

Acoustic response of a quantum Hall ferromagnet at $\nu = \frac{2}{3}$

Von der Fakultät Mathematik und Physik der Universität Stuttgart
zur Erlangung der Würde eines Doktors der Naturwissenschaften
(Dr. rer. nat.) genehmigte Abhandlung

vorgelegt von

Dimitri Dini

aus Pescia (Italien)

Hauptberichter: Prof. Dr. Klaus von Klitzing

Mitberichter: Prof. Dr. Gert Denninger

Tag der mündlichen Prüfung: 29.01.2007

Max-Planck-Institut für Festkörperforschung

Stuttgart 2006

A mathematician may say anything he pleases,
but a physicist must be at least partially sane.

J. Willard Gibbs

Contents

Symbols, Constants, and Abbreviations	7
1 Introduction	11
2 Two-dimensional electron system in a magnetic field	15
2.1 Two-dimensional electron system	15
2.2 Classical magnetotransport	16
2.3 The integer quantum Hall effect	18
2.3.1 Landau level quantization	18
2.3.2 Transport in high magnetic field	19
2.3.3 Edge states	21
2.3.4 Percolation picture	22
2.4 The fractional quantum Hall effect	24
2.4.1 Laughlin's trial wavefunction	25
2.4.2 Composite Fermions (CF) picture	27
3 Quantum Hall ferromagnetism	29
3.1 Exotic spin order at $\nu = 1$	30
3.2 QHF: theoretical pictures	32
3.3 QHF at fractional filling factors	36
3.3.1 The spin in the CF picture	38
3.4 The spin phase transition at $\nu = 2/3$	41
3.4.1 Electron spin polarization at $\nu = \frac{2}{3}$	45
4 Experimental techniques and setup	49
4.1 Surface acoustic waves on piezoelectric materials	49
4.2 Magneto-acoustic interactions mechanism	51
4.2.1 Acousto-electric effect	55
4.3 Setup	57
4.3.1 Sample preparation	57
4.3.2 Apparatus	62

5	Results and discussion	73
5.1	About the devices	73
5.2	Quasi-DC transport	74
5.2.1	Lack of reproducibility and exchange effects	76
5.3	Time dependence	80
5.4	Transport in small Hall bars	84
5.5	SAW measurement: small current regime	86
5.6	SAW measurement: high current regime	90
5.7	Acousto-electric measurements	92
5.8	Domain orientation at the transition	94
5.9	Discussion	97
6	Conclusions	101
A	Sample structure	105
A.1	Wafer 81644	105
A.2	Wafer 8813	105
	Bibliography	107
	Deutsche Zusammenfassung	120
	Acknowledgments	123
	Curriculum Vitae	124

Symbols, Constants, and Abbreviations

Symbols

A	Vector potential.
b	Fit parameter of integer number (only in Sec. 2.4).
B ,	Magnetic field vector.
E	Electric field vector.
E_c	Coulomb energy.
E_F	Fermi energy.
E_z	Zeeman energy.
f	Frequency or generic rational number (only in Sec. 2.4).
H	Hamiltonian.
H_N	Hermite polynomials.
I , I	Current.
J	Current density vector.
k_{eff}^2	Electromechanical coupling coefficient.
k_i	Momentum in the i direction or wavevector.
l_B	Magnetic length.
L	Length.
m	Odd integer number.
m^*	Electron effective mass.
n , n_e	Electron density.
N , N	Landau level index or number of finger pair in an IDT.
p	Generic integer number.
p	Momentum operator.
\mathcal{P}	Electron polarization.
r	Position vector.
R_{ii}	Resistance.
S	Electron spin operator.
S	Electron spin or strain.

t	Time.
T, T	Temperature or stress.
\mathbf{v}	Velocity vector.
V_i	Electrical potential.
V_H, V_H	Hall voltage.
v_{SAW}	Surface acoustic wave velocity.
x, y, z, x, y, z	Position coordinates.
W	Width.
Λ	Attenuation.
ε	Electrical permittivity.
λ	Wavelength.
ΔE	Energy spacing.
Δ_{CF}	Composite fermion cyclotron energy.
$\Delta E_{\text{subband}}$	Subband energy spacing.
τ	Relaxation time.
ω_c	Cyclotron frequency.
ω_c^*	Composite fermion cyclotron frequency.
ω_{cr}	Conductivity relaxation frequency.
μ	Mobility.
μ_i	Chemical potential.
σ	Conductivity.
$\bar{\sigma}$	Conductivity tensor.
Ψ_N	Wavefunction.
ϕ_N	One-dimensional harmonic oscillator wavefunction.
ϵ_N	Energy of the N^{th} Landau level.
ν	Filling factor.
ν_{CF}	Composite fermion filling factor.
ρ	Resistivity or material density.
ρ_{xx}	Longitudinal resistivity.
ρ_{xy}	Transversal (Hall) resistivity.

Constants

$e = -1.6021917 \cdot 10^{-19} \text{ C}$	Electron charge.
---	------------------

$e^2/h = 1/R_K = 0.3874045 \cdot 10^{-6} \Omega^{-1}$	Conductance quantum.
$\Phi_0 = h/e = 2.41797 \text{ Tm}^2$	Magnetic flux quantum.
$g_S = 1, 2$	Spin degeneracy.
$g^* = -0.44$	Effective Landé factor of electrons in bulk GaAs.
$h = 6.626196 \cdot 10^{-34} \text{ Js}$	Planck constant.
$\hbar = h/2\pi$	Reduced Planck constant.
$k_B = 1.380650 \cdot 10^{-23} \text{ JK}^{-1}$	Boltzmann constant.
$m_0 = 9.109558 \cdot 10^{-31} \text{ kg}$	Electron mass.
$m^* = 0.067m_0$	Effective electron mass in bulk GaAs.
$\mu_B = 9.274096 \text{ JT}^{-1}$	Bohr magneton.
$R_K = 25812.807 \Omega$	Von Klitzing constant.

Abbreviations

2DEG	Two-dimensional electron gas.
2DES	Two-dimensional electron system.
a.u.	Arbitrary units.
CF	Composite Fermion.
DC	Direct current.
DOS	Density of State.
ESR	Electron Spin Resonance.
FQHE	Fractional Quantum Hall Effect.
HLR	Huge longitudinal resistance.
HF	High Frequency.
IDT	Interdigital transducer.
IQHE	Integer Quantum Hall Effect.
LL	Landau Level.
LLL	Lowest Landau Level.
MBE	Molecular Beam Epitaxy.
NMR	Nuclear Magnetic Resonance.
QHE	Quantum Hall Effect.
QHF	Quantum Hall Ferromagnetism, Quantum Hall Ferromagnet.
QW	Quantum Well.
RDNMR	Resistively detected nuclear magnetic resonance.

Symbols, Constants, and Abbreviations

SAW	Surface acoustic wave.
SdH	Shubnikov-de Haas.
SO	Spin-orbit.

1 Introduction

The goal of this work is to investigate spin phenomena which occur in two-dimensional electron systems (2DESs) at high magnetic fields and low temperatures.

In the integer quantum Hall effect the electrons occupy an integer number of highly degenerate energy levels separated by the cyclotron energy referred to as Landau levels (Sec. 2.3.1). Due to the electron spin, each of these levels splits into two, separated by the Zeeman energy. When two of these energy levels are degenerate and the number of electrons is not sufficient to fill all of them, two different ground states with different electron polarization can coexist. The system is characterized by ferromagnetic ordering and it is referred to as a quantum Hall ferromagnet. This phenomenon can be explained by exchange energy gain in the ferromagnetic state and Hartree-Fock models are able to describe the physics involved.

The study of a realistic quasi-2DES formed at the interfaces in semiconductor heterostructures leads to effects that are not included in the free-particle picture described above. If electron-electron interaction is considered, new ground states appear with the electrons occupying certain fractions of the available states. This phenomenon is called fractional quantum Hall effect (Sec. 2.4). At the end of the previous millennium, new experimental works observed phenomena reminiscent of quantum Hall ferromagnetism also in the fractional quantum Hall effect regime, being most pronounced at filling factor $\frac{2}{3}$ and $\frac{2}{5}$. In this situation the spin-ordered states become highly correlated and the Hartree-Fock approximation is no longer valid. Transitions between ground states of different spin polarization become possible. Experimental works have provided evidence that these phenomena are closely related to Ising (spin-lattice) ferromagnets. This points to the possibility of formation of domains with ground states characterized by different spin polarization. However, observations without analogy to the usual Ising systems have also been reported.

This picture is even more complicated when the role of nuclei is included. At filling factor $\frac{2}{3}$ many experimental results point out that the electron dynamics is strongly correlated to the one of the host nuclei.

The objective of the present work is to study the ground state and the low-lying excited states at filling factor $\frac{2}{3}$. In order to do this we employ two different measurement techniques. We study the transport properties of a two dimensional electron system with surface acoustic waves and compare them with data obtained from standard lock-in techniques.

Surface acoustic waves are elastic modes propagating on the surface of the crystal. In GaAs they are accompanied by deformation and an oscillating electric field. The latter can interact with the mobile carrier in the two-dimensional electron system and give rise to attenuation and velocity shift of the acoustic wave. Measuring these effects gives access to the electron conductivity. An important aspect is that the conductivity is probed at the frequency and the wavelength of the acoustic mode, a parameter that is chosen during the design of the device and can be optimized up to the GHz range.

The use of surface acoustic waves opens up the possibility to study the spin phase transition at $\frac{2}{3}$ in a different and complementary way with respect to the quasi-DC technique, giving a more complete picture of the phenomenon.

This thesis is organized as follows:

- Chapter 2 will describe the basic properties of a two-dimensional electron system in a magnetic field. The concept of Landau level quantization is introduced together with models that allow the understanding of the integer quantum Hall effect. The fractional quantum Hall effect is also presented. It will be treated using both the Laughlin's trial-wavefunction framework and the composite fermion picture.
- In Chapter 3 we introduce the concept of quantum Hall ferromagnetism. The theoretical pictures put forward to understand this phenomenon will be introduced, together with the experimental evidence of a spin phase transition at fractional filling factors. In the last part of the chapter we will concentrate on the spin phase transition at filling factor $\frac{2}{3}$.
- Chapter 4 will describe in more detail the measurement techniques and the interaction mechanism between a surface acoustic wave and a two-dimensional electron system. Part of our work has been the design and realization of a setup that allows surface acoustic wave measurements. Problems and obstacles

encountered during this work will be discussed, together with the solution adopted to solve them.

- Chapter 5 is the main part of this work. The results of the study of the spin phase transition at $\nu = \frac{2}{3}$ will be presented. Measurements obtained at low and high frequency will be compared. We will also comment on our experimental findings and try to suggest the physics that these imply.
- Finally, we will summarize our results in the Conclusion chapter.

After reading the introduction I would like to wish the reader enjoyment reading this thesis. If you are a newcomer in the field of fractional quantum Hall systems, may this work help you to appreciate how interesting and original the playgrounds in the lowest Landau level are. And if you are an expert in this field, I hope this work still brings something you have not known before.

2 Two-dimensional electron system in a magnetic field

In this chapter we will describe the main properties of a two-dimensional electron system (2DES) in a magnetic field.

In Sec. 2.1 we mention what we mean by 2D and how it is possible to create such a system. In Sec. 2.2 we will describe the classical motion of an electron in a magnetic field. The latter is treated quantum-mechanically in Sec. 2.3. Using the concepts of Landau level quantization and level-broadening by disorder (Sec. 2.3.1) we explain the experimental finding known as integer quantum Hall effect (Sec. 2.3.2). For this purpose we introduce two intuitive pictures involving edge states (Sec. 2.3.3) and the percolation picture (Sec. 2.3.4).

The fractional quantum Hall effect is presented in Sec. 2.4. To understand this many-body phenomenon we introduce the Laughlin's picture in Sec. 2.4.1 and the composite fermion picture in Sec. 2.4.2 respectively

2.1 Two-dimensional electron system

The major impetus in the studies of the quantum Hall effect (QHE) is due to the experimental realization of almost ideal two-dimensional electron systems (2DESs). The electrons are free to move in only two spatial dimensions, while they have quantized energy levels in the third dimension¹. Electron layers have been created in many different ways: on the surface of liquid helium, in a single layer of graphene, in Metal-Oxide-Semiconductor Field Effect Transistors and in semiconductor heterostructures.

In the latter case the 2DES is formed at the interface between two semiconductors with different band gaps. One of the most common systems is the GaAs/Al_xGa_{1-x}As ($0 < x < 1$) heterostructure. The lattice constants for the two materials are almost identical so that the interface is nearly free from disorder. Moreover, using the

¹In reality, the wave functions have a finite spatial extension also in the third dimension.

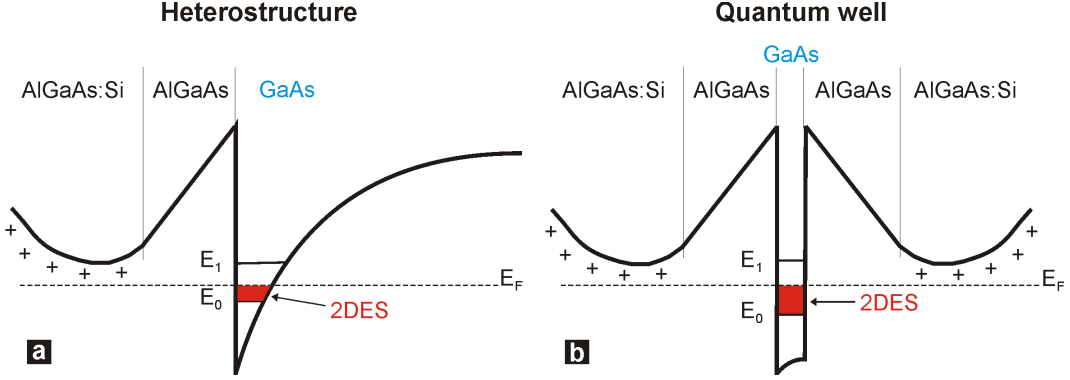


FIGURE 2.1: The conduction band of an AlGaAs/GaAs heterostructure (a) and a quantum well (b) are schematically shown along the grown direction z . A 2DES forms in the GaAs layer with quantized energies in the z -direction. At low temperatures ($k_B T \ll \Delta E_{\text{subband}}$) only the lowest subband is populated. The electrons, supplied from a Si-donor layer, fill the 2DES up to the Fermi energy E_F .

molecular beam epitaxy (MBE) growth technique, it is possible to have precise control over the spatial dimensions of the different layers. Since the $\text{Al}_x\text{Ga}_{1-x}\text{As}$ band gap is wider than that of GaAs, the mobile carriers from the doped AlGaAs alloy move across the interface to the low-lying conduction band of the GaAs. Due to the electric field caused by this charge transfer, the energy bands at the interface are bent and (in first approximation) a triangular potential is formed, as shown in Fig. 2.1a. At low temperature, i.e. $k_B T < \Delta E_{\text{subband}}$ (subband energy spacing), and low density, the electrons occupy only the lowest subband. The doping is usually achieved with a Si-donor layer placed far from the interface in order to minimize scattering.

Electrons can be confined in a potential well, called a quantum well (QW), if two heterojunctions are grown in series ($\text{Al}_x\text{Ga}_{1-x}\text{As}/\text{GaAs}/\text{Al}_x\text{Ga}_{1-x}\text{As}$) as shown in Fig. 2.1b.

2.2 Classical magnetotransport

Fig. 2.2 shows a typical Hall bar geometry: a current I is applied between the source and the drain of a 2DES of width W and length L . In the presence of a perpendicular magnetic field B , the electrons are deflected sideways due to the Lorentz force and produce a voltage V_H perpendicular to the direction of the current (usually called Hall voltage). The transverse or Hall resistance (R_{xy} or R_H) is defined as $R_{xy} = V_{xy}/I$

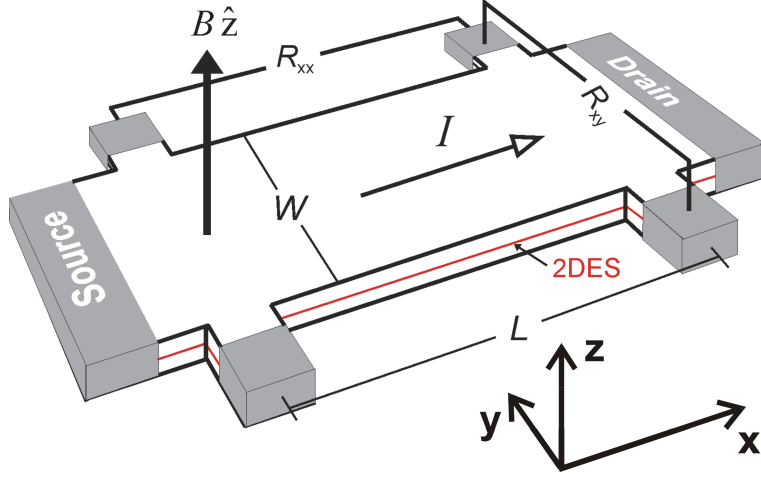


FIGURE 2.2: For magnetotransport measurements, a Hall bar-shaped sample of width W and length L can be used. The current flows from source to drain and the longitudinal voltage V_{xx} , and transverse or Hall voltage V_{xy} , is measured. A magnetic field is usually applied in the z -direction, perpendicular to the 2DES.

while the longitudinal resistance (R_{xx}) is defined as $R_{xx} = V_{xx}/I$.

The classical equation of motion of an electron in a dissipative medium, in the presence of an electric field \mathbf{E} and a magnetic field \mathbf{B} , is:

$$m^* \frac{d\mathbf{v}}{dt} = -e\mathbf{E} - e\mathbf{v} \times \mathbf{B} - m^* \frac{\mathbf{v}}{\tau}, \quad (2.1)$$

where m^* is the electron effective mass and a damping term with constant relaxation time τ has been included to take into account the scattering of the electrons by phonons, impurities and other electrons. Under stationary conditions ($d\mathbf{v}/dt = 0$), in a Hall bar geometry with the electric fields in the xy -plane and the magnetic field in the z -direction with a value B , Eq. 2.1 becomes

$$v_x = -\frac{e\tau}{m^*} \frac{1}{1 + \omega_c^2 \tau^2} (E_x - \omega_c \tau E_y) \quad (2.2)$$

$$v_y = -\frac{e\tau}{m^*} \frac{1}{1 + \omega_c^2 \tau^2} (E_y + \omega_c \tau E_x) \quad (2.3)$$

where $\omega_c = eB/m^*$ is the cyclotron frequency. The mobility μ is defined as $\mu = e\tau/m^*$ and gives information about the transport quality of the sample. The current density $\mathbf{J} = n_e(-e)\mathbf{v}$ (where n_e is the electron density) is related to the electric field by the conductivity tensor $\bar{\sigma}(B)$ via $\mathbf{J} = \bar{\sigma}(B)\mathbf{E}$. From that we can deduce the

resistivity tensor $\bar{\rho}(B) = \bar{\sigma}^{-1}(B)$, so we end up with the following equation for the transversal and longitudinal resistivity:

$$\rho_{xx}(B) = \frac{1}{en_e\mu} \quad \text{and} \quad \rho_{xy}(B) = \frac{B}{en_e}.$$

2.3 The integer quantum Hall effect

2.3.1 Landau level quantization

At high magnetic field the electrons can complete a full cyclotron path and interfere with themselves. In such a situation the classical model described above is no longer valid and a quantum treatment of the problem is required [1].

One convenient choice of the vector potential \mathbf{A} describing the magnetic field is the so-called Landau gauge: $\mathbf{A}(\mathbf{r}) = (-yB, 0, 0)$. The Hamiltonian of a free electron in a magnetic field can be written as

$$H = (p_y^2 + (p_x - eBy)^2) \frac{1}{2m^*} \quad (2.4)$$

Taking advantage of the translation symmetry in the x direction, we can write the wavefunctions in the form $\Psi_N(x, y) = e^{ik_x x} \phi_N(y)$ where the eigenfunctions $\phi_N(y)$ results in the solution of a one-dimensional displaced harmonic oscillator whose frequency is the cyclotron frequency $\omega_c = \frac{eB}{m^*}$ and whose central position is $y_0 = -k_x \ell_B^2$, with $\ell_B = \sqrt{\frac{\hbar}{eB}}$ the magnetic length.

Hence, the total eigenfunctions Ψ_N are:

$$\Psi_N \propto e^{ik_x x} \exp\left[-\frac{(y - y_0)^2}{2\ell_B^2}\right] H_N\left[\frac{(y - y_0)}{\ell_B}\right], \quad (2.5)$$

where H_N are the Hermite polynomials.

The energy eigenvalues are a discrete set of ladder-levels referred to as Landau levels (LLs):

$$\epsilon_N = \hbar\omega_c \left(N + \frac{1}{2}\right), \quad (2.6)$$

where $N = 0, 1, 2, \dots$ is the Landau level index. We can include the spin degree of freedom by adding the Zeeman energy term E_Z to equation 2.6:

$$\epsilon_N = \hbar\omega_c \left(N + \frac{1}{2}\right) + g^* \mu_B B s. \quad (2.7)$$

where g^* is the reduced g-factor, μ_B is the Bohr magneton, and s the spin quantum number $= \pm 1/2$. The energy eigenvalues are obtained regardless of the gauge chosen for the vector potential \mathbf{A} . Also, the center coordinate of the wavefunctions y_0 is independent of (x,y) , which means that each electron will have the same energy, and the degeneracy of a single LL will depend on the number of states that can be packed into that level. If the system is confined in a rectangular cell of sides L_x and L_y , the degeneracy of each LL (N_L) is the number of allowed values of k_x , such that the center y_0 lies between 0 and L_y . Using periodic boundary conditions in the x direction, we obtain $N_L = L_x L_y eB/h$. The filling factor ν can be defined as the ratio between the total number of electrons, N_e , and the degree of degeneracy in each LL, N_L :

$$\nu = \frac{N_e}{N_L} = \frac{n_e h}{eB}. \quad (2.8)$$

So far, we have only considered the DOS of the LLs to be δ -like functions. However, in reality the LLs will be broadened by disorder [1]. The tails of the LLs now consist of localized states (i.e. states in which electrons are confined to a small region in space and do not carry current across the sample) and current-carrying or extended states at the center of the levels. It should be noticed that even if the Fermi energy is located in a gap between Landau levels, extended states always exist at the lateral boundaries of the 2DEG since the Landau level energy raises at the edge. This results in extended states at the Fermi energy running parallel to the edge (see Sec. 2.3.3).

2.3.2 Transport in high magnetic field

Fig. 2.3 shows one measurement of electronic transport properties performed on a 2DES at a temperature of 280 mK. In this graph, the longitudinal resistivity ρ_{xx} (solid curve) and the Hall resistivity ρ_{xy} (dashed curve) are plotted versus the magnetic field B . At low fields ($B < 0.2$ T), ρ_{xy} increases linearly with B while ρ_{xx} remains constant, as expected from the classical magnetotransport theory described in Sec. 2.2. However, at higher fields, a series of plateaus in the Hall resistivity, accompanied by a vanishing longitudinal resistivity, becomes the most striking feature in the curve. The value of these steps is given by:

$$\rho_{xy} = \left(\frac{1}{\nu}\right) \frac{h}{e^2} \quad (2.9)$$

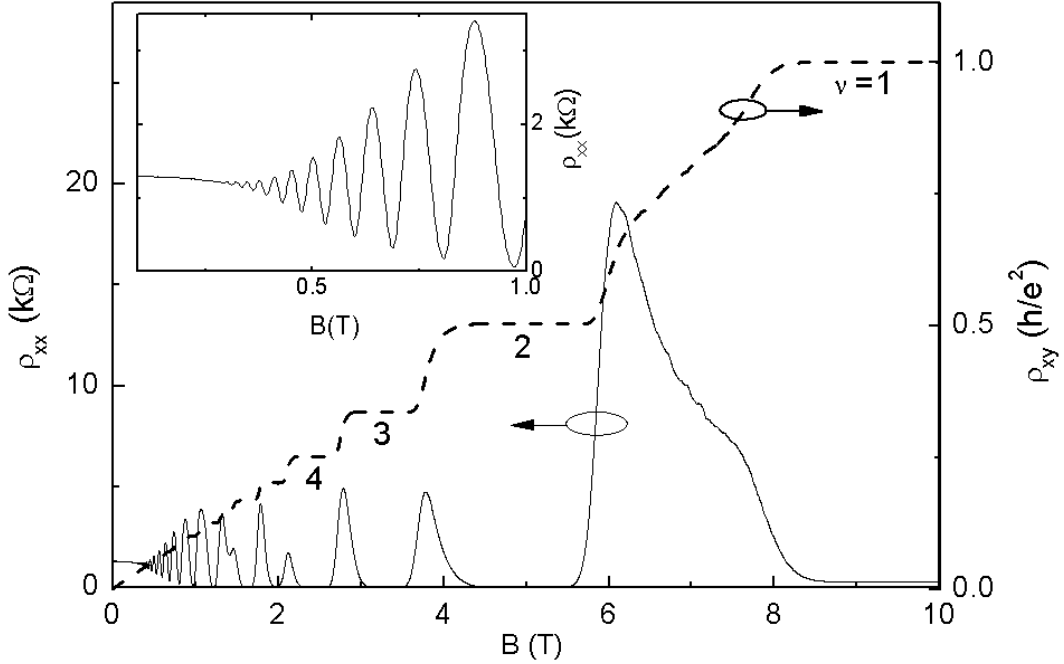


FIGURE 2.3: IQHE: at high magnetic fields the Hall resistivity ρ_{xy} (dashed curve) is characterized by plateaus quantized to $(1/\nu)h/e^2$ for integer filling values ν , accompanied by a vanishing longitudinal resistivity ρ_{xx} (solid curve). Inset: SdH oscillations in ρ_{xx} at low fields (Sample from wafer 71994).

for an integer filling factor ν . This phenomenon, discovered by Klaus von Klitzing, is known as the integer quantum Hall effect (IQHE) [2, 3]. The resistance value at filling factor 1 is known as the von Klitzing constant ($R_K = 25812.807\dots \Omega$) and is used to maintain the standard of electrical resistance by metrology laboratories around the world. In fact, it can be measured with a precision up to 10^{-8} [4, 5], depends only on the fundamental constants e and h and is not affected by any sample parameters. The oscillations in ρ_{xx} at low fields where there are no plateaus, known as Shubnikov-de Haas (SdH) oscillations, are periodic in $1/B$ and inversely proportional to the density: $\Delta(1/B) = g_s e / h n_e$ (g_s is the spin degeneracy). Even though the IQHE was discovered almost 25 years ago, there are still many questions which remain unanswered concerning its nature. Several successful approaches and formalisms, however, have been put forward which accurately describe many of the observed phenomena (for a review see [1, 6, 7, 8]). In general, all of these approaches include Landau level formation, low temperatures ($k_B T \ll \hbar \omega_c$) and the existence of localized states. In this work we will concentrate on two differ-

ent approaches: the *edge state* and the *percolation* pictures.

2.3.3 Edge states

In Sec. 2.3.1 we calculated the energy spectrum of free electrons. Now we consider the problem of electrons confined in an Hall bar of finite width by a soft wall potential $V(y)$, where the potential changes slowly with respect to the magnetic length. Far from the boundary (where $V(y) = 0$) the energy eigenvalues are the same as in Eq. 2.7 [1]. Near the boundary the energy of a state is just the sum of the Landau energy and the electrostatic energy. Due to the confining potential, the group velocity

$$\mathbf{v}_k = \frac{1}{\hbar} \frac{\partial \epsilon_{nk}}{\partial \mathbf{k}} \hat{y} \quad (2.10)$$

has an opposite sign on the two edges of the sample. For N filled LLs, one gets N quasi-one-dimensional edge channels at the Fermi energy on either side of the sample through which dissipationless current flows². Using the Landauer formulation of transport, a Hall voltage drop across the sample in the y direction corresponds to a difference in the (electro)chemical potential between the two edges. Assuming zero temperature and integrating over the group velocities of all occupied states one obtains $I_N = Ne/h \times [\mu_R - \mu_L]$, where μ_R (μ_L) is the chemical potential of the right (left) edge. Hence we obtain

$$I_N = N \frac{e^2}{h} V_H \quad (2.11)$$

with N integer. Since in the QHE case the right and left movers are physically separated in such a way that the voltage drop is transverse to the current, we have the desired results

$$\sigma_{xx} = 0 \quad \sigma_{yx} = N \frac{e^2}{h}. \quad (2.12)$$

In the presence of localised states, the current will be reduced due to backscattering. However, in the QHE case, that process would require transfer of the electron from

²The semi-classical interpretation of these currents is that they represent skipping orbits in which the circular cyclotron motion is interrupted by collisions with the walls at the edge of the sample.

one edge of the sample to the other, since they are spatially separated. For ideal samples without disorder the probability for such a process to happen is exponentially small. In short, only forward scattering can happen. If the disorder causes LL mixing to occur, then the electron in one channel can scatter into another, but still going in the same direction, so there is no backscattering. This unidirectional nature of the edge state gives rise to the universal Hall quantization. The localized states formed by the disorder will allow the chemical potential to vary smoothly with density (or magnetic field), but will not contribute to the transport, so the Hall conductance will be quantized over a plateau of finite width.

In the presence of a magnetic field most states are localized. However, if all states were localized, no transition from one QHE plateau to the next would be possible. In order to understand this we will now introduce the intuitive percolation picture.

2.3.4 Percolation picture

Let us consider a smooth random potential caused, for example, by ionized silicon donors remotely located away from the 2DES. We also consider the magnetic length to be small on the scale over which the potential varies (see e.g. [9]).

Due to the motion of electrons perpendicular to the potential gradient, charges at the Fermi energy E_F move along the equipotential lines $E_F = \text{constant}$.

As we decrease the magnetic field at constant density and occupy a single LL with electrons, the Fermi energy moves across the broadened level. At the low-energy tail, electrons first start occupying the deep valleys; they are localized and do not contribute to transport (Fig. 2.4a). At this point ρ_{xx} vanishes and ρ_{xy} is quantized. As the magnetic field is further changed, the occupied valleys grow larger until their shorelines, where the electrons can move, percolate from one side of the sample to the other (Fig. 2.4b). Electrons can now move across the sample and scatter back to the source. As the Fermi level approaches the percolation threshold (the center of the LL) the trajectories of the edge states on the two sides will go deeper and deeper into the bulk and the edge states start to communicate with each other. Electrons in one edge state can be backscattered into the other edge state and be reflected. This backscattering process impedes transmission of the electrons from source to drain and thereby causes ρ_{xx} to take on finite values and ρ_{xy} to deviate from the quantized value. At this point the Fermi energy lies in the extended states of the LL. By further increasing the field, the electrons occupy most of the sample except

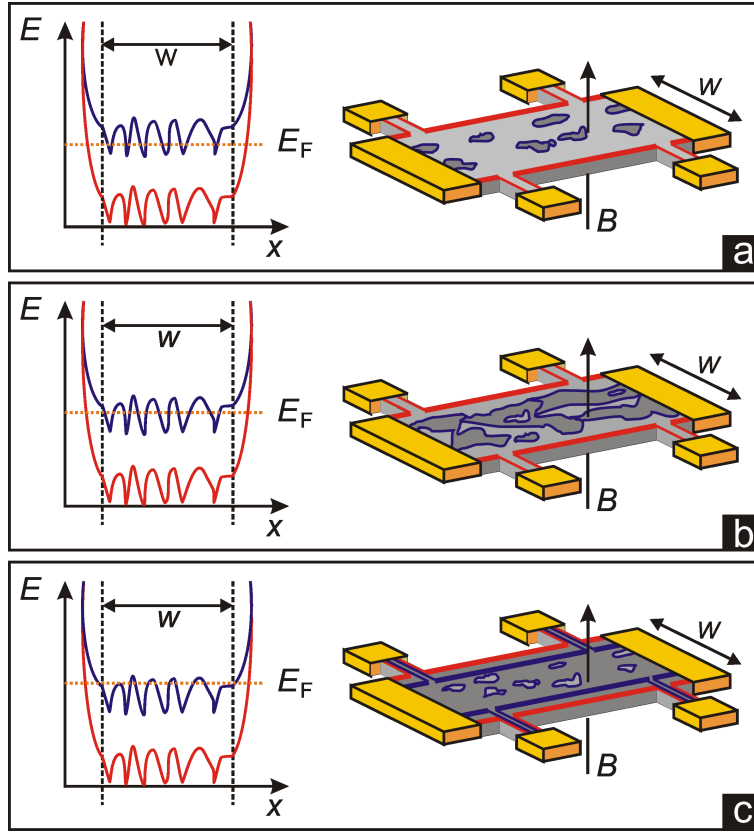


FIGURE 2.4: Left: Confinement potential for a sample of width W . LLs are affected in the bulk by the disorder and curve up sharply near the edges due to sample boundaries. Right: Contour maps of the potential landscape. Dark gray areas indicate filled states and light gray areas empty states. (a) The Fermi energy, E_F , is at the low-energy tail of the second LL (localized states). Electrons occupy only deep valleys without backscattering (ρ_{xy} is quantized, $\rho_{xx} = 0$). Intersection of E_F with the first LL near the edges leads to edge channels as indicated on the Hall bar with red line. (b) E_F is at the center of the second LL (extended states). Electrons backscatter from one edge to the other (ρ_{xy} is not quantized, $\rho_{xx} \neq 0$). (c) E_F is at the high-energy tail of the second LL (localized states). Current flows on energy contours of mountain tops and edge states (red and blue line) without backscattering (ρ_{xy} is quantized, $\rho_{xx} = 0$).

for the top of the potential hills. In this case, backscattering is again suppressed and ρ_{xx} vanishes while ρ_{xy} is quantized (see Fig. 2.4c).

2.4 The fractional quantum Hall effect

Quantized Hall plateaus characterized by simple rational fractional quantum numbers appear at very low temperature and in the case of weak disorder.

Figure 2.5 shows the longitudinal resistivity and the Hall resistance versus the magnetic field for a high-mobility sample. The curves are characterized by plateaus in ρ_{xy} quantized to values of h/fe^2 , where f is an exact rational value with an odd denominator, accompanied by a vanishing ρ_{xx} . In the LLL, these fractions occur at certain sequences, which can be summarized by the following equations:

$$f = \frac{b}{2pb \pm 1} \quad (2.13)$$

and

$$f = 1 - \frac{b}{2pb \pm 1}. \quad (2.14)$$

Here, p and b are both integer numbers. All of these fractional states are characterized by having odd denominators, being symmetric around $\nu = 1/2$ and having

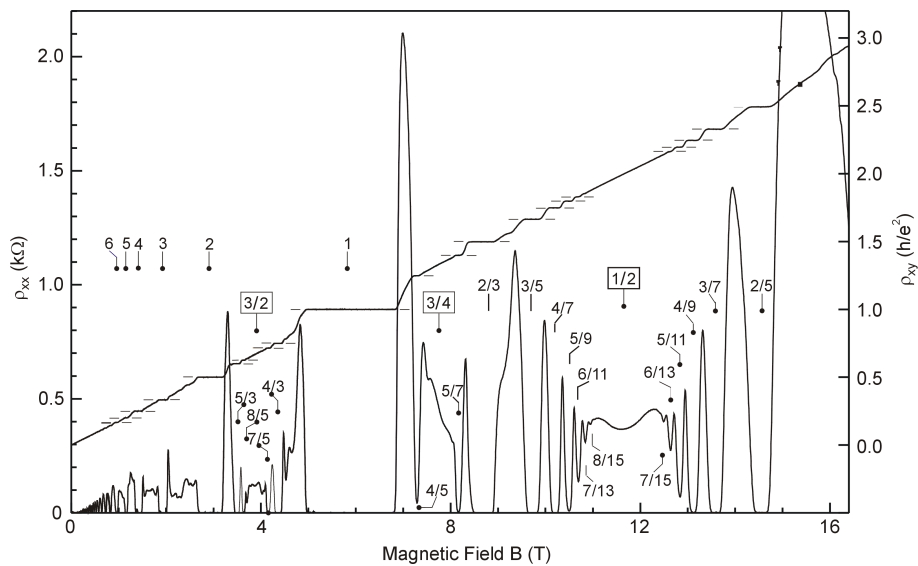


FIGURE 2.5: FQHE: in the lowest Landau level (LLL), a number of plateaus at fractional values of h/fe^2 appear in the Hall resistance, accompanied by a vanishing longitudinal resistivity. These fractional quantum Hall states are caused by Coulomb interactions between the electrons in a strongly correlated system. These measurements were performed by J.H. Smet and the sample grown by W. Wegscheider.

a larger energy gap for small denominators. The existence of fractional QH states was completely unexpected, since in the single particle picture no gap should exist below $\nu = 1$. In order to understand the FQHE, electron-electron interaction has to be taken into account. As a result, the Hamiltonian of equation 2.4 now reads

$$H = \frac{1}{2m^*} (-i\hbar\nabla + e\mathbf{A}(\mathbf{r}_j))^2 + \frac{e^2}{4\pi\epsilon_0} \sum_{j < k} \frac{1}{|\mathbf{r}_j - \mathbf{r}_k|} + \sum_j U(\mathbf{r}_j) + g\mu_B \mathbf{B} \cdot \mathbf{S}. \quad (2.15)$$

In the Hamiltonian, we have added the Coulomb interaction energy (second term on the right side), the positive background and disorder potential (third term) and the Zeeman energy (last term) [8, 10].

Several approaches were taken in order to understand the problem of interactions in the lowest Landau level (LLL) [11, 12, 13]. Laughlin's proposal of a trial wavefunction proved to be very successful in describing the strong electron correlations that characterize the $\nu = 1/m$ QH ground states with m being an odd integer [14, 15]. This is treated in the next section.

2.4.1 Laughlin's trial wavefunction

When the FQHE was discovered, Robert Laughlin realized that one could write down a many-body variational wavefunction at filling factor $1/m$ in the form

$$\Psi_{1/m} = \prod_{i < j} (z_i - z_j)^m \exp \left[-\frac{1}{4\ell_B^2} \sum_i |z_i|^2 \right]. \quad (2.16)$$

In this formula, $z_{i,j}$ is the position of an electron denoted as a complex number and $m = 2p+1$ where p is an integer. There are certain restrictions for the wavefunctions. For example, for $\Psi_{1/m}$ to be analytic m must be an integer and to preserve the antisymmetry it has to be restricted to odd integers. It is assumed that since the electrons are only occupying the lowest spin split LL, the spin degree of freedom is frozen, i.e. the system is fully polarized³.

The second part of Eq. 2.16 is merely the Gaussian wavefunction of the problem without interactions. More interesting is the first part of the equation, the so-called Jastrow-type term. This term naturally builds in good correlations among the electrons because each particle sees an m -fold zero at the position of all the

³In reality this assumption holds only for $\nu = 1/m$ ground states. At other fractional filling factors, partial or zero polarization ground states do exist.

other particles. The wavefunction vanishes extremely rapidly if any two particles approach each other, and this helps minimize the expectation value of the Coulomb energy.

Laughlin's trial wavefunction method was well corroborated by Monte-Carlo and other numerical calculations and set the base for understanding the FQHE.

Laughlin's fractionally charged quasiparticles

So far, we have presented the necessary wavefunction that explains the FQH ground states at $\nu = 1/m$. Since at these filling factors $\rho_{xx} \rightarrow 0$, gapped elementary excitations should exist. Here the question arises what these gapped excitations are. Laughlin showed that they are fractionally charged quasiparticles [14, 15]. This can be understood by considering $\nu = 1/3$ as an example. If we move away from exactly $\nu = 1/3$ by either slightly increasing ($\nu < 1/3$) or decreasing ($\nu > 1/3$) the magnetic field (or changing the density), we can introduce or remove a single quantum of magnetic flux, respectively. Since 3 flux quanta exist per electron of charge e , it is then equivalent to say that the introduction or removal of a flux quantum means adding either a quasihole or a quasielectron of fractional charge $e^* = e/3$. The excitation gap is then given by the necessary energy required to include the quasiparticle. In general quasiparticle excitations have a charge $e^* = e/m$ and obey neither Bose-Einstein nor Fermi-Dirac statistics, but rather anyonic statistics. Shot-noise and tunnel experiments, which have satisfactorily proven the existence of fractionally charged excitations, were essential in supporting Laughlin's theory [16, 17]. Recent works on Aharonov-Bohm interferometers have also proven the anyonic nature of these quasiparticles [18, 19]. One major drawback of Laughlin's approach is that it only accounts for the $1/m$ FQH ground states. The wavefunctions for the other fractions (see Fig. 2.5 and equations 2.13 and 2.14), such as $\nu = 2/3$, are not considered if Laughlin's ansatz is used. Many of the missing fractions could be accounted for by the hierarchy approach, in which higher order FQHE states are constructed with Laughlin's quasiparticles instead of electrons [20, 21, 22]. Nonetheless, this approach turned out to be incomplete. For example, it failed to describe the experimental data, in which some states are more stable than others. A very elegant and natural way of describing all of the FQHE states in the LLL is Jain's composite fermion picture described in the next section.

2.4.2 Composite Fermions (CF) picture

The resemblance between the IQHE and the FQHE seen experimentally hinted to the idea that many of the phenomena occurring in the FQHE could be explained by transforming the strongly interacting system of electrons into a weakly interacting system of some new quasi-particles. Jain's success in identifying *composite fermion* as these quasi-particles was a major achievement in this field [23]. In the following, we describe the basic concepts of this model: if an even number ($2p$) of vortices of the many-body wavefunction are captured by an electron, a new quasiparticle, referred to as a composite fermion (CF) is formed [10, 23, 24]⁴. In a simplified picture, we can say that $2p$ point flux quanta are attached to an electron. At $\nu = 1/2$, $p = 1$ and for this special case each electron carries exactly 2 flux quanta. The composite particles experience an effective magnetic field, which is given by

$$B_{\text{eff}} = B_{\text{ext}} - 2n_e\phi_0. \quad (2.17)$$

Here, B_{ext} is the external magnetic field and n_e the electron density. Generally speaking, it is possible to interpret the effective magnetic field as follows: an electron is attached to 2 “fictitious” flux quanta which are oriented opposite to the external magnetic field. These partially cancel the real magnetic field resulting in B_{eff} .

At $\nu = 1/2$, $B_{\text{eff}} = 0$ and a CF Fermi sea forms. B_{eff} deviates from 0 as one moves away from $\nu = 1/2$ and it is negative for $\nu > 1/2$ and positive for $\nu < 1/2$. Consequently, composite fermions occupy CF LL which are energetically separated by $\hbar\omega_c^*$, with the CF cyclotron frequency $\omega_c^* = \frac{eB_{\text{eff}}}{m_{\text{CF}}^*}$, where m_{CF}^* is the CF effective mass. The CF filling factor can be obtained from the electron filling factor by using the following relation:

$$\nu = \frac{\nu_{\text{CF}}}{2\nu_{\text{CF}} \pm 1}. \quad (2.18)$$

This is obtained by replacing B by B_{eff} of equation 2.8. For example, $\nu = 2/3$ and $\nu = 2/5$ become $\nu_{\text{CF}} = 2$ for negative or positive B_{eff} , respectively. The CF model explains the experimental results astonishingly well. All of the fractional states can be well understood with this model. Even the recently discovered FQHE fractions (for example $\nu = 4/11$ and $\nu = 5/13$) could be explained as FQH states of CFs [25, 26]. Comparing again with Fig. 2.5, we see that ρ_{xx} shows SdH oscillations

⁴If an odd number of vortices is captured by an electron, the resulting quasi-particle is a composite boson.

which are symmetrical around $\nu = 1/2$. This resembles the case for electrons around $B = 0$.

In general, the FQHE of strongly-correlated electrons can be considered to be the IQHE of weakly interacting composite fermions.

3 Quantum Hall ferromagnetism

In this chapter we describe the physics of a 2DES when different Landau levels become degenerate in energy.

The system presents features similar to what observed in magnetism, like hysteresis, peculiar time dependence, Barkhausen jumps and so on. Due to the above analogy this field has been named quantum Hall ferromagnetism (QHF) and the ground states can be characterized by ferromagnetic ordering.

In Sec. 3.1 we describe the simplest and most understood quantum Hall ferromagnet: a 2DES at filling factor 1. Peculiar type of charged spin-textures excitations named skyrmions can occur in this system due to the interplay between Zeeman and Coulomb energy. Different kind of ferromagnetic ordering can occur in QHFs, and many theories have been used to describe them. Some of these are reviewed in Sec. 3.2, where we focus on the similarities and the main differences between them. The concept of domain formation at the (phase) transition between different ground states will be introduced. In the same chapter we will also describe the low-energy excitations that are predicted for a QHF and that are responsible for the peculiar experimental features of these systems.

QHFs have been studied extensively in many experiments. We will review the main experimental findings in Sec. 3.3, where we will concentrate on experiments performed at fractional filling factors. We will describe the main fingerprints of the QHF like hysteresis and reentrant behavior of the longitudinal resistance upon tilting the magnetic field. The last section, Sec. 3.4, deals with the special quantum Hall ferromagnet that occurs at $\nu = \frac{2}{3}$, the subject of the rest of this thesis. This system has been extensively studied experimentally. Moreover, at this particular filling factor, the 2DES is strongly coupled with the spin of the host nuclei through hyperfine interaction. This interaction can produce dynamical nuclear polarization and a huge increase of the longitudinal resistance, a phenomenon named HLR.

3.1 Exotic spin order at $\nu = 1$

At $\nu = 1$ the lowest spin state of the lowest LL is completely filled. Naively one would expect that the spin dynamics of electrons are frozen out by the Zeeman energy¹. However, in GaAs, the Zeeman energy is much smaller than the cyclotron energy due to the small effective mass and the reduced g factor. This means that it is possible to be in a regime in which the orbital motion is fully quantized ($k_B T < \hbar\omega_c$), but the low-energy spin fluctuations are not completely frozen out ($k_B T \sim g^* \mu_B B$). The peculiar kind of ferromagnetism in this system is called itinerant, or Heisenberg type, and it depends on the interplay between the Zeeman energy and the Coulomb energy between electrons. Magnetism occurs not because of direct magnetic forces, but rather because of the combination of electrostatic forces and the Pauli principle. In a fully ferromagnetic state all the spins are parallel and hence the spin part of the wavefunction is symmetric. This means that the spatial part has to be antisymmetric and it vanishes when any two particles approach each other. This makes the Coulomb energy much higher than the Zeeman splitting, stabilizing the ferromagnetic state and giving rise to a fully polarized ground state [9].

Let us consider the low energy excitations of this ferromagnetic state.

The lowest-lying excitations are spin waves, in which the spin orientation undergoes smooth fluctuations in space and time. Since they don't carry charge they do not strongly alter the transport properties.

Since at $\nu = 1$ the lowest spin state is fully occupied, a second kind of excitations is obtained by reversing a single spin. However, in 1993, Sondhi *et al.* [27] discovered that it is energetically favorable to form a topological spin texture by partially tuning some of the spins. Such a topological object, referred to as skyrmion², is schematically drawn in Fig. 3.1. Skyrmions are characterized by having their spin turned downward at the center and gradually turning upward over a certain distance from the center. At intermediate distances, all the spins point in the xy -plane and exhibit a vortex-like winding configuration. Whenever the Coulomb exchange energy is large in comparison to the Zeeman energy a skyrmion is energetically more favorable than a single spin flip. The size of a skyrmion and the number of spin reversals are then determined by the interplay between these two energies. At $E_Z = 0$

¹In free space with $g=2$ (neglecting QED corrections) the Zeeman splitting is equal to the cyclotron splitting.

²The name is due to its provenance from the Skyrme model in nuclear physics [28].

the size of the skyrmion should be infinite. Increasing the Zeeman energy shrinks the skyrmion in order to balance the Coulomb energy. At large E_Z the single particle model is restored and the excitations are single spin flips. Skyrmions carry a charge that is equal to $\pm e$ and freeze out at exactly filling factor 1 at sufficiently low temperatures. However, as one moves away from it, the energetically lowest way to add or remove charge is through the formation of a finite density of skyrmions (for $\nu > 1$) or antiskyrmions ($\nu < 1$) [29]. Experimentally, the presence of skyrmions was first observed with Nuclear Magnetic Resonance (NMR) by measuring the Knight shift in the Larmor frequency of the host nuclei [30], and then by detecting the heat capacity [31, 32].

New low-energy collective excitations exist in the presence of many skyrmions: the so-called Goldstone modes. Unlike ordinary spin waves, these Goldstone modes can have a minimum excitation gap lower than the Zeeman energy. In fact, the system can support excitations down to zero energy. These excitations are related to the broken spin rotational symmetry of the ground state and they can be understood using a semi-classical picture: in ordinary ferromagnets all the spins in the ground state are aligned along a particular axis. The ground state is invariant under rotation around this axis, so no additional energy is required for such a symmetry

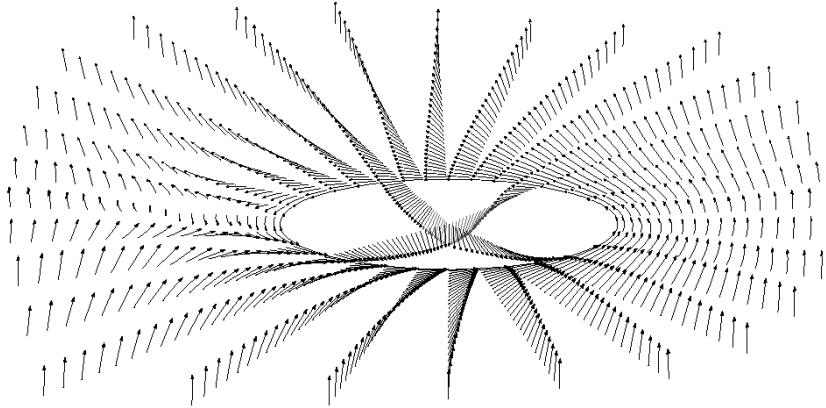


FIGURE 3.1: The lowest-lying energy excitations of the QHF state $\nu = 1$ at vanishing Zeeman energy are topological objects with an underlying spin-texture known as skyrmions. These structures are characterized by gradually flipping numerous electron spins but yet they carry exactly one unit of charge. The spin points downwards at the center and upwards at a distance far from the center. At some intermediate distance the spin points in the xy -plane. The existence and the size of a skyrmion are determined by the interplay between E_Z and E_C .

operation. In the presence of skyrmions the spins are no more aligned and the system is not collinear. States produced by different rotations of the ground state are now distinguishable from each other and additional excitations are produced.

3.2 QHF: theoretical pictures

In the previous section we introduced the Heisenberg ferromagnet at $\nu = 1$ and we briefly mentioned the different kinds of low-lying excitations in such a system. It turns out that many-body interactions can give rise to ferromagnetic ordering at many other filling factors, leading to the notion of quantum Hall ferromagnets (QHFs) [33]. In general, according to Hartree-Fock theory, broken-symmetry ground states occur at integer filling factors in quantum Hall systems whenever two or more partially filled LLs are degenerate. In this situation, the system can support different ground states, with the formation of domains of different ferromagnetic order. Single-particle states in the IQHE are defined by the subband (or layer index), by the LL index and by the electron spin orientation. In the theory of QHFs the levels under study are labeled with a pseudospin variable of value 'up' or 'down', indicated respectively with \uparrow and \downarrow . In this language the splitting between pseudospin-up and -down plays the role of the Zeeman energy and determines the ground state properties. The introduction of a pseudospin variable brings a direct analogy with the field of magnetism. It also allows the study of different energy crossing within the same theoretical framework. When two pseudospin energy levels cross each other, the pseudospin degeneracy can be spontaneously broken, giving rise to pseudospin anisotropy. Depending on the nature of the crossing, different kinds of ferromagnetic anisotropy are possible, each of them exhibiting different properties [33]. Systems with *easy-axis* anisotropy present a discrete direction at which the energy of the ordered state is minimized. They have long-range order at finite temperature and Ising-type phase transitions. For systems with *easy-plane* anisotropy a continuum of coplanar pseudospin magnetization orientations exists at which the energy of the ordered state is minimized. They do not have long-range order but do have a Kosterlitz-Thouless phase transition at finite temperature. Finally, in the *isotropic* case, all directions of pseudospin magnetization have identical energy, only the ground state has long-range order and there are no finite-temperature phase transitions.

A lot of different theoretical works discuss the physics of QHFs. We will present some of the most important ones in this section.

Already in 1985 Giuliani and Quinn [34] proposed that in a QH system at filling factor 2, a phase transition from a paramagnetic to a ferromagnetic phase should occur at LL crossing.

Later on, an important step in the understanding of QH ferromagnetism came from the two papers of Fal'ko and Iordanskii [35, 36]. They calculated the low-lying excitations in a 2DES characterized by a single-particle Zeeman energy on average equal to zero over the 2D plane, but locally fluctuating between positive and negative values. They argue that such fluctuations, given by interface roughness in the device or by inhomogeneity of the nuclear spin polarization, would lead to the formation of a multidomain structure in the ferromagnetic 2DES. In contrast to [34], the theory of Fal'ko and Iordanskii includes also spin-orbit coupling. In [35] they calculate the excitation spectrum for $\nu = 1$. The lowest eigenvalue corresponds to a spin wave (the Goldstone mode) in which the component of the polarization vector in the plane of the 2DES varies smoothly along the domain walls. Other excited states are spin waves in the bulk of the domains, rather than along the walls; their spectrum has a gap of the order of the Zeeman energy and a linear dispersion in the wavevector. The soft excitations described until now do not carry charge so they do not affect the transport properties. More important is a second kind of excitations that develops at the domain wall. These are charged topological spin textures very similar to skyrmions (see Sec. 3.1), but with the difference of being localized at the domain wall and having an activation energy lower than the one of standard 2D skyrmions. The latter condition prevents these new topological excitations to decay into skyrmion-bulk excitations. In the paper they suggest that this quasi-skyrmion excitation can have a dominating role in the dissipative conductivity σ_{xx} when the network of DWs forms a percolation cluster through the entire 2D plane. In [36] they extended their analysis to a narrow QW in the $\nu = (2n + 1)$ QH ferromagnetic state. They deduce that, upon decreasing the single particle Zeeman splitting E_z , the pseudospin polarization of the system exhibits an easy-axis configuration with the formation of the quasi-skyrmion excitations described above. Upon further decreasing E_z , the easy-axis configuration is followed by a phase transition to helical

spin texture³.

Jungwirth and MacDonald [33, 38] and in collaboration with others [39, 40], published many contributions to the field of QH ferromagnetism. In [33] they present a Hartree-Fock analysis of the different kinds of ferromagnetism, including a classification of the different pseudospin anisotropies depending on the nature of the crossing LLs. In [38] they investigate the Ising-type ferromagnet at $\nu = 3$ in order to explain the origin of the anomalous dissipation observed in experiments [41]. In the framework of Hartree-Fock theory, they propose that close to the degeneracy the system breaks up into domains of different pseudospin polarization. The domain wall loops carry a charge quantized in units of the electron charge e and the relative number of these loops changes as a function of the magnetic field. Exactly at the degeneracy point, most of the domains are large and carry a charge of $2e$. The Hartree-Fock quasi-particle energy reduces drastically near the domain wall. They suggest that the increase in dissipation is due to the fact that the quasi-particle can percolate across the sample by scattering between overlapping loops. In their picture the domain wall loops shrink and do not overlap any more when the temperature is too low or the electron density is too high, in accordance with the experimental findings. Their model also reproduces the experimental asymmetry in the longitudinal resistance when the magnetic field is swept upwards or downwards. Moreover, the experimental temperature at which the pseudospin order is lost ($\sim 500\text{mK}$) is correctly reproduced by their theory.

Chalker *et al.* [42] present a similar argument for the dissipation in Ising type QHF, but in order to explain the experimental observation of magnetoresistance anisotropy in Ref. [43, 44], they suggest that, when a magnetic field component parallel to the plane of the 2DES is added, the domains assume a stripe shape depending on the orientation of the gradient of the surface roughness with respect to the direction of the in-plane magnetic field.

Brey and Tejedor present a different picture [45]. They start by assuming the existence of domains, and they calculate the energy spectrum of a domain wall at $\nu = 2$. They consider a functional that include both the spin-orbit interaction and the

³Recently helical spin-order in magnetic materials has been observed in real space [37].

Coulombic interaction between the charged domain walls and that describes the low-energy pseudospin textures of the system. The solutions obtained are topological excitations related to neutral and charged domain walls. For the latter, they compute the size and the energy of the excitations as a function of the spin-orbit term. In their picture, the current *along* the domain walls is different from zero only if the chemical potential does not lie in the charge excitation gap. On the other hand, if the chemical potential does lie in the gap, the carrier has to pass *across* the domain wall. In other words, one electron with a given real spin can pass across the wall smoothly flipping its spin. Since the spin-orbit coupling (related to the excitation gap of the domain wall) is small, only a few electrons can pass through the wall, and the resistance is therefore high. They also claim that the hyperfine interaction with the nuclear spin has no role in the transport properties. At most, due to the slow relaxation time of the nuclear spins, those can serve as spin memory for the electrons.

The last theoretical work that we want to mention is from Freire and Egues [46]. They employ the spin density functional theory (SDFT) in a local spin density approximation to calculate adiabatically (in the change of the magnetic field) longitudinal resistance, total energy, spin-dependent electron density and spin polarization. *Without including domains*, they find that all of these quantities show hysteretic behavior depending on the magnetic field sweep direction, in accordance with the experiment of Ref. [47]. They attribute this effect to the coexistence of two solutions of the ground state SDFT functional due to the spin-dependent exchange potentials of the 2DES for up and down magnetic field sweep. They also infer that a dip in the Hall resistance should be present at the magnetic field at which the hysteresis is present.

In conclusion, many different theories have been used to describe the physics of a QHF. All of them managed to reproduce some of the experimental features and it is difficult to decide upon which theory is the correct one.

Two in particular are the questions that remain to be answered: do the domains exist? Which is the mechanism responsible for the anomalous dissipation at the phase transition observed in experiments?

3.3 QHF at fractional filling factors

In the previous paragraph we reviewed some of the main theoretical approaches to the problem of QH ferromagnetism. We focus now on experiments.

QH ferromagnetic order at integer filling factors has been studied in a variety of different systems, including $\text{Ga}_x\text{In}_{1-x}\text{As}/\text{InP}$ [48], $\text{GaAs}/\text{Al}_x\text{Ga}_{1-x}\text{As}$ [44], InSb [49], Si/SiGe [43], magnetically doped QWs [47], parabolic QWs [50], AlAs QWs [41, 51, 52, 53]. Moreover, using wide QWs or bilayer systems, the extra degree of freedom due to the (different) layer indices opens the intriguing possibility to study different kinds of ferromagnetic order in the same sample [54, 55, 56]. All of the above systems present interesting features that would deserve being mentioned. However, from now on, we will focus on spin phenomena occurring at *fractional* filling factors.

Soon after the discovery of the FQHE, Halperin suggested the existence of a ground state with partial spin polarization in the fractional quantum Hall regime. Exact diagonalization results by Chakraborty and Zhang [57, 58] indicated that such states can sometimes be energetically more favorable than the fully polarized ones depending on the interplay between the Zeeman energy E_z and the Coulomb energy $E_c = e^2/(\epsilon l_B)$.

There are (at least) three ways to manipulate the ratio E_z/E_c : applying a magnetic field parallel to the plane of the 2DEG, changing the g^* factor by hydrostatic pressure, lowering the magnetic field and/or the electron densities at constant filling factor. In the following sections we will briefly describe the three methods and mention some of the first evidences of spin-phase transitions obtained with the different configurations⁵.

At constant filling factor the Coulomb energy is given by the component of the magnetic field perpendicular to the 2D plane (B_\perp), since the motion of electrons is confined to that plane. Electron spins are not affected by this confinement, hence the Zeeman energy is proportional to the total magnetic field B . By tilting the sample with respect to the direction of the magnetic field, we can change the ratio

⁴The direct measurement of the spin-polarization of a 2DES at fractional filling factor was performed later by Kukushkin *et al.* [59].

⁵A more detailed review of results, both theoretical and experimental, regarding spin in FQHE was given by Chakraborty in 2000 [60].

between B_{\perp} and B , and thus between E_z and E_c . However, since B is always $\geq B_{\perp}$, we can only make the Zeeman energy larger than the Coulomb energy, and not the opposite. The first experiments concerning a spin phase transition in the FQHE are, to my knowledge⁶, those of Clark *et al.* [62] and Eisenstein *et al.* [63]. The experimental observation was that on tilting the sample the longitudinal resistivity at $\nu = \frac{4}{3}$ [62] and $\nu = \frac{8}{5}$ [63] shows a reentrant behavior: it had a pronounced minimum at zero tilt angle which disappears at large enough tilt and reappeared for yet higher angles (see Fig. 3.2a). The authors suggest that a transition to a fully spin polarized state occurs upon increasing the Zeeman energy by tilting the sample.

By applying hydrostatic pressure to a GaAs sample, it is possible to modify the

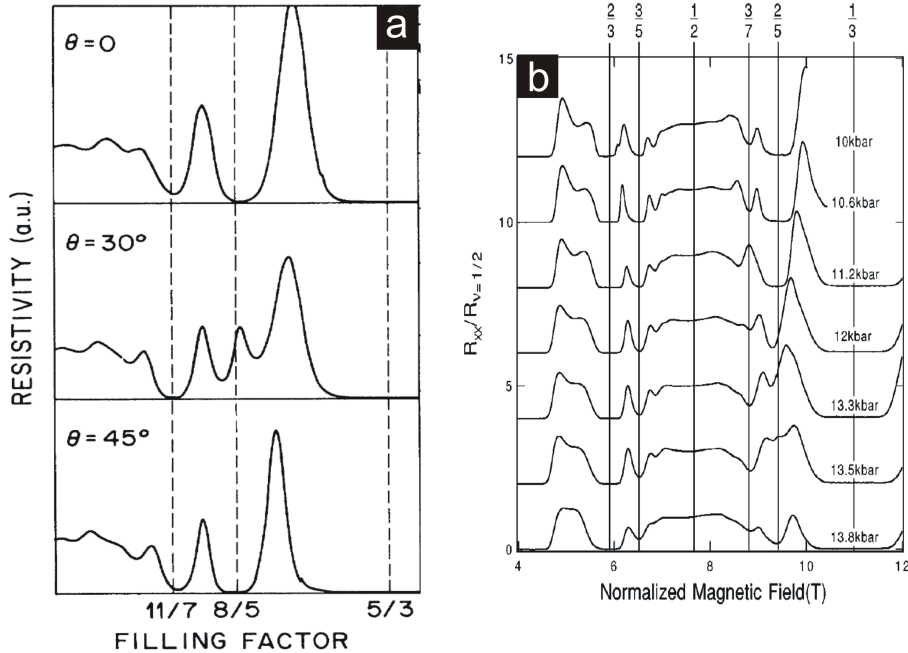


FIGURE 3.2: Spin transition of the ground state at filling factors $\frac{8}{5}$ and $\frac{2}{5}$ observed as a reentrant behavior of the QH states upon changing the ratio between Zeeman energy E_z and Coulomb energy E_c . The transition can be induced by tilting the sample in a magnetic field (a)(adapted from [63]) or by applying a hydrostatic pressure in order to change g^* (b)(adapted from [64]).

⁶In [61] Eisenstein *et al.* observed a rapid collapse of the $\nu = 5/2$ state upon increasing the angle. This represents the first observation of a fractional state whose ground state is not fully polarized, but no recovery of the state was reported after the collapse. We prefer not to include this work here as evidence of a spin phase transition.

spin-orbit coupling and decrease the g^* factor. Eventually, it is possible to achieve $E_z \propto g \sim 0$, but such experiments are technologically difficult. Morawicz *et al.* [65] were the first to study a fractional quantum Hall state under pressure, but they did not recognize the transition at $\nu = \frac{4}{3}$. Later experiments by Kang *et al.* [64] demonstrated the spin phase transition at filling factor $\frac{2}{5}$ as a reentrant behavior of the longitudinal resistivity as a function of the applied pressure (see Fig. 3.2b). Leadly *et al.* [66] achieved such a high pressure that they managed to make the g^* factor vanish. They presented data of activation energy gap measurements at $\nu = \frac{2}{5}$, $\frac{2}{3}$ and $\frac{1}{3}$ as a function of E_z/E_c . Interestingly, they were able to claim the existence of skyrmions at $\nu = \frac{1}{3}$, the CF analogy of skyrmions at $\nu = 1$.

Recently, experimental findings [67, 68] obtained at $\nu = \frac{2}{5}$ upon applying an hydrostatic pressure indicate that a transition between a spin-polarized and a spin-unpolarized state can be accompanied with phenomena reminiscent of ferromagnetism. Cho *et al.* [67] reported hysteretic phenomena at filling factor $\nu = \frac{2}{5}, \frac{3}{7}, \frac{4}{7}$ and $\frac{4}{9}$. They showed (for $\nu = \frac{2}{5}$) that hysteresis occurs only if the two spin ground states have similar energy (see Fig. 3.3a). Eom *et al.* [68] studied the temporal evolution of R_{xx} and found a logarithmic behavior without saturation (see Fig. 3.3b). In this article a comparison with magnetic materials is also presented.

Due to the different dependency of E_c and E_z on B or n , it is possible to change the ratio between Zeeman and Coulomb energy by just changing the magnetic field and/or the density. The latter option can be achieved in different ways: by changing the doping concentration during growth [69], by illuminating the sample and by using a metallic layer as a gate.

3.3.1 The spin in the CF picture

Even though the spin phase transitions can be satisfactorily understood by only considering the strongly correlated electron system, the weakly interacting CF picture provides a more intuitive way of understanding these phenomenon.

In Sec. 2.4.2, we explained that the CF Fermi-sea develops into a discrete series of LLs energetically separated by $\hbar\omega_c^*$ if $\nu \neq 1/2$. If we introduce the spin degree of freedom, we can further split these levels by the Zeeman energy $g^*\mu_B B$ as in the case of the IQHE. The latter splitting, however, depends on the external magnetic field and not on B_{eff} . Drawing the first CF LLs as a function of B_{tot} at tilted fields

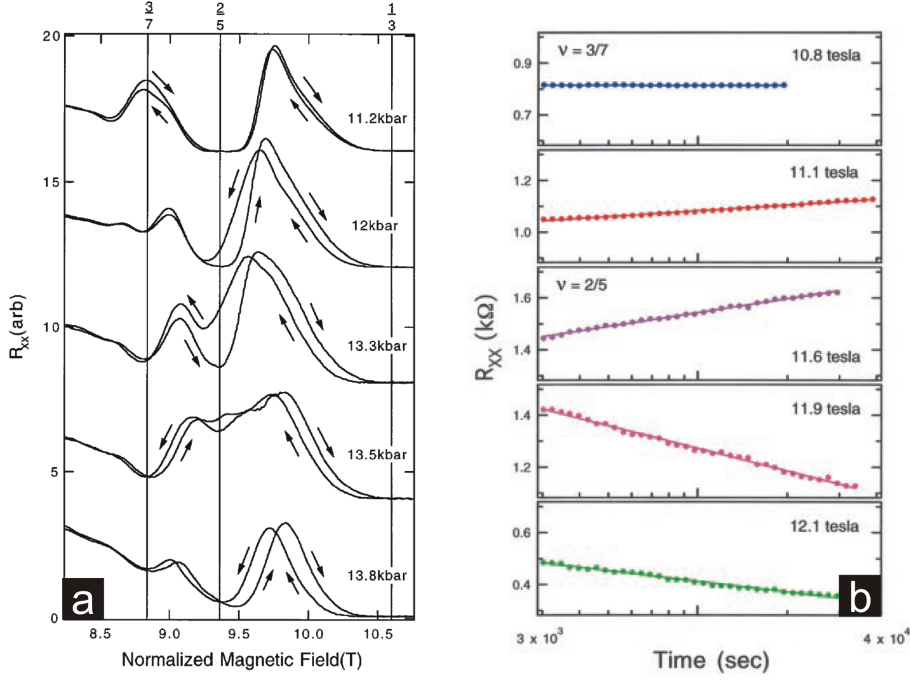


FIGURE 3.3: Cho *et al.* studied the spin phase transitions at $\nu = \frac{2}{5}, \frac{4}{7}, \frac{4}{9}$ by applying hydrostatic pressure in order to change the g^* factor (a) (adapted from [67]). They observed a dramatic hysteresis in the up and down magnetic-field sweeps in close proximity of these transitions. Using the same method, Eom *et al.* performed detailed temperature and time dependence measurements. They observed a logarithmic dependence, similar to what is observed in ferromagnetic materials (b) (adapted from [68]).

(or equivalently, as a function of n) and including the spin-splitting, the crossings of CF LLs become clear. This is plotted in Fig. 3.4 for the CF LLs $N = 0$ and 1. The spin-up level is depicted as a solid line, the spin-down is shown as a dashed line and the Fermi energy at $\nu_{CF} = 2$ as a thin dotted line. The splitting between two levels of same spin, for example $N = (0, \uparrow)$ and $N = (1, \uparrow)$ is given by the CF cyclotron energy $\hbar\omega_{c1}^*$ at field B_1 . The splitting between levels of different spin of the same CF LL, e.g. $N = (0, \uparrow)$ and $N = (0, \downarrow)$ is the Zeeman energy ($g^*\mu_B B_1$ at B_1). Considering the case of fixed filling factor $\nu_{CF} = 2$ as an example, we see that at low fields $\hbar\omega_{c1}^* > g^*\mu_B B_1$. The two CF LLs have different spin orientations and the polarization is therefore zero. The polarization is given by the following expression:

$$\mathcal{P} = \frac{N_{\uparrow} - N_{\downarrow}}{N_{\uparrow} + N_{\downarrow}}. \quad (3.1)$$

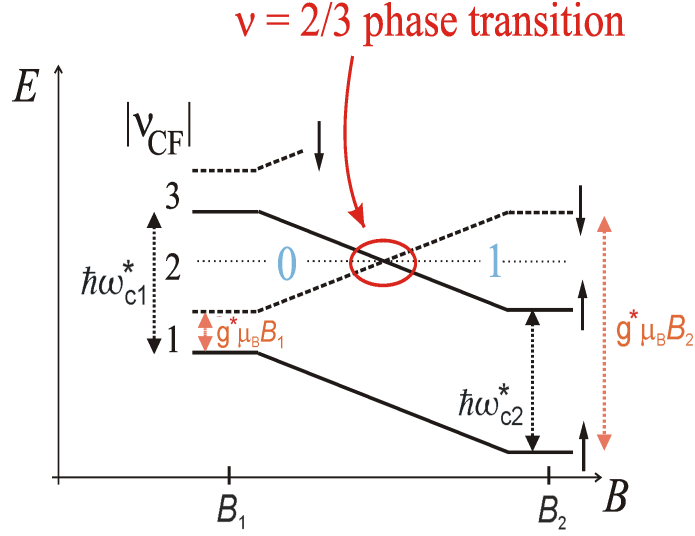


FIGURE 3.4: Spin-split composite fermion Landau levels. Since the CF cyclotron energy increases as \sqrt{n} or \sqrt{B} and the Zeeman energy as n or B , crossings between ground states of different polarizations exist. The thin-dotted line represents the Fermi level at $\nu_{\text{CF}} = 2$. For simplicity, we have connected the low field and the high field regions with straight lines. The polarization can be determined from $\mathcal{P} = \frac{N_{\uparrow} - N_{\downarrow}}{N_{\uparrow} + N_{\downarrow}}$ and its value is indicated on the Fermi energy line. At $\nu_{\text{CF}} = 2$ ($\nu = 2/3$), a transition occurs from $\mathcal{P} = 0$ to $\mathcal{P} = 1$ at $\hbar\omega_{\text{c}}^* = E_{\text{Z}}$.

where N_{\uparrow} (N_{\downarrow}) represents the number of electrons with spin-up (down). Increasing the magnetic field has a different effect on both energies. While the Zeeman splitting increases linearly with the field B , the CF cyclotron energy increases as \sqrt{B} ($m_{\text{CF}} \propto \sqrt{B}$). Therefore, at higher magnetic field, $\hbar\omega_{\text{c2}}^* < g\mu_B B_2$ and the two occupied CF LLs have the same spin orientation, i.e. the system is polarized⁷. A transition between $N = (0, \downarrow)$ and $N = (1, \uparrow)$ occurs whenever the CF cyclotron and the Zeeman energies are the same⁸:

$$\hbar\omega_{\text{c}}^* = \frac{\hbar e}{m_{\text{CF}}^{\text{p}}} |B_{\text{eff}}| = E_{\text{Z}} = g_{\text{CF}}^* \mu_B B_{\text{ext}}. \quad (3.2)$$

In this equation, m_{CF}^{p} is the CF polarization mass [71] and B_{eff} is given by equation 2.17. The CF g -factor g_{CF}^* has been measured to be largely the g -factor of the electrons g^* [72]. In references [73], [74] and [75], it is shown that the critical value

⁷Since the CF spin and the electron spin are the same, it is equivalent to refer to a CF or electron spin polarization [70].

⁸For simplicity, we have drawn straight lines from the low field to the high field region. It is however important to remember that the CF cyclotron energy increases as \sqrt{B} .

of spin transitions in the FQHE is more accurately described by the CF picture than by the Coulomb to Zeeman energy ratio of the electrons.

Due to the similarity between the experimental findings occurring at integer QHFs and at fractional quantum Hall states, and taking into account the analogy between electronic systems at $\nu = \frac{2}{3}$ or $\frac{2}{5}$ and composite fermion system at $\nu_{\text{CF}} = 2$, it was suggested already in 1998 [67] that the spin-phase instability at fractional filling factors can be described as the integer quantum hall ferromagnetism of composite fermions.

3.4 The spin phase transition at $\nu = 2/3$

Soon after the discovery of the FQHE, a lot of research was conducted for the study of the state at $\nu = \frac{2}{3}$.

Already in 1984 numerical calculations in small size systems by Chakraborty and Zhang [57, 58] showed that at small magnetic field the ground state is unpolarized, while at high field it is polarized, with a gapless region at intermediate fields. The first experimental evidence of a spin-transition at $\nu = \frac{2}{3}$ was provided by Clark and Maksym [76, 77]. They observed a reentrant behavior of the longitudinal resistance of the fractional state upon tilting the magnetic field,. Moreover, they also observed a splitting of the $\frac{2}{3}$ minimum at the angles where the minimum was the weakest. Later Eisenstein *et al.* [78] measured a reduction of the activation energy at $\nu = \frac{2}{3}$ either by changing the density or by tilting (see Fig. 3.5a). Their data were given as evidence for a transition between different spin-polarized ground states. Engel *et al.* [79] reported the splitting of the minimum in the longitudinal resistance at $\nu = \frac{2}{3}$ (i.e. the occurrence of a resistance peak at the phase transition) upon tilting the magnetic field (see Fig. 3.5b). They claim that this could be due to the coexistence of the two spin phases, polarized and unpolarized, in the ground state.

The experiments discussed above indicate the (co)existence of ground states with different spin polarization. In 1998 the experimental work of Kronmüller *et al.* [80, 81] presented unexpected phenomena occurring at the spin transition at $\nu = \frac{2}{3}$. They measured the longitudinal resistance of a 15 nm-wide quantum well as a function of the magnetic field. At small current they detected a tiny peak close to the $\frac{2}{3}$ minimum. On the other hand a sharp and huge peak around $\nu = \frac{2}{3}$ was observed at low magnetic field sweep rate and high enough current (Fig. 3.6a). This unexpected peak was named huge longitudinal resistance (HLR). The temporal evolution of this

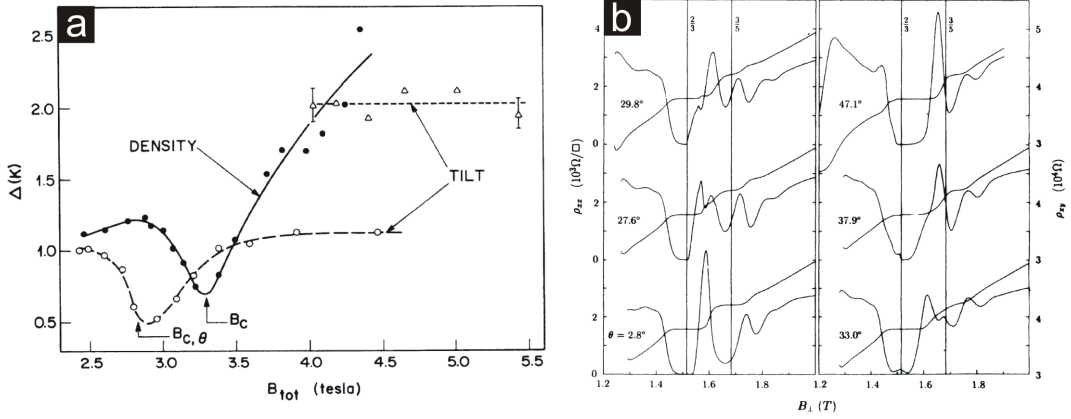


FIGURE 3.5: Eisenstein *et al.* studied the spin phase transitions at $\nu = \frac{2}{3}$ by changing the density and tilting the sample in a magnetic field (a). In both cases they find a minimum in the activation energy that they interpreted as evidence of a phase transition (adapted from [78]). Engel *et al.*, monitoring the longitudinal resistance at $\nu = \frac{2}{3}$ upon tilting the sample, found a splitting in the fractional minimum (b) (adapted from [79]).

HLR was measured by setting the magnetic field to an appropriate value and recording R_{xx} as a function of time. A monotonic increase and a subsequent saturation were found, where the typical times to form the HLR varied from minutes to several hours, with longer times for wider Hall bars (Fig. 3.6a inset). Both the longitudinal and Hall resistances show hysteretic behavior sweeping the magnetic field upwards and downwards. The authors suggest that at the transition the electronic system breaks up into domains of different spin configuration. The source of the HLR could be electron scattering at the domain walls. The long relaxation rates of R_{xx} observed in [82] suggested that the nuclear spins are involved into the formation of these domains via the hyperfine interaction. In order to prove this Kronmüller *et al.* [83] performed resistively detected nuclear magnetic resonance (RDNMR): they monitored the value of the longitudinal resistance while irradiating the sample with a radio-frequency signal. They detected a reduction of the value of the HLR whenever the irradiated frequency was corresponding to transitions between different spin states of the host material nuclei: ^{75}As , ^{69}Ga , ^{71}Ga , all having spin $I = 3/2$. The nuclear resonance peaks measured in R_{xx} were fourfold splitted; quite unexpected since the quadrupole moment allows only three resonance frequencies between the four states $I_z = \pm\frac{3}{2}$ and $\pm\frac{1}{2}$. The authors argued about a new kind of interaction

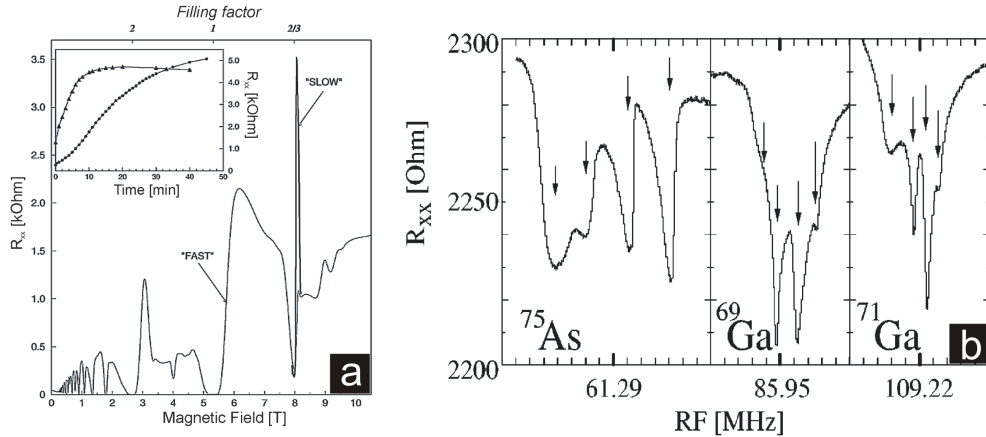


FIGURE 3.6: HLR at $\nu = \frac{2}{3}$ (a). When a small current is used, ρ_{xx} presents only a small peak close to $\nu = \frac{2}{3}$. When a large current is applied and the magnetic field is swept slowly, a huge peak in the resistance is detected. (a) inset shows the temporal evolution of the HLR peak for two different sample widths: $800 \mu\text{m}$ (indicated with dots) and $80 \mu\text{m}$ (indicated by triangles). Figure from [80]. (b) shows the response of the HLR upon irradiating the sample with a radio-frequency signal in resonance with the Larmor frequencies of the three host nuclei. The value of ρ_{xx} shows a fourfold splitting (from [83]).

between electrons and nuclei⁹. In a different type of device, but still using RDNMR, the expected threefold splitting at $\nu = \frac{2}{3}$ was detected by Smet *et al.* [85]. In the same work, Barkhausen steps (long known in magnetism [86]) in the temporal evolution of the resistance were found, bringing thus another analogy with magnetism. Kraus *et al.* [87] proposed that the quantum Hall ferromagnetism and the HLR at $\nu = \frac{2}{3}$ are just two different operating modes of the same spin-phase transition. In their work they accurately studied the longitudinal resistivity ρ_{xx} at the $\nu = \frac{2}{3}$ transition as a function of density and tilt angle, both in the low current regime, where just a small peak was observed at $\nu = \frac{2}{3}$, and in the high current regime at slow sweep rate, where the HLR showed up. They showed that the HLR develops exactly at the phase boundary between spin-polarized and spin-unpolarized ground state (Fig. 3.7). According to the authors, the small ρ_{xx} peak in the low current regime is due to back scattering of electrons *along* the domain walls. The increase in resistivity in the HLR regime is explained by scattering of electrons *across* the domain boundaries, involving nuclear spin polarization changes (flip-flop scattering)

⁹Later on, this fourfold splitting was found to be due to the mechanical strain of the sample caused by the glue used in the experiment [84].

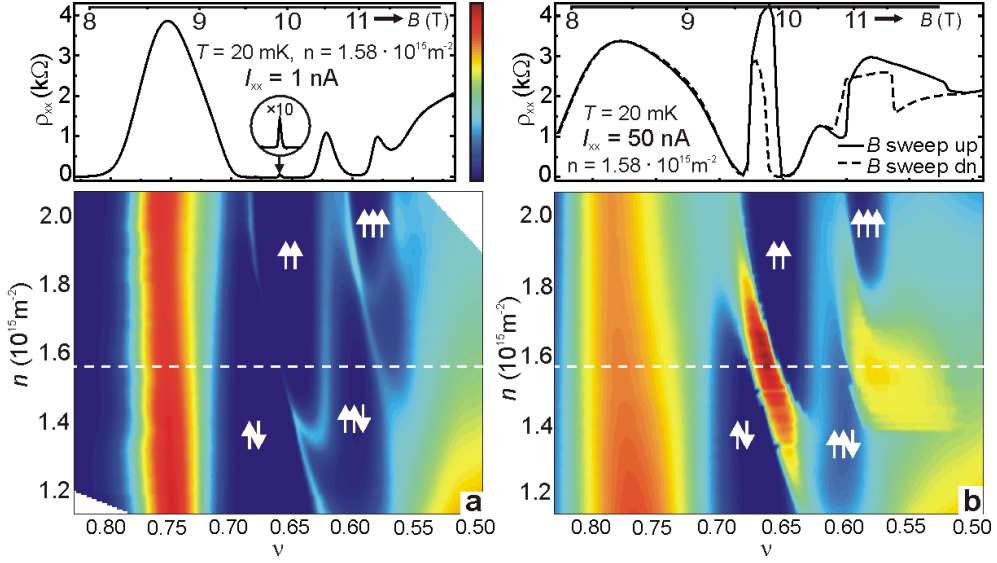


FIGURE 3.7: The two different modes of operation of the spin phase transition at $\nu = \frac{2}{3}$. The main graphs show color plots of the longitudinal resistance as a function of filling factor and density. The top traces show ρ_{xx} at the fixed density indicated by dashed lines in the main graph. In the low current regime (a) a small peak separates the regions of spin-polarized and spin-unpolarized ground state. In the high current regime (b) the HLR develops at the phase boundary. Figure from [87].

due to hyperfine interaction.

This last process allows the control of the nuclear spin polarization by manipulating the electron system at $\nu = \frac{2}{3}$ [88, 89, 90, 91, 92]. In particular, Hashimoto *et al.* [93] showed that the HLR is completely suppressed when the potential of the QW hosting the 2DES is made very asymmetric by gate voltages. Furthermore, they find that the nuclear spin relaxation time is also modified by this asymmetry. They argued that this is due to the enhancement of the SO interactions. The SO mixes LLs with opposite spins making the electron spin component along the magnetic field direction no longer a conserved quantity. Therefore, electron spin-flips can occur without nuclear spin-flops, facilitating the transport across the domain walls. As discussed above, many experimental works studied the QHF at $\nu = \frac{2}{3}$. These works concern the detection of the longitudinal resistivity with low-frequency techniques. The different authors find unexpected transport properties at filling factor $\frac{2}{3}$. However, they could not find evidence of domains or convincing arguments about the physical origin of their experimental results. For this reason a different technique has to be employed.

3.4.1 Electron spin polarization at $\nu = \frac{2}{3}$

The electron spin is involved in the transition at $\nu = \frac{2}{3}$. Here we review some of the experiments that allowed the direct measurement of the spin polarization at this filling factor.

Kukushkin *et al.* [59] employed an optical technique to measure the polarization of a 2DES at several filling factors. A metallic gate was used, and the electronic polarization was studied at a fixed filling factor and a variable density and magnetic field. At $\nu = \frac{2}{3}$, this experiment confirmed that the polarization is zero for low Zeeman energy and one for high Zeeman energies, as expected for a spin-unpolarized and a fully spin-polarized ground state. However a kink at the value of one half was observed at the transition between these two polarization values, (Fig. 3.8).

Freytag *et al.* [94] used the Knight shift of the NMR signal of a multiple quantum well structure as a probing tool for the electron polarization. The device consisted of many (100) quantum wells separated by barriers wide enough that the wells can be considered as independent. They measured that the fully polarized state at $\nu = \frac{2}{3}$ turned into a stable ground state with \mathcal{P} approximately 0.775 when the Zeeman energy was decreasing (Fig. 3.9). However, in this experiment a low enough Zeeman energy for the unpolarized ground state to take over was not obtained. The result of Freytag *et al.* is in contradiction with the one of Kukushkin *et al.*, and the scientific community agrees in considering the finding of Freytag *et al.* as an experimental artifact.

More recently, Stern *et al.* [95] measured the electron polarization of a single QW by using a technique that combines RDNMR with standard NMR. The absolute degree of electron spin polarization can be determined by measuring the Knight shift of the nuclei interacting with electrons and comparing the results with the nuclear signal in the absence of the 2DES. The Knight shift was measured by RDNMR, while the unshifted signal is obtained with standard NMR techniques. They showed that at $\nu = \frac{2}{3}$, both in the low and high current regime, the RDNMR signal shows two resonance features. One can be assigned to an unpolarized system ($\mathcal{P} = 0$), while the other one to a fully polarized one ($\mathcal{P} = 1$) (Fig. 3.10).

The results presented in this section give strong evidence of the presence of (at least) two different spin polarization values at $\nu = \frac{2}{3}$.

However, the morphology of the domains and the type of excitations at the transition are not understood.

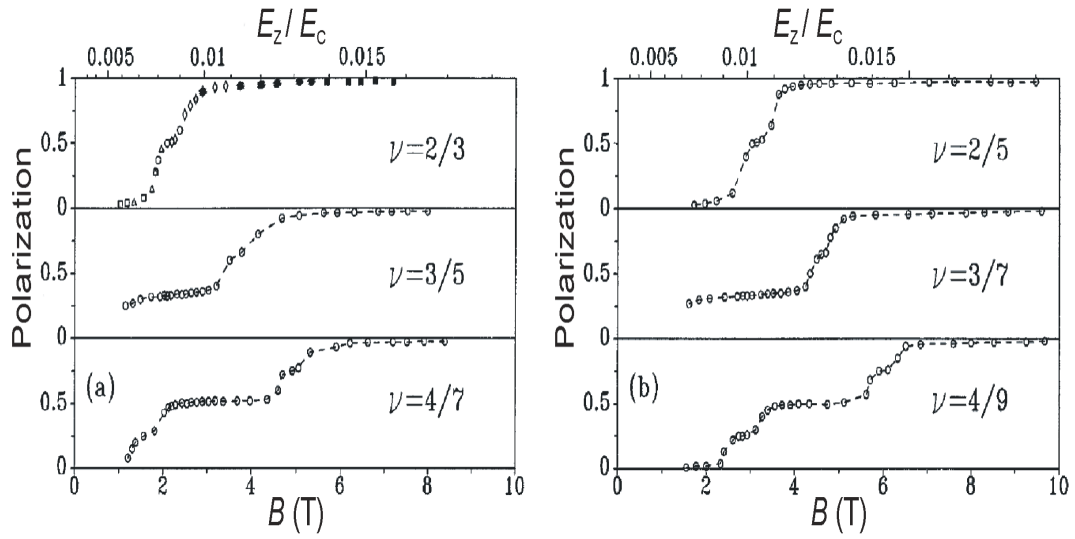


FIGURE 3.8: Electron spin polarization at different filling factors measured with an optical technique by Kukushkin *et al.*. Concerning $\nu = \frac{2}{3}$, at low Zeeman energy the system is unpolarized (polarization = 0), while at high Zeeman energy it is fully polarized (polarization = 1). Between these two regimes, a feature at polarization = 0.5 is detected. Figure adapted from [59].

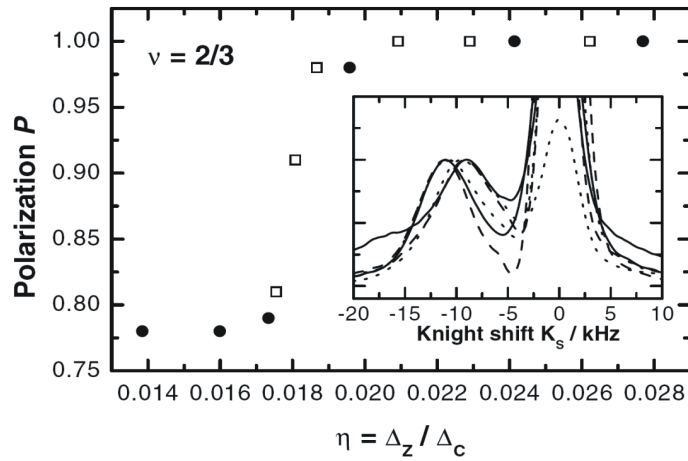


FIGURE 3.9: Electron spin polarization at $\nu = \frac{2}{3}$ measured by Freytag *et al.* with NMR techniques. The sample is a multiple quantum well structure. Reducing the Zeeman energy, the system moves from a fully polarized state (polarization = 1) to a partially polarized state (polarization = 0.775). The inset shows the normalized NMR spectra. Figure from [94]

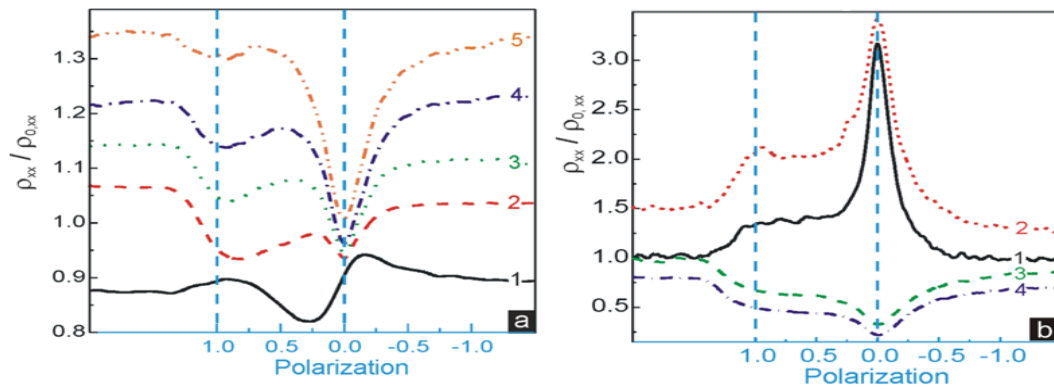


FIGURE 3.10: Resistance Detected NMR at $\nu = \frac{2}{3}$ in the low current regime (a) and in the high current regime (b). The signal presents two resonance features when the sample is irradiated with a RF signal in resonance with the Larmor frequency of the host nuclei. Combining a standard NMR technique, Stern *et al.* were able to assign these two features to a system fully polarized ($\mathcal{P} = 1$) or unpolarized ($\mathcal{P} = 0$). Figure adapted from [95]

4 Experimental techniques and setup

In this chapter we describe the different techniques that we used in the investigation of the spin phase transition at $\nu = \frac{2}{3}$.

In our work we employ a technique based on the detection of high frequency surface acoustic waves (SAW) together with quasi-DC transport measurements. In Sec. 4.1 we describe the basic properties of the propagation of a SAW on GaAs. The mechanism of interaction of a SAW with a 2DES is described in Sec. 4.2 where we also present the technique that we employ. A great part of the work concerns the design and the realization of a setup that allows the detection of SAW transmission with a good signal to noise ratio. For this reason, the sample preparation and the experimental apparatus are described in detail in Sec. 4.3.

4.1 Surface acoustic waves on piezoelectric materials

Surface acoustic waves are modes of elastic energy propagating along the surface of a crystal [96]. The amplitude of the wave decays almost exponentially into the bulk and nearly all of the energy is contained within a wavelength from the surface. The physical motion of this wave is associated mechanically with a time-dependent elliptical displacement of the surface structure (Fig. 4.1(a)). One component of this displacement is parallel to the SAW propagation axis, while the other is normal to the surface. On piezoelectric materials such as GaAs a mechanical strain produces an electric field and, conversely, an applied electric field produces a mechanical strain in the crystal. Hence, in GaAs, the propagation of a SAW is accompanied by an elastic field and an electric field.

One of the most frequently used ways to generate SAWs is through the use of interdigital transducers (IDTs). An IDT (Fig. 4.1(b)) consists of an array of interleaved metal electrodes deposited on a piezoelectric substrate. Applying an alternating voltage to the contacts will cause a spatial strain distribution of periodicity P in the crystal below. If the frequency (f_0) of the applied voltage is such that the periodicity is equal to the wavelength $\lambda = \frac{v_{\text{SAW}}}{f_0}$ (with v_{SAW} the velocity of the acoustic

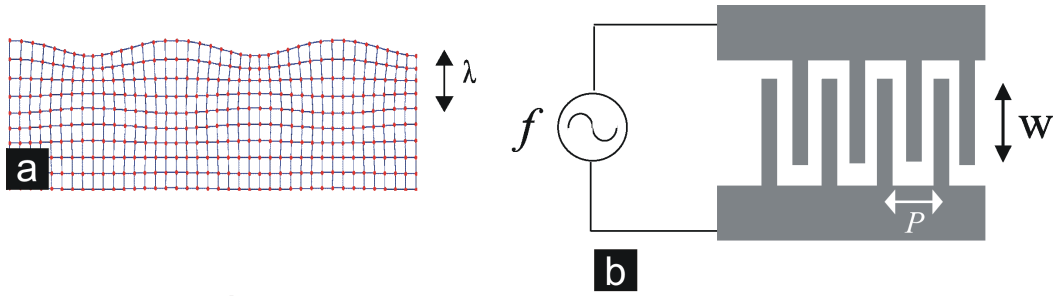


FIGURE 4.1: Sketch of the particle displacement in a medium due to a surface acoustic wave (a). The main energy flow is concentrated within a distance of the order of a wavelength beneath the surface. Cartoon of an interdigital transducer (b). When an oscillating voltage of frequency $f_0 = v_{\text{SAW}}/P$ is applied, a surface acoustic wave is generated.

wave), SAWs are generated in both directions perpendicular to the electrodes. Consequently, the periodicity of the electrodes determines the fundamental resonance frequency of the IDT for a particular material. Two IDTs are required in a basic SAW device configuration. One of these acts as the device input and converts voltage variations into mechanical acoustic waves. The other IDT is employed as an output receiver and converts mechanical SAW vibrations back into output voltages. To characterize the different crystal axis and SAW propagation directions, the electromechanical coupling coefficient k_{eff}^2 is usually defined. This parameter is a measure of the efficiency of a given piezoelectric material in converting an applied electrical signal into the mechanical energy associated with a SAW. The higher k_{eff}^2 , the more efficiently a material is able to generate and detect SAWs. When the surface is covered with a conducting metal film the time-varying electric field associated with the SAW causes the metal surface film to accumulate charge. If the SAW propagation is modeled as an equivalent electrical transmission line LC , the additional charge accumulation increases C . Since the electromagnetic wave velocity of a transmission line is proportional to $1/\sqrt{C}$, an increase in C will decrease the velocity.

In a piezoelectric crystal like GaAs, an acoustic wave can couple to mobile charge carriers via the associated longitudinal electric field with it¹.

The next section will describe first the interaction of an acoustic wave in bulk materials and then move onto the case of a SAW interacting with a 2DES.

¹In most of the cases the effect of the deformation potential due to the elastic field is much smaller than the effect of the electric field.

4.2 Magneto-acoustic interactions mechanism

Let us consider a small static deformation of an elastic solid. We can define two second-rank tensor parameters [97]: the stress $\{T\}$ and strain $\{S\}$.

The stress is the force \mathbf{F} applied per unit area \mathbf{A} of the solid and its component can be written as $T_{ij} = F_i/A_j$ with $i, j = x, y, z$. The strain represents the fractional deformation due to the force \mathbf{F} and can be defined as $S_{ij} = \Delta_i/L_j$, where Δ is the fractional deformation of the solid of length \mathbf{L} . The stress and strain tensors can be reduced to matrices of six elements (indicated as $[T]$ and $[S]$) by symmetry arguments. The equations of state describing the propagation of elastic waves in piezoelectric materials are [98]

$$[T] = [c][S] - [e_{pz}]^t \mathbf{E} \quad \text{and} \quad \mathbf{D} = [e_{pz}][S] + [\varepsilon] \mathbf{E} \quad (4.1)$$

where \mathbf{E} is the electric field, \mathbf{D} the electric displacement field, $[c]$ is the elastic stiffness, $[e_{pz}]$ is the piezoelectric constant and $[\varepsilon]$ the electrical permittivity.

For SAWs propagating in piezoelectrics materials the electromechanical coupling coefficient k_{eff}^2 can be defined as [98]

$$k_{eff}^2 = \frac{e_{pz}^2}{c\varepsilon} \quad (4.2)$$

where the tensor subscripts have been dropped.

The analysis of the propagation of a SAW in a piezoelectric material with a finite conductivity σ has been completed by various authors [99, 100]. Here we just present the main results: the propagating electric field E accompanying the SAW can couple to the mobile carriers in the material and leads to induced currents and associated ohmic losses σE . This transfer of power from the wave is observed as an attenuation and velocity shift of the SAW as a function of the conductivity. In a simple relaxation model, in the linear regime, the attenuation Γ and the velocity shift Δv are, respectively

$$\Gamma = \frac{\omega k_{eff}^2}{v} \frac{\omega_{cr}/\omega}{2(1 + (\omega_{cr}/\omega)^2)} \quad \text{and} \quad \frac{\Delta v}{v} = \frac{k_{eff}^2}{2} \frac{1}{1 + (\omega_{cr}/\omega)^2} \quad (4.3)$$

where $\omega_{cr} = \sigma/(\varepsilon_1 + \varepsilon_2)$, with ε_1 (ε_2) the dielectric constants of the half-space above (below) the crystal surface. The conductivity relaxation frequency ω_{cr} is the rate at which the electron system relaxes back to the equilibrium distribution. If the sound frequency ω is much smaller than ω_{cr} the carriers will be able to redistribute

themselves rapidly enough to screen the external piezoelectric field. This results in inducing a periodically-spaced charge wave traveling in phase with the SAW. In the present context the electric field is effectively screened by the carriers and no loss of energy will occur. This is the situation for a perfect conductor. As the conductivity falls, the time required for a charge wave to build up increases and a situation arises where, as the elastic wave moves on, the charge carriers are no more able to screen the electric potential. This imperfect screening of the SAW potential causes a finite dissipation. The maximum attenuation occurs when the SAW frequency equals the conductivity relaxation frequency ($\omega = \omega_{cr}$). Finally, if the frequency ω becomes much greater than ω_{cr} , the electron distribution can no longer respond to the acoustic wave. The inability to screen the field of the SAW results in a maximum piezoelectric stiffening of the crystal. No charge wave is induced, hence the current is zero and the associated acoustic losses are minimal. In this situation the material behaves as an insulator. We can model the 2DES as a thin sheet of mobile carriers with sheet conductivity σ_{\square} located directly on top of the crystal. Let us also suppose that the thickness of this conducting layer is much smaller than the SAW wavelength. In this situation, the longitudinal electric field of the SAW can be screened only at the surface. Restricting the conductivity to a thin sheet results in a modification of the conductivity relaxation frequency ω_{cr} , that becomes [101]

$$\omega_{cr} = \frac{\sigma_{\square} k}{(\varepsilon_1 + \varepsilon_2)} \quad (4.4)$$

where $k = 2\pi/\lambda$ is the wavevector of the SAW. Eq. 4.3 becomes now

$$\Gamma = \frac{\omega}{v} \frac{k_{eff}^2}{2} \frac{\sigma_{\square}(\omega)/\sigma_m}{1 + (\sigma_{\square}(\omega)/\sigma_m)^2} \quad \text{and} \quad \frac{\Delta v}{v} = \frac{k_{eff}^2}{2} \frac{1}{1 + (\sigma_{\square}(\omega)/\sigma_m)^2} \quad (4.5)$$

where $\sigma_m = v(\varepsilon_1 + \varepsilon_2)$ is independent of the frequency. Eq. 4.5 tells us that the attenuation and the velocity shift of a SAW on a piezoelectric substrate containing a 2DES is controlled by the sheet conductivity. In a magnetic field we have to consider the magnetic field induced anisotropy of the conductivity tensor. If the longitudinal electric field accompanying the SAW lies in the x direction, σ_{\square} has to be replaced by $\sigma_{xx}(B)$. Thus, in a 2DES in a Hall bar geometry, the relaxation interaction is strongest for $\sigma_{xx} \simeq \sigma_m$ (Fig. 4.2). For GaAs the characteristic conductivity σ_m , when liquid ^3He is above the surface, is approximately $3.6 \times 10^{-7} \Omega^{-1}$.

Eq. 4.5 tells us that by monitoring the attenuation and the velocity shift of a SAW we can probe the conductivity of the 2DES at a frequency much higher than using

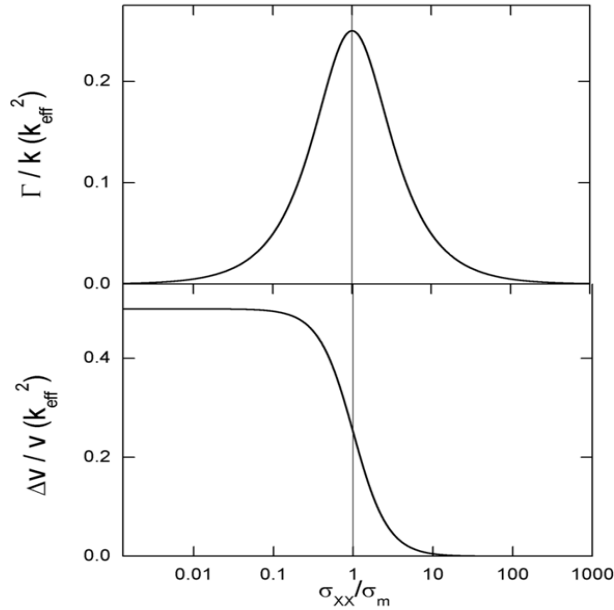


FIGURE 4.2: Attenuation (upper panel) and velocity shift (lower panel) of a surface acoustic wave as function of the conductivity as predicted from Eq. 4.5.

quasi-DC techniques. Moreover, with standard quasi-DC techniques we measure the sum of resistivities of the 2DES while with SAW technique we probe its conductivity at the length scale given by the acoustic wavelength.

The above model was originally derived for systems in the absence of an applied magnetic field under the assumptions that $kl \ll 1$ and $\omega\tau \ll 1$ (with l mean free path). If a magnetic field is applied, the first condition has to be replaced by kR_C where R_C is the cyclotron radius. The regime of validity of these conditions is called *local regime* [102, 103, 104, 105]. Many experiments show the validity of this relaxation model in a wide range of frequencies and magnetic field strengths [106, 107, 108, 109, 110, 111, 112].

Wixforth *et al.* [106] studied a 2DES at integer filling factor using a SAW frequency of about 70 MHz (see Fig. 4.3). The agreement between the experiment and Eq. 4.5 is extremely good.

Some deviations from the relaxation model of Eq. 4.5 are observed at very high frequency and strong magnetic field, when the surface acoustic wavelength becomes comparable with the length scale characterizing the electron system. Willett *et al.* [113, 114, 115, 116, 117] used SAW of very high frequency (up to 7.8 GHz) to study the electron correlations in the fractional quantum Hall regime. One of the main

results of their study is the measurement of a Fermi sea at $\nu = \frac{1}{2}$ which is evidence for the composite fermion picture of the FQHE. This was achieved by studying the velocity shift of a SAW for different sound wavelengths. At $\nu = \frac{1}{2}$, a peak in Γ and Δv was predicted by using Eq. 4.5. However, when the SAW wavelength was comparable to the quasi-particle mean free path, they detected instead a dip in both the attenuation and the velocity shift (Fig. 4.4).

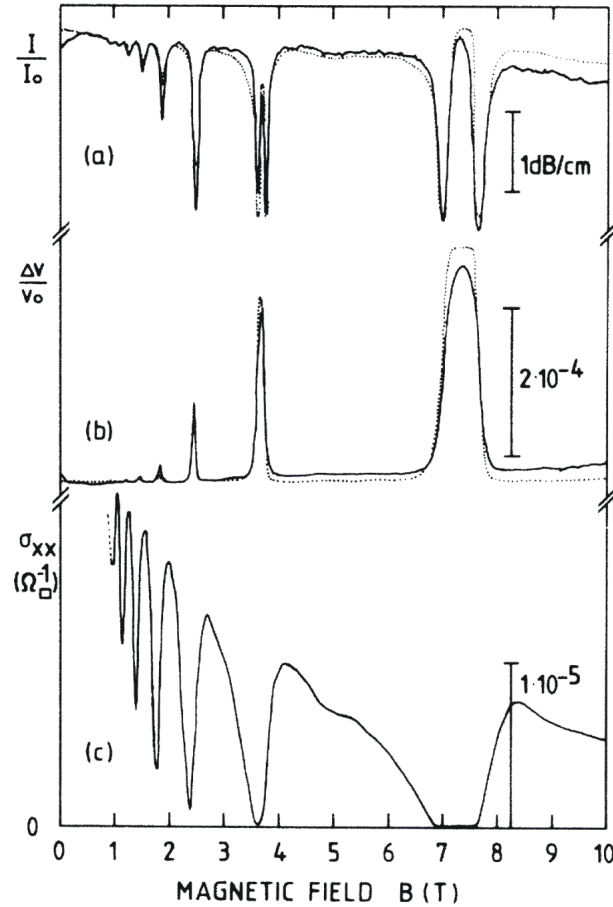


FIGURE 4.3: SAW measurement of a 2DES in the integer quantum Hall regime with an acoustic frequency of 70 MHz. The transmission and the velocity shift on the SAW are shown together with the conductivity of the 2DES. The solid lines are experimental data, while the dotted lines are obtained using Eq. 4.5. The agreement is very good. Figure from [106].

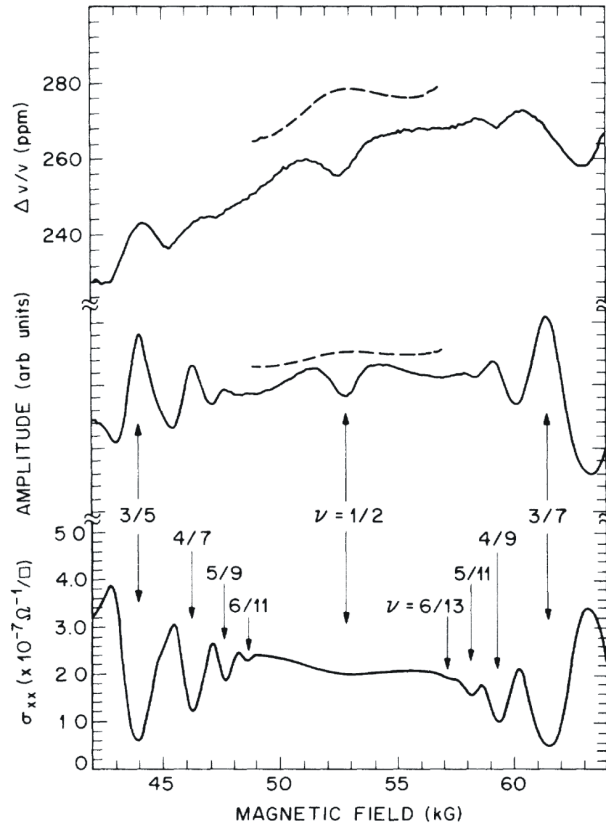


FIGURE 4.4: SAW measurement of a 2DES in the fractional quantum Hall regime with an acoustic frequency of 700 MHz. The amplitude and the velocity shift of the SAW are shown together with the conductivity of the 2DES. The solid lines are experimental data, while the dashed lines are obtained using Eq. 4.5. At filling factor $\frac{1}{2}$, Eq. 4.5 predict a peak in both amplitude and velocity shift of the SAW. Instead, a dip was experimentally detected (solid lines). The local-regime conditions are not fulfilled since the acoustic wavelength becomes comparable with the CF mean free path, so Eq. 4.5 is not valid any more. Figure from [113].

4.2.1 Acousto-electric effect

A well-defined momentum characterizes a SAW. When the traveling electrostatic potential of the wave interacts with a 2DES it perturbs the electron density and transfers part of the momentum to the mobile carriers. This will induce drag currents and voltages depending on the experimental configuration. This is the acousto-electric effect (AE) [118]. In the following section we derive the expression for the acousto-electric effect based on the theory of Falko *et al.* [119].

For piezoelectric materials a SAW propagating along the x direction is accompanied

by an electric field $E_{\text{SAW}}(x, t) = -\frac{\partial}{\partial x}\Phi(x, t) = E_0 e^{i(kx - \omega t)}$ where Φ is the varying potential of the SAW. As mentioned previously the mobile carriers in the 2DES screen this field. This leads to an effective electric field

$$E_{\text{eff}} = \frac{E_{\text{SAW}}}{1 + i(\sigma_{\text{xx}}/\sigma_{\text{m}})}. \quad (4.6)$$

The action of the effective electric field is to perturb the density of the mobile carriers. The non-linear second-order density perturbation leads to a finite acoustoelectric drag current within the 2DES. This (time-averaged) drag current j^{ac} can be expressed in the form

$$j_i^{ac} = \Lambda_{il} \frac{I\Gamma}{v} = \Lambda_{il} Q_l. \quad (4.7)$$

Here I denotes the acoustic intensity of the wave and is related to the attenuation Γ by $I = I_0 \exp(-\Gamma x)$. Q represents a 'phonon pressure' while Λ_{il} is the acoustoelectric tensor. Thus a SAW of intensity I is attenuated by the 2DES and a momentum Q is transferred to the mobile carriers. The drag current causes a DC electric field to appear which in turn causes an ohmic current to flow in the 2DES. In the presence of a magnetic field this electric field causes also a Hall current to appear.

Falko *et al.* found the acoustoelectric tensor to be given by

$$\Lambda_{il} = -\frac{\partial \sigma_{il}}{\partial n}, \quad (4.8)$$

with n the electron density. The derivatives of the conductivity may be expressed as

$$\frac{\partial \sigma}{\partial n} = \frac{\partial \sigma}{\partial \nu} \frac{\partial \nu}{\partial n} = \frac{\nu}{n} \frac{\partial \sigma}{\partial \nu}. \quad (4.9)$$

In our experiments all the contacts are left open and no macroscopic current is permitted. With this boundary condition, using the expression for the LL filling factor $\nu = \frac{n\hbar}{eB}$ and recalling that

$$\bar{\sigma} = \begin{pmatrix} \sigma_{\text{xx}} & \sigma_{\text{xy}} \\ \sigma_{\text{yx}} & \sigma_{\text{yy}} \end{pmatrix} = \bar{\rho}^{-1} = \frac{1}{\rho_{\text{xx}}\rho_{\text{yy}} - \rho_{\text{xy}}\rho_{\text{yx}}} \begin{pmatrix} \rho_{\text{yy}} & -\rho_{\text{xy}} \\ -\rho_{\text{yx}} & \rho_{\text{xx}} \end{pmatrix},$$

we end with the following expressions for the electric field components

$$E_x = \frac{\Gamma I}{ven} \left(\nu \rho_{\text{xy}} \frac{\partial \sigma_{\text{yx}}}{\partial \nu} + \nu \rho_{\text{xx}} \frac{\partial \sigma_{\text{xx}}}{\partial \nu} \right) \quad (4.10)$$

and

$$E_y = \frac{\Gamma I}{ven} \left(\nu \rho_{yx} \frac{\partial \sigma_{xx}}{\partial \nu} + \nu \rho_{yy} \frac{\partial \sigma_{yx}}{\partial \nu} \right). \quad (4.11)$$

Eq. 4.10 and Eq. 4.11 will be used in Sec. 5.5 to interpret the experimental findings of the acoustoelectric measurements.

4.3 Setup

In the previous section we showed how it is possible to obtain complementary information about the electronic properties of the 2DES using quasi-DC and SAW measurements. In the rest of this chapter we will explain how these measurements are conducted. One of the main requirements is to have a device that allows the realization of low and high frequency (HF) measurements with the best possible efficiency. This will be discussed in Sec.4.3.1. The second important requirement is to have a measurement setup with high enough signal to noise ratio, in order to obtain reliable results. Our system will be outlined in Sec. 4.3.2.

4.3.1 Sample preparation

Fig. 4.5 shows one of our typical devices. We start with a MBE-grown wafer containing a 15 nm GaAs quantum well imbedded between $\text{Al}_x\text{Ga}_{1-x}\text{As}$ barriers doped with a layer of Si donors. A Hall bar 900 μm long and 200 μm wide is defined by standard photolithography and wet chemical etching. Eight ohmic contacts to the 2DES are achieved by deposition of Au/Ge/Ni (3016/1538/900Å) in a vacuum chamber and subsequent annealing at 370°C for 120 s and at 440°C for 50 s in a N_2 atmosphere at 300 mbar. These ohmic contacts are used for the quasi-DC measurements. After the ohmic contacts, single-finger IDTs are fabricated using photolithography (for fundamental frequencies up to 450 MHz) and subsequent evaporation of 80-100 nm of Al. Finally, as last step of the preparation of our device, pads of Ti/Au (15/150 nm) are deposited over the ohmic contacts and the transducer pads.

In the following section we discuss the design factors for the IDTs.

Since the frequency response of a SAW delay line allows only the transmission of frequencies close to resonance [98], we will refer to our device as a SAW (bandpass) filter.

An important consideration when designing the SAW devices is the spatial separation of the transducers. The size of the package and spatial constrictions within

the cryostat determine the maximum separation of the IDTs. Sufficient delay is required to allow the delayed SAW pulse to be time-resolved from the electromagnetic breakthrough between the RF lines. A greater separation would enhance the sensitivity of the device as the wave would propagate over a longer interaction region. Furthermore it is desirable to have the IDTs far from the 2DES in order to reduce the electromagnetic cross-talk. Trading these factors against the inherent propagation losses and considering the restrictive limits imposed by the package, an IDT separation of about 2.3 mm was chosen, yielding a SAW delay time τ_{SAW} of about 800 ns.

The second important point is the direction along which the transducers have to be oriented. In general, SAW piezoelectric substrates are anisotropic. This means that their SAW propagation characteristic is not the same in all directions. This can lead to an effect known as beam steering², which can degrade the response of a SAW delay line [96, 121]. The reason for this is that in anisotropic media the flow of power is not necessarily perpendicular to the phase front. Instead, it makes an

²Also known as phonon focusing (see for example [120]).

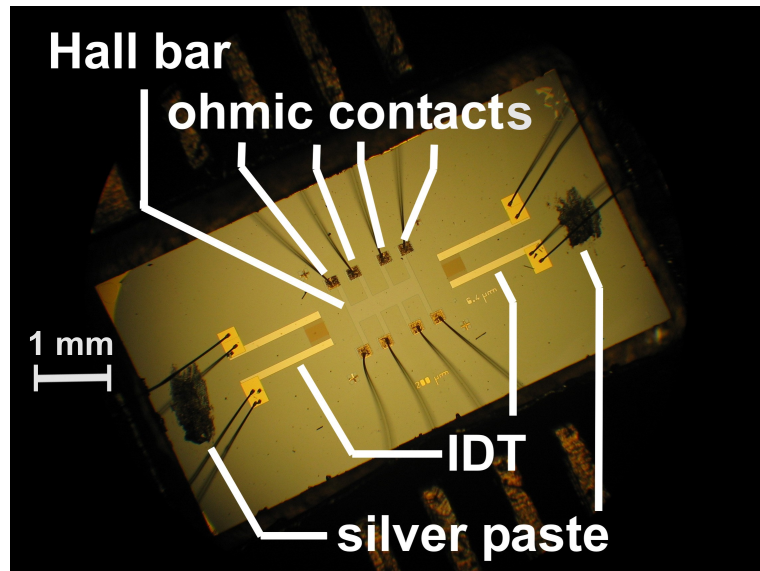


FIGURE 4.5: A top-view image of one of our devices. The IDTs, the Hall bar and the ohmic contact are indicated, together with the silver paste used to damp the wave reflected by the edge of the crystal. The IDTs have a fundamental frequency of 450 MHz. See text for the details of preparation. The scale is shown by the horizontal bar on the left.

angle α with the perpendicular given by

$$\alpha = \frac{1}{v} \frac{dv}{d\theta} \quad (4.12)$$

where θ is the angle between the propagation direction and the crystal axis. This means that only those directions in which the velocity is a maximum or a minimum can be used for SAW devices. Improper alignment of an IDT with the required crystal direction can also result in beam steering [121]. The next restriction comes from the requirement of strong piezoelectric coupling. For the reasons mentioned above, in our devices, the IDTs are oriented along the [110] direction on the (001) plane of GaAs, which has k_{eff}^2 of 6.4×10^{-4} and a SAW velocity of 2863 m/s [122, 123].

For the fabrication of a SAW delay line thin metal films are deposited to form IDTs. These films need to be light enough so that they do not damp the surface wave excessively. Because of its low density we employ Al. The metal films should be as thin as possible but at the same time should provide good electrical contact and low resistance. In our structure we used a thickness between 75 nm and 100 nm.

Until now we focused on the fundamental resonance frequency. A single-finger IDT structure like the one showed in Fig. 4.5 can operate at harmonic frequencies as well. This harmonic use is attractive for three reasons: first it enables gigahertz SAW filters to be fabricated with standard photolithography techniques. Second, the use of harmonics can be useful when the response at the fundamental frequency is degraded by bulk wave interference. Third, harmonic operations allow the study of the response of the same 2DES at different frequencies without changing the environmental conditions. The frequency response at harmonics depends strongly on the ratio between the width of a single electrode and the distance between two consecutive ones. In order to enable the generation of as many harmonics at low frequency as possible, a ratio metallized:unmetallized regions of 3:2 was chosen. Within our devices we managed to excite up to the 11th harmonic.

So far we have only analyzed the behavior of the SAW filter alone. In reality it is connected to some external circuit and requires impedance matching. The impedance of the IDTs can be adjusted to match the external source (usually 50 Ω) by varying the width of the acoustic beam set by the aperture W (see Fig. 4.1).

The last parameter to consider in the design of the transducers is the number of finger pairs N , which is related to the bandwidth Δf of the SAW filter by the

relation

$$\frac{\Delta f}{f} = \frac{1}{N}. \quad (4.13)$$

In order to have more acoustic power one should have a larger N . However, increasing N will reduce the bandwidth of operation of the filter. Moreover, higher N implies a higher value of the capacitance of the IDT and maintaining impedance matching becomes difficult. Our IDTs have $N = 40$.

An IDT generates SAWs in both directions, towards the Hall bar and the crystal edge. A spot of a two-component silver paste is applied behind the IDTs to damp the incoming acoustic waves (see Fig. 4.5) that could be reflected by the sample edge and degrade the performance of the transducers. The input transducer generates not only SAWs but also waves propagating into the bulk in any direction. Some of these waves can be reflected at the bottom of the crystal and reach the output transducer modifying the response of the filter. To reduce this effect, the devices are glued onto the sample holder with the same silver paste as before in order to absorb most of the bulk waves.

Many other sources contribute to decrease the performance of the SAW filter [98]. An inherent insertion loss is associated with the geometry of the device itself. When excited by an alternating voltage the IDT generate surface acoustic waves in both directions. This inherently causes a 3 db insertion loss since part of power is lost in this unwanted process. Moreover, some of the SAW power received at the output transducer is radiated back through the piezoelectric effect. The portion reflected back to the input transducer can lead to further generation of SAWs from the input towards the output transducer. This new wave will then arrive at the output transducer delayed by $2\tau_{\text{SAW}}$ with respect to the main SAW pulse (so the name Triple Transit Echo) and produce ripples in the frequency pattern. In modern SAW technology some tricks or special IDT geometries are used to reduce these (and many more) second-order effects. They mainly consist in increasing the performance of a SAW filter at one, and only one, operation frequency. Since we prefer to have a good frequency response at all harmonics, such solutions were not adopted. Moreover the limited space in our cryostat, together with the presence of the Hall bar along the propagation path, makes many of these solutions not applicable.

After describing how to prepare a device for generating and detecting surface acoustic waves we turn to the requirements for the 2DES in order to be studied with SAWs.

As shown in Fig. 4.2, the changes in the attenuation and velocity shift of a SAW are more dramatic when the conductivity of the 2DES is similar to σ_m , which in GaAs is a small quantity (in our experiments $3.6 \times 10^{-7} \Omega^{-1}$). Therefore, in SAW measurements, any unwanted contribution to the conductivity smears out the changes we are looking for. The main detrimental effect in high mobility 2DES is the parallel conduction. Special attention has to be put in the design of the MBE-wafers in order to reduce this effect and still have good electron mobilities.

The density of the mobile carriers cannot be set precisely enough during growth to have the spin phase transition exactly at $\nu = \frac{2}{3}$. This means that it is convenient to change the electron density of the 2DES by means of a metallic gate. A top-gate is usually preferable since it is technologically easy to fabricate and it does not require a high voltage to be applied due to the close proximity with the 2DES. We used a structure in which the 2DES is located 400 nm below the surface. On the top of the Hall bar a 8.5 nm thick AuPd layer is deposited to be used as the top-gate. Unfortunately, although our gate has an extremely small thickness, our attempts to detect a clear signal from this structure failed because the metal electrode shorts the electric field of the wave, the main mechanism of interaction between the SAW and the 2DES. We also tested devices with a back-gate. For this purpose we designed two different types of structure. In both of them the 2DES resides 120 nm below the surface but the gate is obtained in two different ways. In the first type of structure a layer of p-doped GaAs is grown about 1 μm below the quantum well. In order to have the 2DES electrically separated from the gate it is necessary to obtain ohmic contacts to the QW and to the p-doped GaAs which are perfectly n-type and p-type respectively in order to avoid a short circuit. This avoids prestructuring the gate layer prior to overgrowing it [124, 125, 126]. We successfully managed to fulfill these requirements and some devices were prepared which were tunable over a wide range of electron density and still show mobilities exceeding $600000 \text{ cm}^2/\text{Vs}$. Alternatively the devices are glued onto the sample holder with conducting silver paste, as above mentioned; the holder itself can then be used as back-gate. This solution is relatively simple but has the disadvantage that the metallic gate is far from the 2DES and high voltage is required in order to slightly modify the carrier density. This means that the sample has to be designed to have an intrinsic carrier density already close to the optimal value. This has been achieved by optimizing the doping concentration and the spacer extension (see App. A for the sample structure). All the measurements that will be presented in Chapter 5 are obtained with the last

type of sample.

In addition to all of these efforts a setup with a high signal to noise ratio is required in order to detect small changes in the attenuation and velocity of the SAWs. Our apparatus is described in the next section.

4.3.2 Apparatus

Sample holder

The metallic transducers behave essentially as antennas. This means that at high frequencies they will generate unwanted electromagnetic radiation that can interfere with the signal in which we are interested. It turned out that these sources of radiation were not sufficiently screened using the sample holders normally used for quasi-DC measurements. For this reason a special sample holder was designed. Fig. 4.6 shows one of these devices. It consists of a custom-designed PC board; the dielectric material is FR4, while the metallization material is copper, partially covered with tin. The ohmic contacts and the transducers are connected to the metallized parts of the board by gold wires $25\ \mu\text{m}$ in diameter. Gold pins are used for

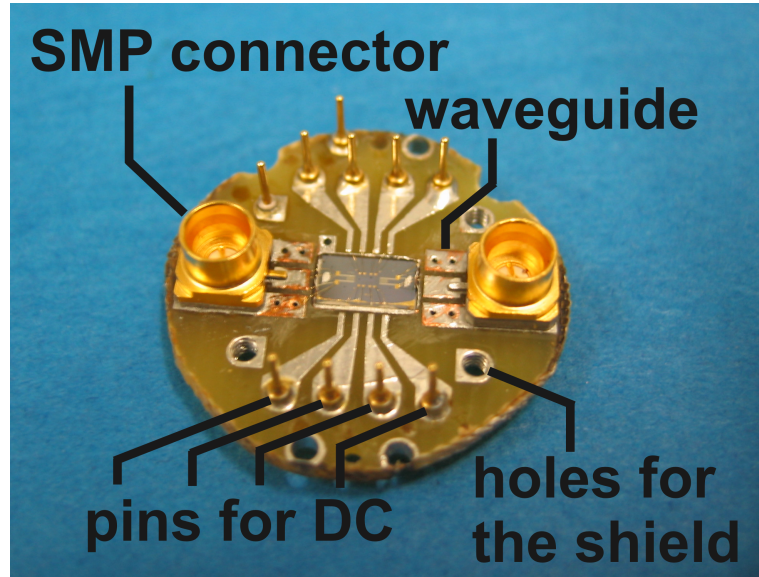


FIGURE 4.6: An image of our PC board with the device inserted. The bonding wires are present. After the device is glued with silver paste and the bonding wiring is ready, a metallic cover is put on the top using three screws. The cover voltage is put to ground to shield the device from electromagnetic radiation. See text for details.

connecting the ohmic contacts to the DC wiring of the cryostat. The design of the high frequency lines must be more accurate in order to avoid power dissipation and electromagnetic radiation. To save space we use SMP Straight Plug connectors for the transmission of the high-frequency signal. The connection between the bonding wires and the SMP connectors is realized with grounded-coplanar-waveguide designed for 50Ω impedance³. Also the bonding wires connecting the coplanar waveguides to the transducers behave like antennas when subjected to a HF signal. To reduce this contribution we opted for having wires as short as possible. This is achieved by creating a slot in the PC board that contains the device, reducing in this way the vertical extension of the wires. This slot is metallized and is used as a back-gate (see Sec. 4.3.1).

Finally, as a shield against external perturbation, a brass cup connected to ground covers the device. The main idea behind this design is to confine the sample into a metal cavity with dimensions much smaller than the wavelength of the ambient RF signals.

Cryogenic insert

Our first choice had been a Heliox insert from Oxford Instruments. It allows measurements in vacuum, where the mass loading on the surface is negligible. It has a nominal base temperature of about 270 mK and enough space for the sample holder and for a mechanism to tilt the sample *in situ*. High frequency low loss coaxial cables were required to carry the RF signal to the input IDT and detect the transmitted SAW from the output IDT. However heat flow through the RF lines thermally loaded the sample. To counteract this, great care had been taken to dissipate the heat to prevent thermal conduction to the device. Sapphire striplines were mounted onto the ^4He and ^3He pot respectively. The lines were defined by thermal evaporation of Au, and their dimension was calculated in order to achieve 50Ω impedance. Cables were thermally anchored in this manner on the ^4He and ^3He pot. Furthermore, the outer conductors of the coaxial cables were thermally anchored to the conical seal of the Heliox. Connections between the coax and the strip line were made using silver solder paste. The RF lines consisted of three sections: first, semi-rigid coaxial cables were mounted between the top of the insert and the ^4He pot. These were

³The layout recommendation from the company producing the SMP connector (Rosenberger Hochfrequenztechnik GmbH) was used.

terminated at the top end with a $50\ \Omega$ SMA connector. This type of cable (Precision Tube, model AS50085) has a stainless steel outer conductor of thickness 0.25 mm, a silver plated copper-clad steel inner core of 0.5 mm diameter and a PTFE dielectric. Thinner and more flexible coaxial cables were inserted between the 1 K pot and the ^3He pot. These have an inner conductor diameter of 0.11 mm, an outer conductor of 0.51 mm and a PTFE dielectric. The attenuation is higher than for the previous cables and they were inserted to increase the thermal isolation of the ^3He pot. Finally, the lower section connecting the ^3He and the sample consisted of the semi-rigid coax plus twisted copper wires at the very end. With these modifications we managed to reduce the heat load of the sample. However, due to poor reliability of the insert (leaks) and technical problems with the rotating mechanism, we moved to a different system.

The measurements shown in Chapter 5 are performed in an Oxford Instruments cryostat equipped with a superconducting magnet with a maximum magnetic field value of 12 T. The sample holder resides in a ^3He bath inside a ^3He pumped insert whose lowest temperature is nominally 350 mK (homemade ^3He system).

The liquid above the device dissipates part of the acoustic power. There are two main mechanisms of dissipation: due to generation of compressional waves into the liquid, and due to friction with the liquid at the surface. The attenuation due to these two effects can be estimated to be [127] 3.37 db/cm and 3.7×10^{-3} db/cm respectively, low enough to be disregarded.

The insert was equipped with a small Philips RuO_2 thermal resistor placed in close proximity to the device, a bigger Ge resistor still close to the sample holder, a heater to remove liquid ^3He for allowing faster device replacement and a LED to illuminate the device. 21 double-insulation constantan wires were inserted to perform quasi-DC measurements, to apply the voltage to the gate and to control the electronic devices just mentioned. Two low-loss coaxial cables were required to carry the HF voltage to the transducers and detect the SAW signal. The coax that we inserted were the same semi-rigid Precision Tube cables that we have described above. They terminated at the very top end of the insert with $50\ \Omega$ SMA connectors, and at the bottom with SMP Straight Jack connectors compatible with the SMP connectors on the sample holder. In this way the sample holder can be easily (dis)connected to the HF line just by plugging it. Special care has to be taken in order to avoid excessive heating from the HF lines to the 2DES. The ^3He bath in which the coaxial cables terminate provides already a good dissipation. Moreover, several heat sinks

are placed along the full length of the cables and also along the insert itself to increase heat dissipation.

With the modifications mentioned above we were able to work at a temperature of about 400-500 mK for about 30 hours. After this time, the liquid ^3He is almost completely evaporated, the pumping on its surface has to be stopped and the ^3He gas has to be condensed again at about 1.3 K. Waiting a longer time caused the device to warm up dramatically to more than 30 K, with the consequence that the 2DES could have different characteristics in a second cooldown. To prevent this we did not perform continuous measurements for more than 20 hours.

A Keithley Source Measurement Unit 236 provided the DC voltage to the gate. This instrument allows the determination of the resistance between the 2DES and the metallic back-gate. In all the measurements shown in this thesis, the value of this resistance was higher than $5\text{ G}\Omega$ for an area of 0.18 mm^2 .

With the exception of the power supply of the magnet, which was controlled via a Serial connection, all the instruments were controlled via a GPIB interface by self-written programs in Labview.

Quasi-DC transport measurements

Theoretical predictions of the velocity shift and attenuation of surface acoustic waves based on Eq. 4.5 rely on the measurement of the low-frequency conductivity. Transport measurements were made using the Hall bar geometry shown in Fig. 4.5. The transversal and longitudinal voltages were measured simultaneously with two Signal Recovery 5210 lock-in amplifiers, whose outputs were fed into Keithley 199 digital multimeters and then read out by a GPIB interface. Measurements were performed in a 4-point configuration, with separated contacts being used for source, drain, voltage probes. The reference signal was given by the internal source of one of the lock-in amplifiers. The applied current was generated by the internal oscillator of the same lock-in amplifier followed by an in-series $10\text{ M}\Omega$ resistor. If not otherwise specified, reference signals of 3.4 Hz were used, with excitations currents in the range 1-200 nA.

SAW transmission

SAW attenuation and velocity measurements are usually made with pulsed signals in order to use the different arrival times to distinguish between the unwanted (fast)

electromagnetic cross-talk and the (slower) SAW signal. However the construction of a linear, low-noise detection system is not an easy task. Our approach is to use an Agilent Technologies network analyzer E5071B equipped with the option of time-domain measurements. With this instrument we can send frequency-swept continuous waves to the input transducer and measure simultaneously both phase and amplitude of the signal induced from the output transducer. This allows us the inverse Fourier transformation of the data to the time domain and still use arrival time discrimination to select the desired SAW signal through bandpass window gating. Once the correct gating is chosen, it is possible to return to the frequency domain where, thanks to above procedure, the signal caused by frequencies not in resonance with our IDTs is strongly suppressed, and this results in an enhanced signal to noise ratio.

Before being sent to the network analyzer the signal coming from the output transducer is amplified. We use one of three different models of amplifier from Miteq depending on the frequency range in which we are working: AU-1114 (10-500 MHz), AM-1533 (1-1000 MHz) and AFS5-00100600-1 (0.1-6 GHz).

Furthermore the signal is averaged over 100 spectra by the network analyzer to increase the signal to noise.

Flexible low-loss coaxial cables LMR-240 from Times Microwave Systems are used from the network analyzer to the cryostat and from the amplifier to the network analyzer.

It is important to stress that the SAW measurements are performed simultaneously with the quasi-DC transport measurements described in the previous section. This allows a direct comparison between the results obtained with the two techniques. Fig. 4.7 shows an example of such a kind of measurement. The experimental attenuation and velocity shift for a SAW of frequency 350 MHz are plotted in the upper graphs. At low magnetic field ($B \lesssim 1$ T) both the attenuation and the velocity shift show characteristic oscillations which coincide in position with the Shubnikov-de Haas oscillations. At higher field, when the quantum Hall effect becomes more pronounced, the oscillations in the attenuation split into two peaks surrounding the region of integer filling factor. The prediction of Eq. 4.5 are shown in the lower graphs of Fig. 4.7. The curves qualitatively reproduce the experimental results although there are some quantitative differences. The experimental oscillations seem to be superimposed on a smooth background. Moreover, the experimental attenuation maxima do not reach the theoretical value of $k k_{eff}^2/2$ (see Eq. 4.5). One

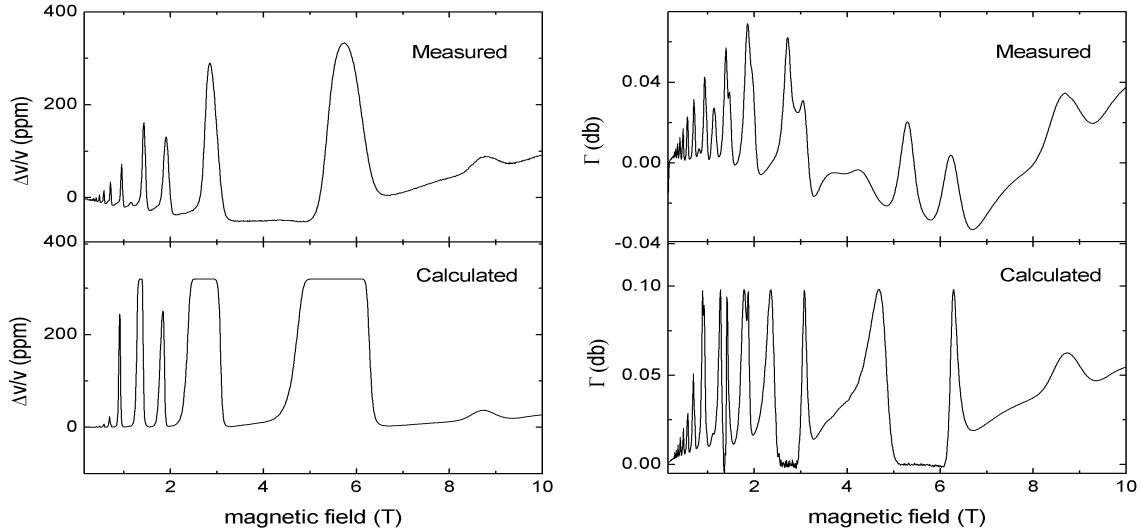


FIGURE 4.7: Velocity shift (left panels) and attenuation (right panels) of a surface acoustic wave as a function of the magnetic field. The upper graphs are the experimental results, while the lower ones are the calculations based on Eq. 4.5. The acoustic power at the top of the inset was -20 dbm. Data obtained from wafer 8813 with a SAW frequency of 350 MHz.

possible reason is the acoustic load caused by the AlGaAs barrier in our sample and (much more important) by the doping layer. The latter source of attenuation is included in Eq. 4.5 only through the contribution that it adds to σ_{xx} , but the SAW is more sensitive to any extra conductive channel than quasi-DC transport. Another difference between the experimental and the theoretical curves is that the width of the peaks in the velocity shift and the distances between the splitted peaks in the attenuation are smaller than the predicted ones, whose positions coincide with the widths of the quantum Hall effect as obtained from the transport data. We do not know yet where this difference comes from. One possible explanation is due to the fact that standard quasi-DC transport probes the conductivity of the edge states, while in the case of SAW propagation we probe the *bulk* conductivity of the 2DES. The asymmetry of the peaks in Γ is probably caused by small inhomogeneities of the sample [108]. In short, our setup allows us the detection of all the features present in the standard quasi-DC transport measurement with SAWs. Fig. 4.8 shows a comparison between the longitudinal resistivity ρ_{xx} at low field with the SAW transmitted signal. Oscillations are clearly resolved in the transmission that fully reproduce the well-known Shubnikov-de Haas oscillations in the resistivity. This ensures the sensitivity of our setup even to small changes in the conductivity.

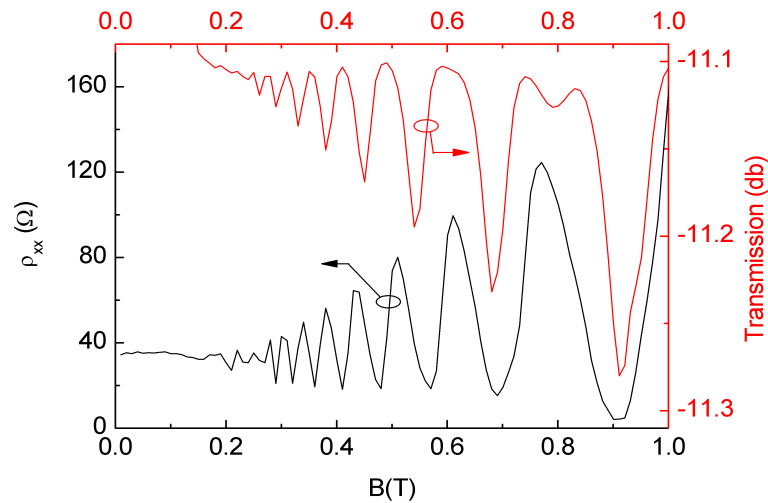


FIGURE 4.8: Longitudinal resistivity (black curve) and acoustic transmission (red curve) along the SAW delay line at low magnetic field. Data obtained from wafer 8813 with a SAW frequency of 350 MHz.

SAW drag

For this kind of measurements we use the same type of device as described in Sec. 4.3.1 and employ the experimental configuration called 'open geometry' [128]. We generate SAWs with one of the transducers while the other is kept short circuited. All of the contacts of the Hall bar are left open and the action of the SAW is to generate electric fields in the sample where no macroscopic current is permitted. An amplitude modulated (AM) signal is generated by an HP8657A RF-generator and sent to the input IDT while the other IDT is connected to ground. The reference modulation signal for the RF-generator is a sinusoidal wave with a frequency of 70 Hz and the ratio on/off of the AM output signal is set to 99%. The voltage generated by the SAW at the contacts of the Hall bar is detected with standard lock-in technique with the reference frequency given by the modulation signal.

Studying the acoustoelectric effects is not an easy task. It is extremely difficult to separate the contribution of the 2DES from that generated by impurities, by non-perfect contacts and so on. In the following we show the capabilities of our setup using measurements performed on the same wafer of Fig. 4.7.

First we check that we can detect acousto-drag voltages: we fix the value of the magnetic field and we sweep the input frequency in a range around the resonance frequency of the transducer. Since the IDTs produce SAWs only at a precise frequency, the voltage due to the acoustic wave should appear only when the exciting

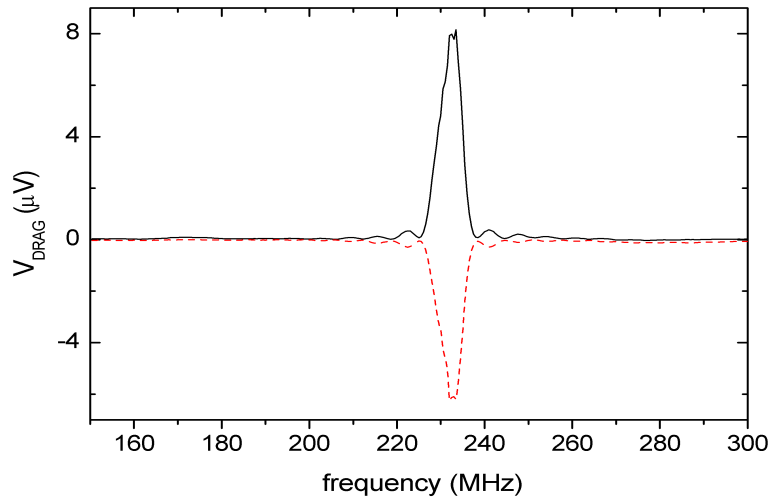


FIGURE 4.9: Drag voltage measured at a magnetic field of 10 T and an acoustic power of -10 dbm. The solid and dashed lines are recorded under the same experimental conditions but using two different transducers. Data obtained from wafer 8813 with a SAW frequency of 233 MHz.

frequency is equal to the resonance frequency. The same resonant structure should be detected also when the input IDT is interchanged, but from symmetry arguments its sign should be reversed. A typical result for the longitudinal (drag) voltage measured at 10 T and input power of -10 dbm is reported in Fig.4.9. A clear resonant signal is detected around the resonance frequency of 233 MHz. Using the opposite IDT the features at the resonance frequency are inverted, as expected. The quantitative differences are due to the fact that the two transducers are not perfectly identical. We check that the experimental results in the acoustoelectric measurements are present *only* when the signal applied to the transducer is at resonance. To get rid of the smooth background signal, which is typically one order of magnitude smaller than the SAW induced signal, we subtract from the trace taken at the resonance frequency the one taken out of resonance.

Fig. 4.10 shows the quasi-DC measurement of the longitudinal and Hall resistivities taken at a temperature of 1.3 K. The features related to the integer quantum Hall effect are well resolved. In Fig. 4.11, the upper panel shows the drag voltage measured on the same sample for an input power of -10 dbm. At low field ($B \lesssim 1$ T) the curve presents oscillations that are in phase with the Shubnikov-de Haas oscillations. At higher fields the drag voltage is zero at integer filling factors: the SAW-induced electron flow is dissipationless. It is interesting to note that the overall drag voltage

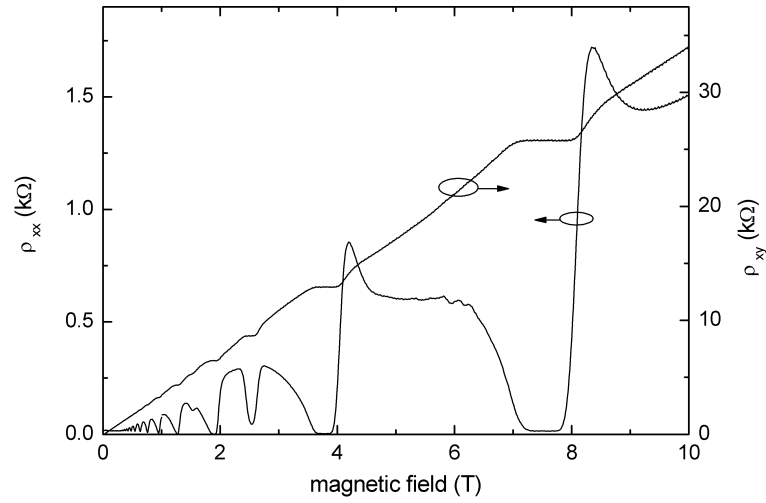


FIGURE 4.10: Longitudinal and Hall resistivities measured with quasi-DC techniques. Data obtained at a temperature of 1.3 K from wafer 8813

resembles quite well ρ_{xx} even though we are not applying any quasi-DC current. This can be understood since now it is the SAW that transfers a non-zero average momentum in the direction of its propagation to the electrons. The above results show that our setup allows the detection of drag voltages. Fig. 4.11 lower panel shows the drag signal calculated according to Eq. 4.10 using the data of Fig. 4.10. Qualitatively the theoretical curve reproduces all the features present in the experimental one. Quantitatively this is not the case. No quantitative comparisons have been reported in previous works. Nevertheless the theory of Falko *et al.* is the one that reproduces the experimental features best.

The above results show that our setup allows the detection of the signal due to the acousto-drag and that Eq. 4.10 can be used to qualitatively interpret our experimental findings.

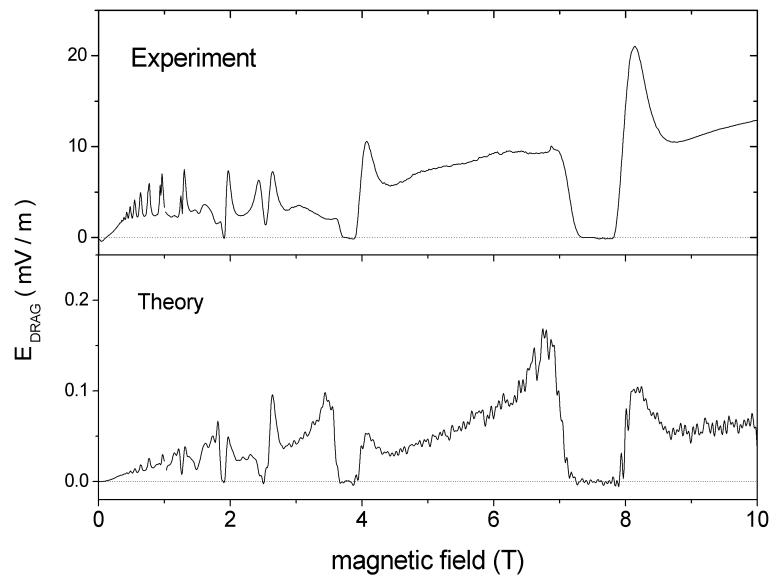


FIGURE 4.11: Upper panel: drag signal from wafer 8813. Data obtained at a temperature of 1.3 K and an acoustic power of -10 dbm with a SAW of frequency 233 MHz. Lower panel: drag signal calculated from the quasi-DC data shown in Fig. 4.10 using Eq. 4.10.

5 Results and discussion

In this chapter we present our experimental results concerning the spin phase transition at filling factor $\frac{2}{3}$. This transition has been studied both in the low current regime, where the quantum Hall ferromagnetism is present, and in the high current regime, where the interaction between electron and nuclear spins takes place.

We study the transition mainly by detecting the longitudinal transport properties of the 2DES close to $\nu = \frac{2}{3}$ and the SAW damping simultaneously.

In the first part we show the results obtained with quasi-DC techniques at a probing frequency of 3.4 Hz. Then we study the conductivity of the 2DES at high frequencies using SAW.

Finally, in the last part of the chapter, we will discuss our experimental findings.

5.1 About the devices

In order to study the phase transition at $\nu = \frac{2}{3}$ with SAWs it is crucial to have a 2DES of good quality.

The most important requirement is a weak parallel conduction because it shorts the electric field (see Chap. 4). Whenever the parallel conduction is absent in the quasi-DC transport data, SAW measurements are possible and the results reliable. In order to change the electron density a metallic top-gate should be (if possible) avoided. In fact a conducting layer on the surface contributes to the screening of the electrical potential of the wave, reducing the signal to noise ratio. If using a back-gate great care has to be taken in order to change the applied voltage slowly, otherwise increased leakage currents can be detected.

We measured several devices from two different wafers. They all show qualitatively the same results. In the rest of this chapter we concentrate on the data obtained from the wafer 81644 (see Appendix for the sample structure). We will focus in particular on two devices obtained from that wafer with back-gates on the bottom surface. The preparation is similar for both (see Sec.4.3.1) except for the design of the IDTs. In one of the samples (sample A) the resonance frequency of the

transducers is about 233 MHz while in the other (sample B) it is 115 MHz. Unless otherwise mentioned, during the measurements the gate voltage was kept fixed in order to have the degeneracy between the two ground states (spin polarized-spin unpolarized) at filling factor $\frac{2}{3}$. The transition between one spin configuration to the other is achieved by sweeping the magnetic field around the fractional filling factor.

5.2 Quasi-DC transport

In this section we describe the magnetotransport measurements of our devices at $\frac{2}{3}$ filling. The main results of previous works at the spin transition are reproduced. As in earlier works the details of the hysteresis varied from sample to sample and experimental runs. The possible explanations for these differences are discussed and the experimental procedures to get consistent results are described.

Fig. 5.1, main graph, shows the longitudinal resistivity for sample B plotted as a function of the magnetic field for the two sweep directions of the magnetic field.

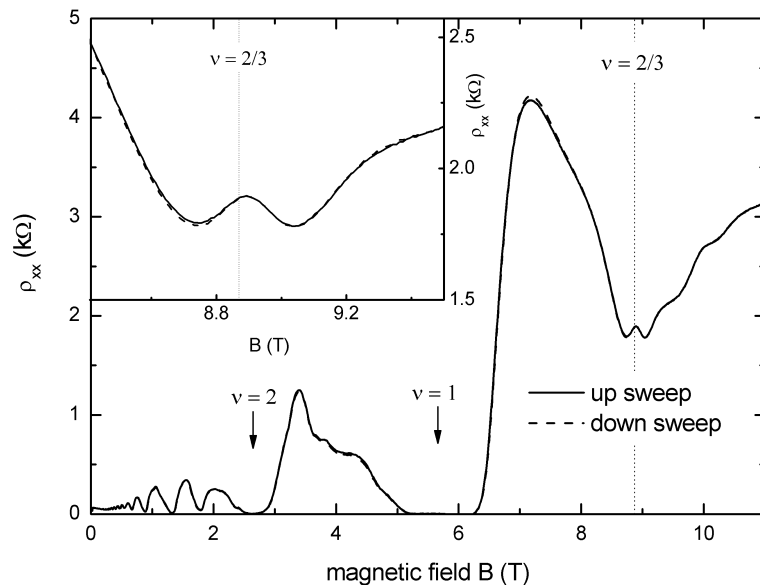


FIGURE 5.1: Main graph: longitudinal resistivity for sample B as a function of the magnetic field for the two sweep directions: up (solid line) and down (dashed line). The data are taken in the low current regime: the excitation current is 10 nA and the magnetic field sweep rate is 0.4 T/min. The regions of dissipationless transport at filling factor 1 and 2 are indicated. The vertical dotted line indicates the position of filling factor $\frac{2}{3}$. Inset: zoom on the magnetic field region close to $\nu = \frac{2}{3}$.

These data are taken with an excitation current of 10 nA and a field sweep rate of 0.4 T/min. One recognizes the regions of dissipationless transport corresponding to the integer quantum Hall regime (filling factor 1 and 2 are indicated in the figure). At low magnetic field, Shubnikov-de Haas oscillations are also visible. More important is the high field region, where the vertical dotted line at about 8.9 T indicates the position of the filling factor $\frac{2}{3}$. This region is plotted in an enlarged view in the inset. At $\nu = \frac{2}{3}$ a minimum in the resistivity is expected. Instead, the curves show a small peak at this filling factor. This resistivity maximum indicates that the phase transition is taking place [54].

Fig. 5.2 represents the same kind of measurement as before, but now the current has been increased to 200 nA and the magnetic field sweep rate, in the region close to $\nu = \frac{2}{3}$, has been reduced to 5 mT/min. Instead of the small peak of Fig. 5.1 a huge increase of the resistivity (HLR) is now present at the phase transition.

From now on, we will refer to these different behaviors as the *low current* and the *high current* regime.

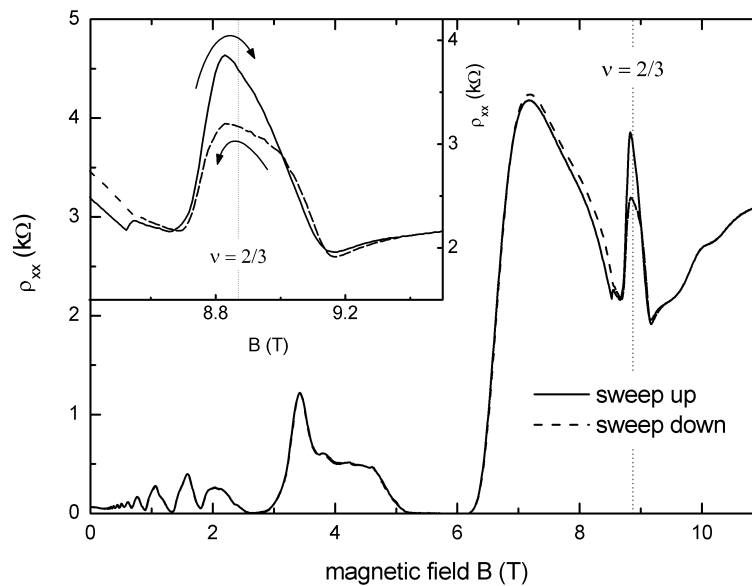


FIGURE 5.2: Main graph: longitudinal resistivity for sample B as a function of the magnetic field for the two sweep directions: up (solid line) and down (dashed line). The data are taken in the high current regime: the excitation current is 200 nA and the magnetic field sweep rate is 5 mT/min close to the transition. The vertical dotted line represents the position of $\nu = \frac{2}{3}$. Inset: zoom on the magnetic field region close to $\nu = \frac{2}{3}$.

5.2.1 Lack of reproducibility and exchange effects

Fig. 5.3 summarizes the longitudinal resistivity at the phase transition for the two different regimes. The solid lines are taken in the low current regime, the dashed line in the high current one; the black curves correspond to a magnetic field sweep up, while the red curves are for fields changing downwards¹.

Looking at Fig. 5.3, there are two effects that distinguish the high current from the low current regimes.

The first one is the increase in resistivity already mentioned. The second one is the dramatic hysteretic behavior present in the high current regime upon changing direction of the magnetic field sweep. Let us focus on this second point.

Fig. 5.4 shows the longitudinal resistivity close to filling factor $\frac{2}{3}$ for sample A, taken in the low current and in the high current regime respectively. For this sample the hysteresis is present not only in the high current regime but also in the low current one. The same phenomenon, although not so dramatic, is present during a second

¹In the rest of the chapter, the same notation holds if not otherwise indicated.

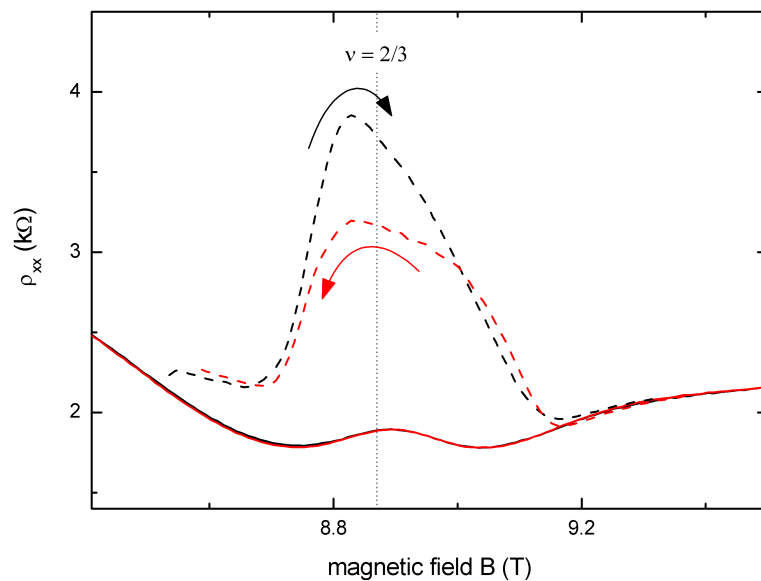


FIGURE 5.3: Longitudinal resistivity for sample B in the high and low current regime as a function of the magnetic field for the two sweep directions in the region close to filling factor $\frac{2}{3}$. The solid lines correspond to the low current regime ($I = 10$ nA, B-sweep rate of 0.4 T/min), while the dashed lines are for the high current regime ($I = 200$ nA, B-sweep rate of 5mT/min). Black lines refer to upwards B-sweep, while the red lines are for the downwards B sweep.

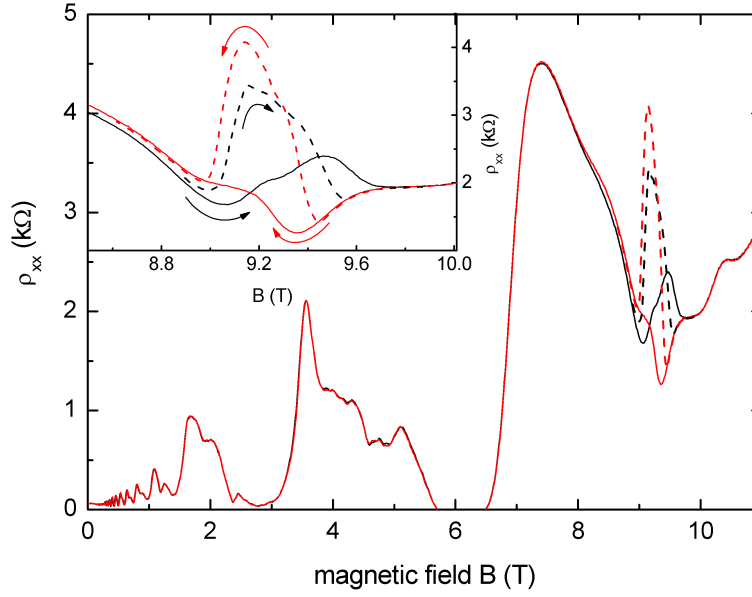


FIGURE 5.4: Longitudinal resistivity for sample A in the high and low current regime as a function of the magnetic field for the two sweep directions. Inset: zoom on the region close to filling factor $\frac{2}{3}$. The notation is the same as in Fig. 5.3

cooldown (from room temperature) of sample B (see Fig. 5.5).

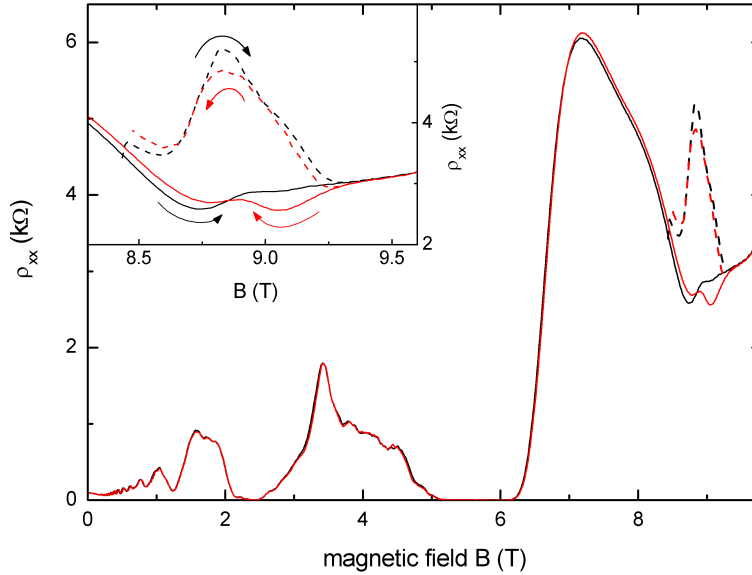


FIGURE 5.5: Longitudinal resistance for a different cooldown of sample B in the high and low current regime as a function of the magnetic field for the two sweep directions. The different lines have the same meaning as in Fig.5.3. Inset: zoom on the region close to filling factor $\frac{2}{3}$

Phase transitions at the crossing of different LLs are often characterized by hysteretic phenomena [54]. Previous studies of the spin transition at $\nu = \frac{2}{3}$ are characterized by hysteresis in the low and high current regime [80, 87, 73]. However, hysteresis in the low current regime has been observed only at temperatures lower than 70 mK, much lower than the one of our experiments. Moreover, while in the high current regime the transport properties changed for different cooldowns also in the previous works, in the low current regime they were quite stable. It is not completely clear why our devices show different behaviors. Stern [84] studied the hysteresis in the low current regime at 70 mK as a function of the gate voltage (i.e. the filling factor) for a 15 nm QW. The hysteresis is present when the voltage is varied at a fast rate (0.6 V/min) while it disappears for a slower voltage rate (6 mV/min). He attributes this effect to the exchange energy of the electrons. To understand this argument let us look at the energy diagram depicted schematically in Fig. 3.4. Approaching the coincidence from the low field region the two occupied level has opposite spin index. Since the Pauli exclusion principle does not prevent electrons with opposite spins from approaching each other, their Coulomb interaction is strongly modified. The transition does not occur at the level coincidence but is slightly shifted. On the other side of the crossing point such a modification is less effective. In other words, the transition does not occur symmetrically with respect to the crossing point. Activation energy measurements of Stern show different energy gaps on the two sides of the transition and the slope with which the coincidence is approached is slightly different for the two magnetic field directions. These data confirm the picture described above. In our measurements the magnetic field is changed relatively fast (0.4 T/min). A stronger exchange interaction with respect to previous studies could be the reason for the detection of the hysteresis at higher temperature.

The lack of reproducibility of the transition in devices obtained from the same wafer and even in the same device in different cooldown cycles suggests that microscopic differences play a role in the observed phenomena. One of these differences could be local random fluctuation of the thickness of the QW. As previously mentioned the polarization of the 2DES depends on the ratio between Zeeman and Coulomb energy. A different width of the quantum well causes corrections to both these energies. The g -factor has to be modified due to corrections arising from the non-parabolicity of the band structure in GaAs [129] and from the confinement induced light-hole heavy-hole splitting in the valence band of GaAs [130]. The Coulomb energy can be

calculated according to

$$E_C = \frac{e^2}{4\pi\epsilon l_B^{eff}} \quad (5.1)$$

where $l_B^{eff} = \sqrt{l_B^2 + \lambda^2}$ is the effective magnetic length and λ is the full-width-half-maximum of the wavefunction, which depends on the QW thickness [131, 132]. Different devices, although originating from the same wafer, could have different QW-width fluctuations. This implies different domain morphology and a different response as a function of the magnetic field.

Also the hyperfine interaction between electron and nuclear spin can strongly influence the electronic transport at $\frac{2}{3}$. Whenever the nuclei are polarized they create a local magnetic field, referred to as the nuclear hyperfine field B_N . As a result the Zeeman energy changes to $g^*\mu_B(B_{ext} + B_N)$. The change in the electron spin resonance (ESR) frequency due to the nuclear hyperfine field is known as the Overhauser shift [133]. The different response of our devices could be due to a different nuclear polarization. This is however quite unlikely to happen. The nuclei can only be polarized thermally or through spin flip-flop processes. The thermal polarization is negligible at the temperature and magnetic field of our experiment ($T \simeq 400$ mK, $B \simeq 10$ T). Spin flip-flop scattering should not occur in the low current regime because the current that we apply is not strong enough to polarize the nuclei (see Sec. 5.4).

The different behavior of our devices could be due to a different disorder potential which can act through pinning centers for the domain nucleation and the domain wall topology². One should mention that the wafer 81644 has been grown with a different MBE machine with respect to the ones used by previous authors [80, 73, 84] and the impurity potential distribution could be different.

Let us focus on the high current regime. In this regime the interaction between electron and nuclear spin becomes stronger. The current can actually induce a dynamical nuclear polarization that can cause the HLR. Previous results [80] report that the local maximum of the HLR occurs at the magnetic field value at which the phase transition is taking place. As mentioned, in the low current regime this value can vary depending on the B-sweep direction: it is quite different in sample A and more similar in sample B. It is noteworthy that the HLR peaks for the two magnetic field directions are more separated in sample A (Fig. 5.4) than in sample B

²Regarding the role of the pinning potential in ferromagnetic materials see [134, 135].

(Fig. 5.3 and 5.5) and that there is also a difference between the relative amplitude of the HLR of the two samples for the different B-sweep direction. The origin of this irreproducibility in detail is not completely understood.

In the rest of the thesis in each section we will present only measurements performed on the same device during the same cooldown. We want to stress that with this precaution all of the results are perfectly reproducible. Moreover, the experimental findings and the conclusions are consistent among different devices and different cooldowns.

5.3 Time dependence

Time dependent measurements in the large current regime show the typical variation of the resistance over minutes and hours. In addition we observe a "switching" between two resistance values in some of our samples that was not reported before. In general, our data are consistent with the formation of domains. The details of this formation are not reproducible and depend in particular on the sample being in the small or large current regime.

These measurements are performed on sample B. Fig. 5.6 shows the longitudinal resistivity close to filling factor $\frac{2}{3}$ in the low (solid line) and high (dashed line) current regime for a magnetic field sweep up. As shown in the previous section an increase in the resistance develops in the high current regime.

The time-dependent data are measured in a 'reset-and-probe' fashion. This type of measurement is normally performed by quickly changing the filling factor by means of a top-gate [89, 88, 84, 132]. In our devices we did not employ a top-gate and the voltage to the back-gate had to be varied slowly in order to avoid leakages. For this reason we decided to vary the filling factor by changing the magnetic field. The complete measurement procedure is described in the following. We move with the magnetic field to one of the values indicated in Fig. 5.6 with a sweep rate of 0.4 T/min. We then stop the field and record the value of the resistivity as a function of time ('probe'). After that we move back to a magnetic field value B_{reset} and monitor the resistivity as a function of time. The value decreases until it reaches a stable minimum ('reset'). This procedure is repeated for the five magnetic field values indicated in Fig. 5.6. Hashimoto *et al.* [89] find an enhanced relaxation rate of the resistivity when $\nu_{\text{reset}} \simeq 1$ due to the presence of skyrmions (see Sec. 3.1). However, as stated by Höppel ([132] pag.111), 'almost any reset filling factor sufficiently far

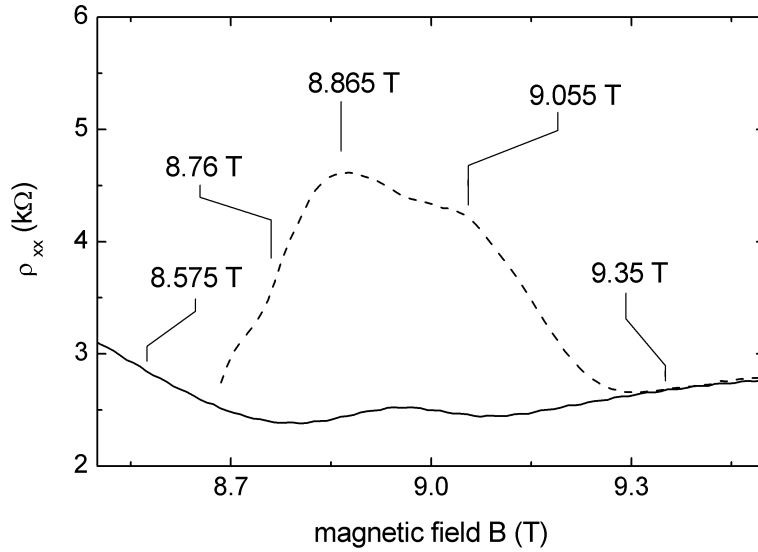


FIGURE 5.6: Longitudinal resistivity of sample B measured in the low current regime (solid line) and in the high current regime (dashed line) for a different cooldown cycle with respect to Fig. 5.3. The magnetic field values at which the 'probe' measurements are performed (see text for details) are indicated.

away from $2/3$ and any reset time well above a few seconds can be used to achieve an always equal nuclear magnetic field'.

Since the magnetic field cannot be varied over a large range instantaneously we choose to perform the reset measurement at $B_{\text{reset}} = 8.5$ T. This value is far enough from the transition to exclude influences from the physics occurring at $\nu = \frac{2}{3}$ but can be reached in about one minute. To ensure the same initial conditions we wait at B_{reset} for about half an hour before the next 'probe' measurement begins. Fig. 5.7 summarizes the results. The resistivity shows a fast and huge increase in the first ten minutes (not shown) followed by a smooth (almost) monotonic change without saturation even after more than one and a half hours. This general behavior has already been reported by previous authors [80, 136]. Our data present however some new features. The first one is that the smooth change in resistivity seems to depend on the magnetic field value at which the measurement is performed. For filling factors higher than $\frac{2}{3}$ (i.e. lower magnetic fields) the resistivity increases as a function of time. For lower filling factors (i.e. higher magnetic field) the resistivity decreases with time. To our knowledge, at $\nu = \frac{2}{3}$, previous works report only an increase. A behavior similar to ours is reported by Eom *et al.* [68] for $\nu = \frac{2}{5}$. The value of the resistance as a function of time was well fitted by a logarithmic

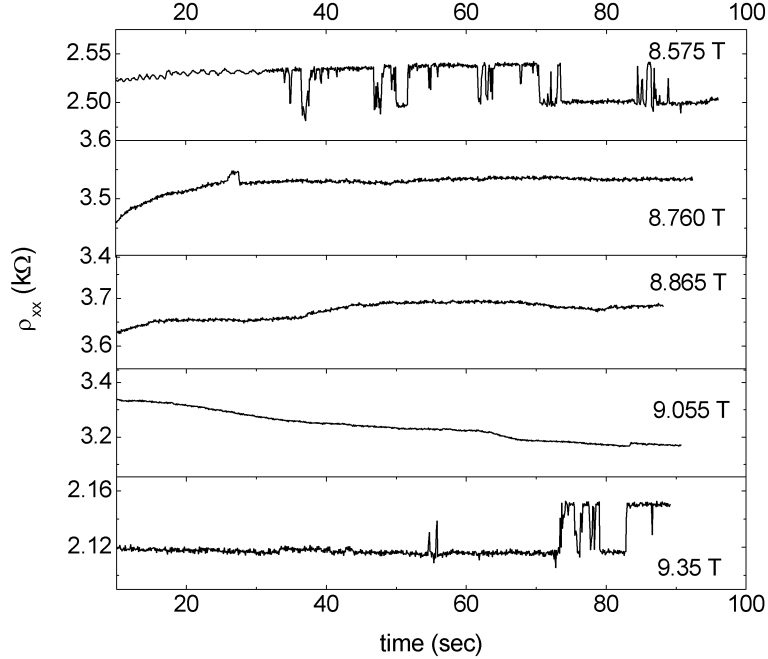


FIGURE 5.7: Longitudinal resistivity as a function of time for the five magnetic field values indicated in Fig. 5.6. The value of the magnetic field at which the measurement has been performed is indicated in each panel. Data begin at a time when the first fast increase in the resistivity value is already completed.

dependence. They argued that this is due to different kinds of dynamics in which the domains are involved. They interpret their result as aging effect due to domain growth (below $\nu = \frac{2}{5}$) and shrinking (above $\nu = \frac{2}{5}$) [137]. This picture seems to fit qualitatively with our data. There are however some important differences. Our data did not present any logarithmic dependence as a function of time. Actually, no simple dependence has been found for our data. Eom *et al.* report about a non-linear voltage-current characteristic at filling factor $\frac{2}{5}$ but did not show the data. It is not known if their results have been obtained in the high current regime, where the interaction with the nuclei could be important³.

We note here that a long relaxation time due to growing and shrinking of domains is indeed expected in a classic Ising model. However, in our system it is difficult to predict the effects due to the DNP and the picture of domain growing and shrinking can be more complicated. Another interesting aspect concerns the resistivity traces recorded at 8.575 T and 9.35 T. These magnetic field values are at the border of the

³They consider the nuclear effects not to be important for their findings.

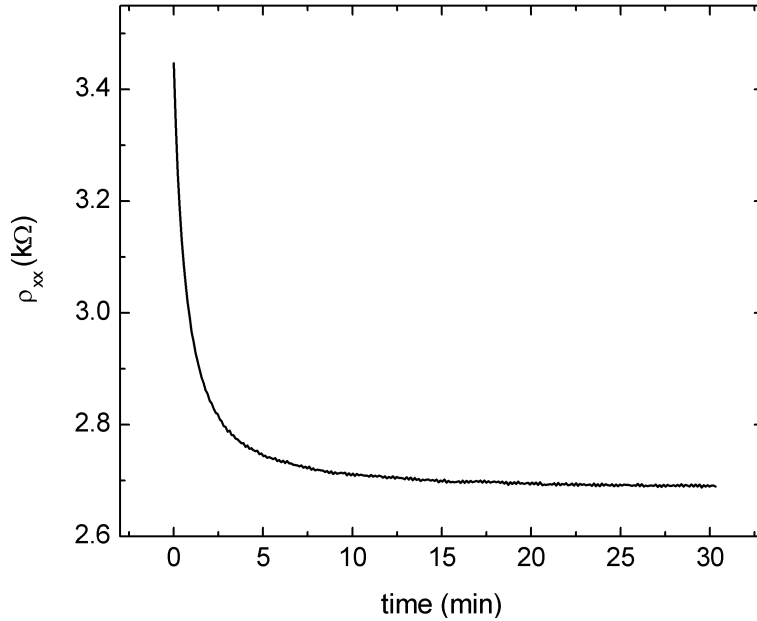


FIGURE 5.8: Relaxation curve at B_{reset} after the 'probe' measurement at 8.865 T (see text for details). The value of the resistance drops rapidly in the first 10 minutes; after about 30 minutes it reaches to a steady value.

region in which the HLR develops. The majority of the sample is either unpolarized (8.575 T) or fully polarized (9.35 T): most likely only a few domains are present. In similar conditions Stern [136] observes increases of the resistivity that look like jumps after tens of minutes. In our devices the resistivity shows also jumps in its value but they are much more numerous compared to the data of Stern. There are also other differences: the jumps in the value of the resistance that we observe are faster compared to Stern's ones. Moreover the value of the resistivity not only increases but also decreases. The resistivity oscillates between two different values in a way similar to telegraph noise. The latter is usually observed when a system jumps between two different states. One possible explanation is that the system is characterized by two different ground states. These data support the picture of domain formation at the phase transition.

After each 'probe' measurement the magnetic field is changed to 8.5 T in order for the system to relax. As an example Fig. 5.8 plots the relaxation curve after the measurement at 8.865 T. The value of the resistivity decreases to a stable value after about 10 min.

5.4 Transport in small Hall bars

Magnetotransport measurements are performed in Hall bars which are only 10, 5 and 2 μm wide. No size dependence of the resistance behavior at $\nu = \frac{2}{3}$ was found down to this length scale.

Fig. 5.9 shows the longitudinal resistivity for a Hall bar 10 μm (upper panels) and 5 μm (lower panels) wide, with contact arms separated by a distance of 30 μm in both cases.

We plot measurements taken in the low current regime (1.5 nA and 1 nA, solid curves) and in the high current one (10 nA and 5 nA, dashed curves) respectively. The two devices behave similar to the ones described in the previous sections: in the low current regime a resistivity maximum signals the spin phase transition; this maximum develops into the HLR peak in the high current regime. Fig. 5.10 shows the longitudinal resistivity measured in the Hall bar 5 μm wide, using contact arms separated by a distance of 30 μm (black curves) and 10 μm (red curves).

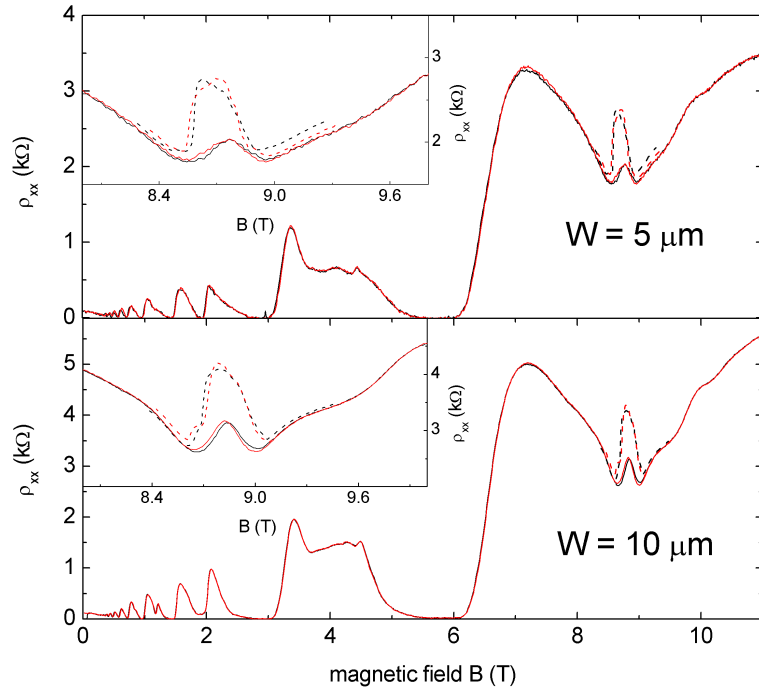


FIGURE 5.9: Longitudinal resistivity for Hall bars 10 μm (lower graph) and 5 μm (upper graph) wide, both in the low (1.5 nA and 1 nA, solid curves) and high (10 nA and 5 nA, dashed curves) current regime. The insets show a zoom on the region close to filling factor $\frac{2}{3}$.

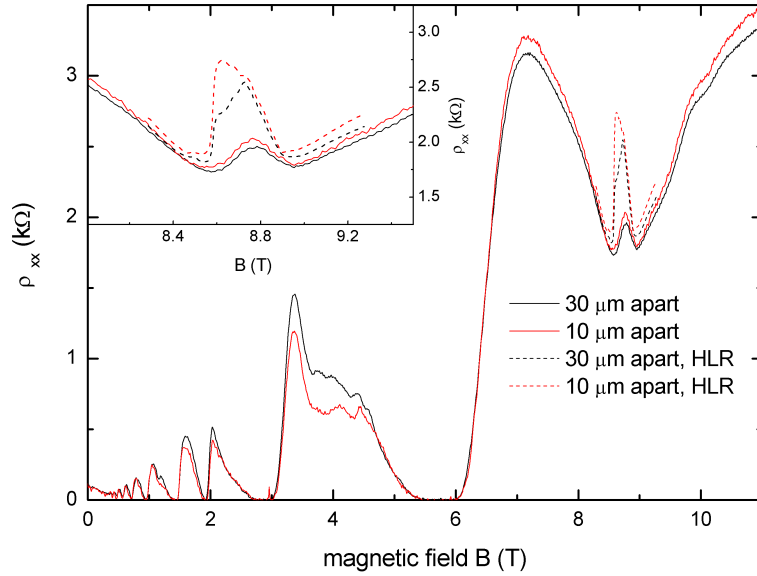


FIGURE 5.10: Longitudinal resistivity for a $5 \mu\text{m}$ wide Hall bar measured using different contact arms. Black curves: contact arms separated by $30 \mu\text{m}$. Red curves: contact arms separated by $10 \mu\text{m}$. Solid lines are measured in the low current regime, dashed lines in the high current regime. The magnetic field is swept upwards during these measurements.

No real difference is present between the curves measured with the two different configurations. These results show that the phenomena responsible for the spin phase transition are taking place on a shorter length scale. To compare the different Hall bar devices we plot the current-voltage characteristic in Fig. 5.11. The applied current is normalized to the width of the Hall bar W . The vertical arrows in the figure point the value of the critical current density where the HLR develops. Although the three devices have different dimensions this value is nearly the same for all three of them and is equal to about $0.33 \text{ nA}/\mu\text{m}$. This means that the mechanism behind the phase transition at $\nu = \frac{2}{3}$ is qualitatively (and quantitatively) the same in Hall bars $200 \mu\text{m}$ and $5 \mu\text{m}$ wide.

The deviation from linearity in the high current regime changes with size. However, the distance between the voltage probes is not the same for the different Hall bars and a comparison is not possible. Further studies need to address this aspect.

We also studied a device in which the width of the Hall bar was only $2 \mu\text{m}$. Unfortunately in this device the gate presented higher leakage current with respect to the previous ones. It was therefore not possible to tune the electron density in order to have the spin transition exactly at filling factor $\frac{2}{3}$. Fig. 5.12 shows the

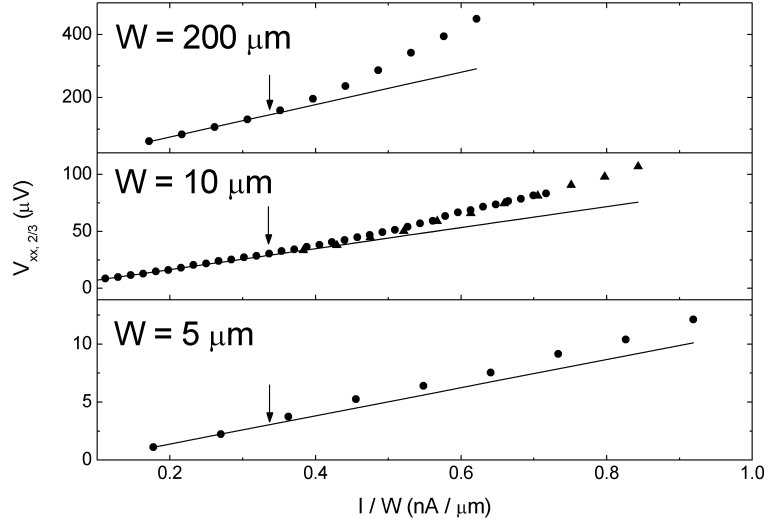


FIGURE 5.11: Longitudinal voltage at filling factor $\frac{2}{3}$ for devices with different Hall bar widths, plotted as a function of the normalized applied current. The onset of the non-linearity due to the development of the HLR is almost constant for the three devices and is indicated by the vertical arrows.

results measured with the gate voltage set to zero. The upper panel shows the longitudinal resistivity in the low (0.3 nA and 0.4 T/min, thin black line) and in the high current regime (1.8 nA and 2mT/min, thick red line). The peak related to the spin transition is present at 9.8 T also in this small device. The lower panel shows the $V(I)$ characteristic of the peak at 9.8 T. As in the wider devices the non-linearity sets in at a critical current density of about 0.33 nA/ μm .

To conclude this section, the quantum Hall ferromagnetism seems to behave in the same way in Hall bars 200, 10, 5 and 2 μm wide.

5.5 SAW measurement: small current regime

The rest of this chapter represents the main part of our work. It presents the experimental investigation of the spin phase transition at $\nu = \frac{2}{3}$ based on SAW measurements. All the SAW measurements shown are performed in the so-called low power regime. This means that the measurements are not affected by the acoustic power. In order to avoid excessive heating of the 2DEG the power fed to the coaxial lines is below -20 dbm.

In this section we concentrate on the low current regime. The data shown have been measured on sample A.

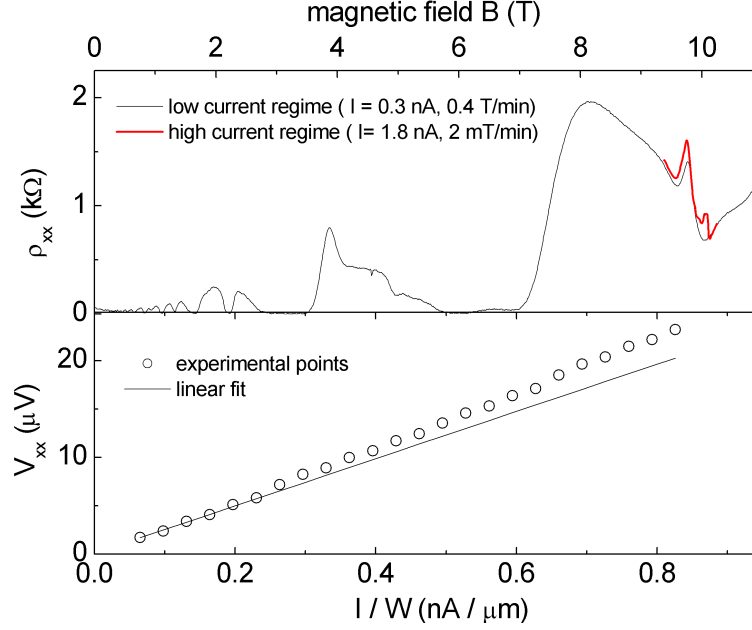


FIGURE 5.12: Upper panel: quasi-DC longitudinal resistivity for a Hall bar $2 \mu\text{m}$ wide in the low (thin black curve) and high current regime (thick red curve). The peak related to the phase transition is detected at 9.8 T. Lower panel: $V(I)$ characteristic of the peak at 9.8 T.

Fig. 5.13, upper panel, shows the longitudinal resistivity for the two B-sweep directions (black line B-sweep up, red line B-sweep down). The lower panel plots the normalized velocity shift recorded during the same magnetic field sweeps. The vertical dashed line indicates the position of $\nu = \frac{2}{3}$. The velocity shift increases whenever the conductivity falls below a certain critical value, as expected from the model presented in Sec. 4.2⁴. This is evident at low and high magnetic fields. In the rest of this thesis we will focus on the magnetic field region close to $\nu = \frac{2}{3}$. For better comparison we will plot the normalized longitudinal conductivity measured with quasi-DC and SAW techniques.

The normalized quasi-DC conductivity is obtained by inverting the resistivity tensor according to the formula

$$\bar{\sigma} = \begin{pmatrix} \sigma_{xx} & \sigma_{xy} \\ \sigma_{yx} & \sigma_{yy} \end{pmatrix} = \bar{\rho}^{-1} = \frac{1}{\rho_{xx}\rho_{yy} - \rho_{xy}\rho_{yx}} \begin{pmatrix} \rho_{yy} & -\rho_{xy} \\ -\rho_{yx} & \rho_{xx} \end{pmatrix}.$$

⁴This is not true for the total magnetic field region corresponding to filling factor 2. See Sec. 4.3.2 for discussion.

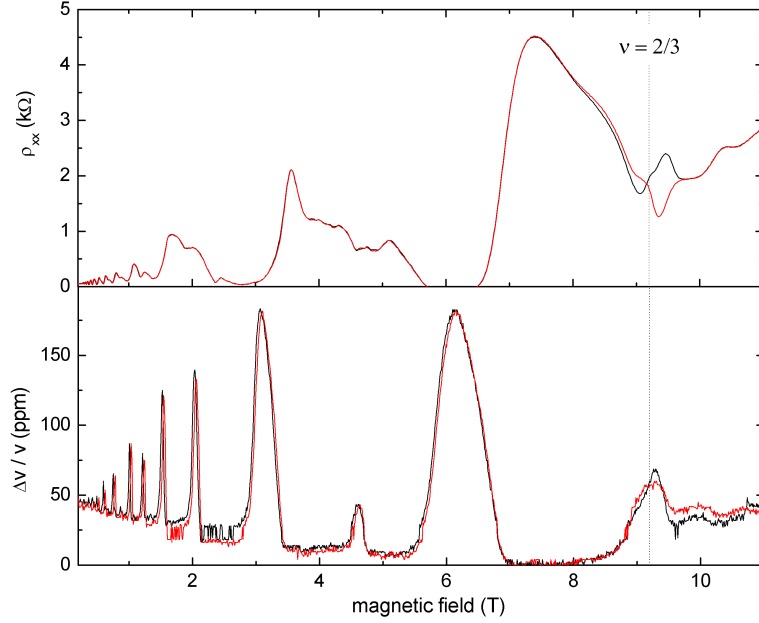


FIGURE 5.13: Upper panel: longitudinal resistivity measured with quasi-DC techniques for B-field swept upwards (black curve) and downwards (red curve) for sample A in the low current regime. Lower panel: normalized velocity shift of a SAW with a frequency of about 233 MHz recorded during the same magnetic field sweeps.

The SAW conductivity is derived using

$$\frac{\sigma_{xx}}{\sigma_m} = \sqrt{\frac{k_{eff}^2}{2} \frac{v}{\Delta v} - 1} \quad (5.2)$$

obtained by inverting Eq. 4.5. Fig. 5.14 shows the result of this procedure applied to the measurements of Fig. 5.13. The curve representing the B-sweep up is plotted in black and the one corresponding to the B-sweep down in red. In the upper panel the quasi-DC measurement is plotted. A small peak with strong hysteresis replaces the minimum in the longitudinal conductivity expected in the fractional quantum Hall regime. This behavior is in agreement with the one shown in Sec. 5.2 (see the longitudinal resistivity in Fig. 5.4). The lower panel shows the conductivity as determined by monitoring the velocity shift of a SAW, with the same scale as for the quasi-DC σ_{xx} . One can clearly notice the minimum in the conductivity expected for the filling factor $\frac{2}{3}$ but, really surprising, no peaks related to the spin-phase transition are discernible from this measurement. No sign of quantum Hall ferromagnetism is present in the conductivity measured at 233 MHz!

As mentioned in Sec. 4.3, our transducers can also operate at odd harmonics.

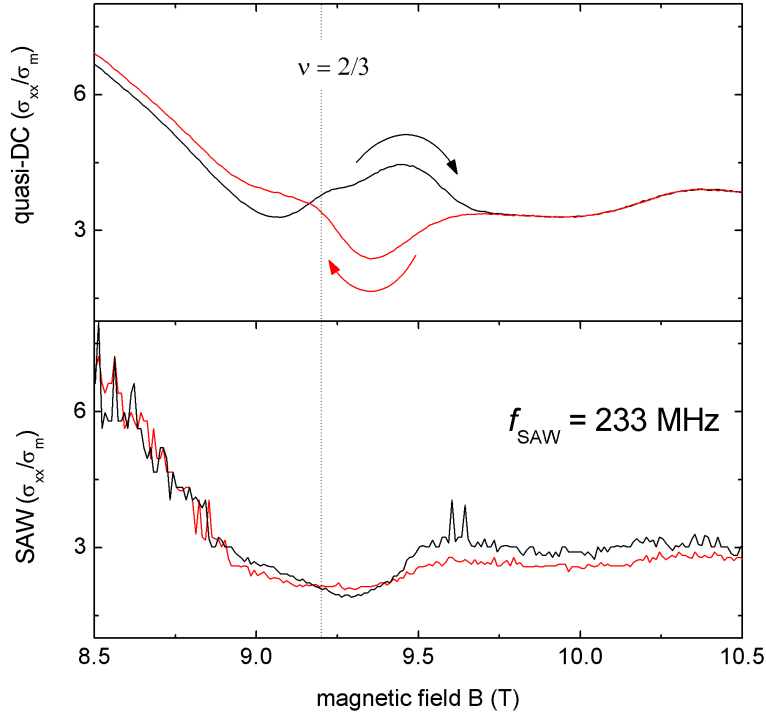


FIGURE 5.14: Upper panel: longitudinal conductivity measured with quasi-DC techniques for B-field swept upwards (black curve) and downwards (red curve) for sample A in the low current regime close to filling factor $\frac{2}{3}$. Lower panel: the same but determined from the velocity shift of a SAW at a frequency of about 233 MHz during the same magnetic field sweeps.

We use this property to study the sample at higher frequency. Fig. 5.15 shows the results obtained with frequencies of about 705 MHz and 1.2 GHz. In the upper panel we show the longitudinal conductivity measured with quasi-DC techniques for comparison. As in Fig. 5.14, the phase transition appears as a peak in the quasi-DC conductivity with hysteretic behavior. In the middle and lower panels the conductivity deduced from the velocity shift is shown for a SAW frequency of 705 MHz (middle panel) and of 1.2 GHz (lower panel). As for the curve at 233 MHz in Fig. 5.14 no sign of ferromagnetism is present. We want to stress here that the resolution of our setup allows the measurement of changes in the velocity of the SAW smaller than 1 part-per-million, corresponding to σ_{xx}/σ_m changes of 0.02.

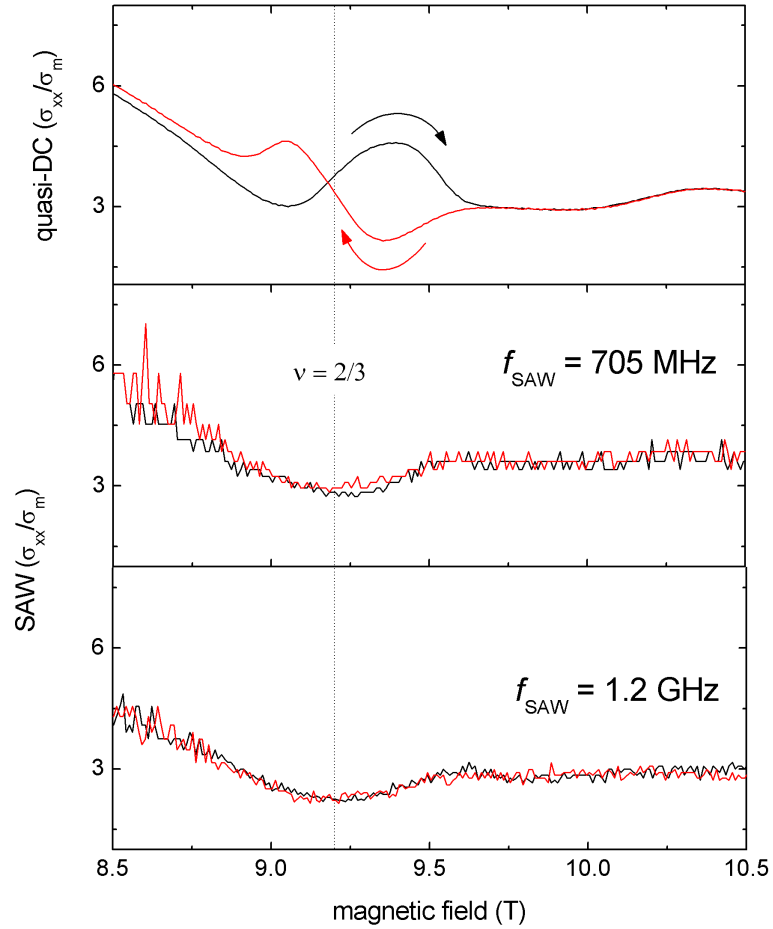


FIGURE 5.15: Upper panel: longitudinal conductivity measured with quasi-DC techniques for B-field swept upwards (black curve) and downwards (red curve) for sample A in the low current regime close to filling factor $\frac{2}{3}$. Middle and lower panel: the same but determined from the velocity shift of a SAW at a frequency of about 705 MHz (middle panel) and 1.2 GHz (lower panel).

5.6 SAW measurement: high current regime

We now concentrate our SAW study to the high current regime.

Fig. 5.16 shows the longitudinal conductivity in the high current regime measured with the quasi-DC technique (upper panel) and with a SAW of 233 MHz (lower panel) to be compared with Fig. 5.14.

In the quasi-DC conductivity the development of the HLR is taking place. Instead of a small local maximum at the fractional filling factor we detect a huge peak. As in the low current regime, the increase of the conductivity at filling factor $\frac{2}{3}$, well

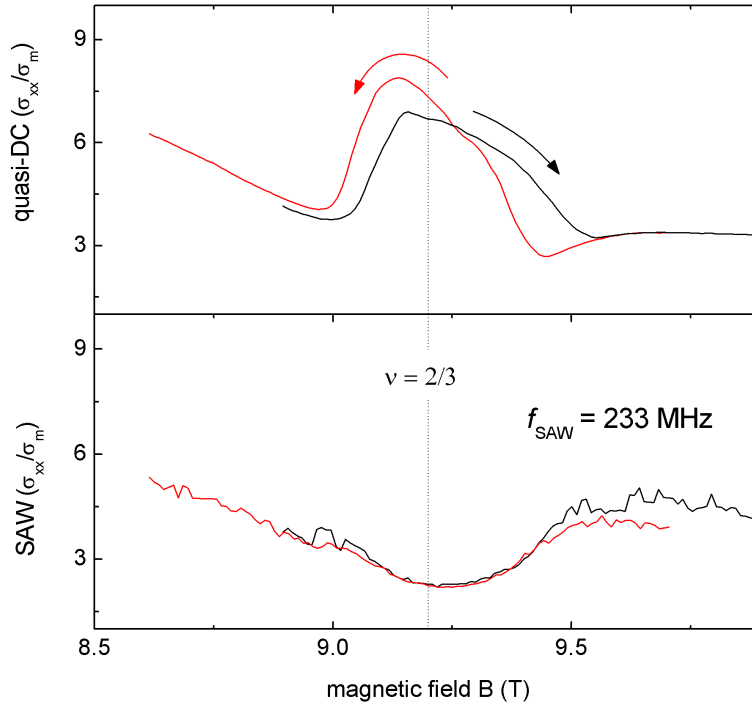


FIGURE 5.16: Upper panel: longitudinal conductivity measured with quasi-DC techniques for B-field swept upwards (black curve) and downwards (red curve) for sample A in the high current regime, close to filling factor $\frac{2}{3}$. Lower panel: the same but determined from the velocity shift of a SAW at a frequency of about 233 MHz during the same magnetic field sweep. Figure to be compared with Fig. 5.14

distinguishable in the quasi-DC measurement, is missing in the SAW measurement. The minimum at $\nu = \frac{2}{3}$ remains. Due to the resolution of our measurement we can state that if a peak is present in the SAW conductivity it has to be at least 100 times smaller than in the quasi-DC case. We can repeat the same kind of measurement for the other harmonics but, as shown in Fig. 5.17 (to be compared with Fig. 5.15), the result remains the same.

Fig. 5.18 summarizes the conductivity measurements in the low current (left panel) and in the high current regime (right panel) for a magnetic field changing upwards (black curves) and downwards (red curves). In the top panels we show the dramatic difference seen in the quasi-DC data between the two regimes. In the lower panel we show the high-frequency data for SAW frequencies of 233 MHz, 705 MHz and 1.2 GHz. The signatures of the phase transition seen in the quasi-DC conductivity are missing in the SAW one.

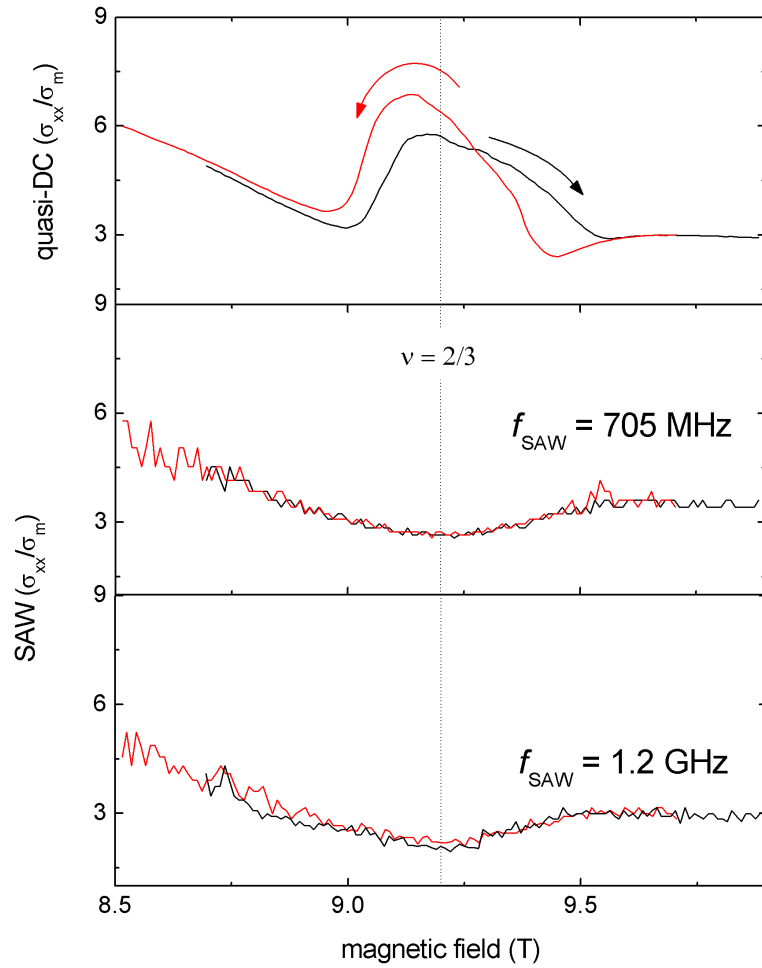


FIGURE 5.17: Upper panel: longitudinal conductivity measured with quasi-DC techniques for B-field swept upwards (black curve) and downwards (red curve) for sample A in the high current regime, close to filling factor $\frac{2}{3}$. Middle and lower panel: the same but determined from the velocity shift of a SAW at a frequency of about 705 MHz (middle panel) and 1.2 GHz (lower panel). Figure to be compared with Fig. 5.15

5.7 Acousto-electric measurements

The most simple explanation for the observed phenomena is that the SAWs do not couple to the quasi-particles at the domain wall responsible for the conductivity maximum at the phase transition. We performed acousto-electric measurements to show that this is not the case.

Fig. 5.19 shows the longitudinal drag voltage measured in sample B with an acoustic power of -10 dbm (upper curve) together with the result calculated using Eq. 4.10

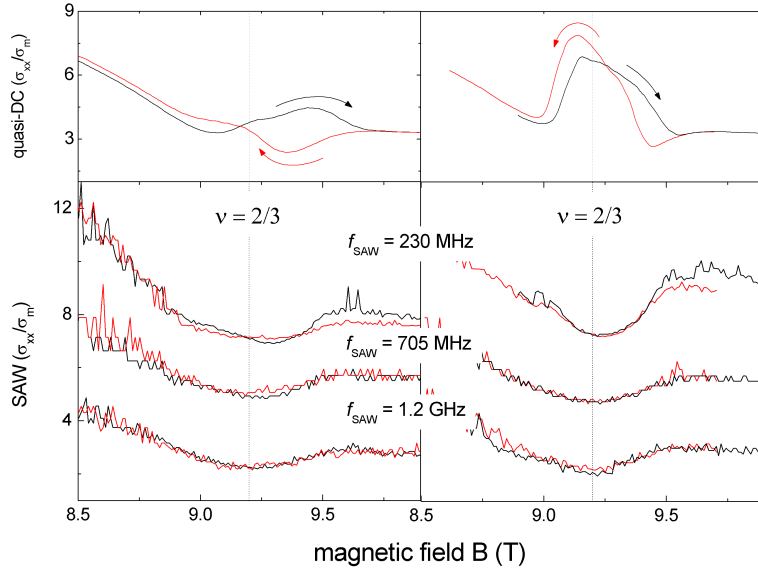


FIGURE 5.18: Upper panels: longitudinal conductivity measured with quasi-DC techniques for B-field swept upwards (black curves) and downwards (red curves) for sample A in the low (left panel) and high current regime (right panel) close to filling factor $\frac{2}{3}$. Lower panels: the same but determined from the velocity shift of a SAW at a frequency of about 233 MHz, 705 MHz and 1.2 GHz (from top to bottom). The figures are shifted vertically by 2.5 for clarity.

(lower curve).

Only the magnetic field region close to the spin transition is plotted in the figure. From the calculated curve we expect that the drag signal shows a local maximum at the transition. This is in fact what we detect in the experiment. As mentioned in Sec. 4.3.2 the theory is not able to predict the result quantitatively. Also the prediction of a negative drag at about 9.7 T is not reproduced in the experimental curve. It is however important that in both curves of Fig. 5.19 a peak is present at the phase transition (dotted line).

This ensures that the SAWs couple to the excitations characterizing the quantum Hall ferromagnet.

In the measurement shown the voltage of the back-gate is set to zero and therefore the spin transition is not exactly at $\nu = \frac{2}{3}$. Setting the correct electron density does not change the experimental findings but the transition peak becomes less sharp in the experimental and in the calculated curve.

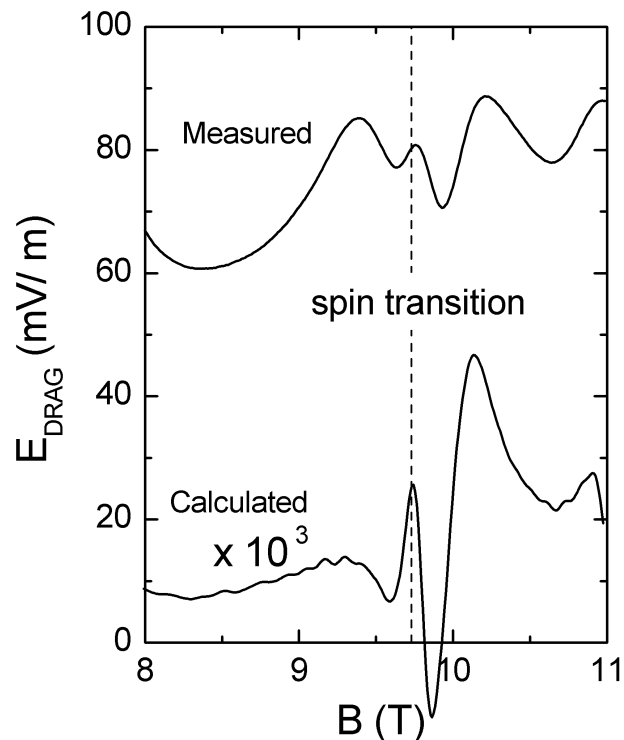


FIGURE 5.19: Longitudinal drag voltage detected on sample B in a magnetic field region close to the spin phase transition. The upper curve is the experimental measurement for an acoustic power of -10 dbm. The lower curve is calculated using Eq. 4.10.

5.8 Domain orientation at the transition

In our experiment the acoustic field is formed by (almost) straight wave fronts perpendicular to the direction of the current and propagating parallel to it. To detect some changes in the SAW conductivity the acoustic wave has to propagate across regions of different conductivity. This means that it has to cross the domain walls. If the domains are in shape of stripes parallel to the direction of the SAW propagation the same conductivity will be measured with and without domains and the phase transition would not be detected. Unfortunately, due to space constraints in the cryostat, it was not possible to install extra coaxial cables in order to have two SAW beams propagating perpendicular to each other. There are two other parameters that give a preferential direction to our experiment: the surface roughness and the current direction. We have not checked yet the dependence on the surface roughness in our devices. We have however performed measurements in which the direction

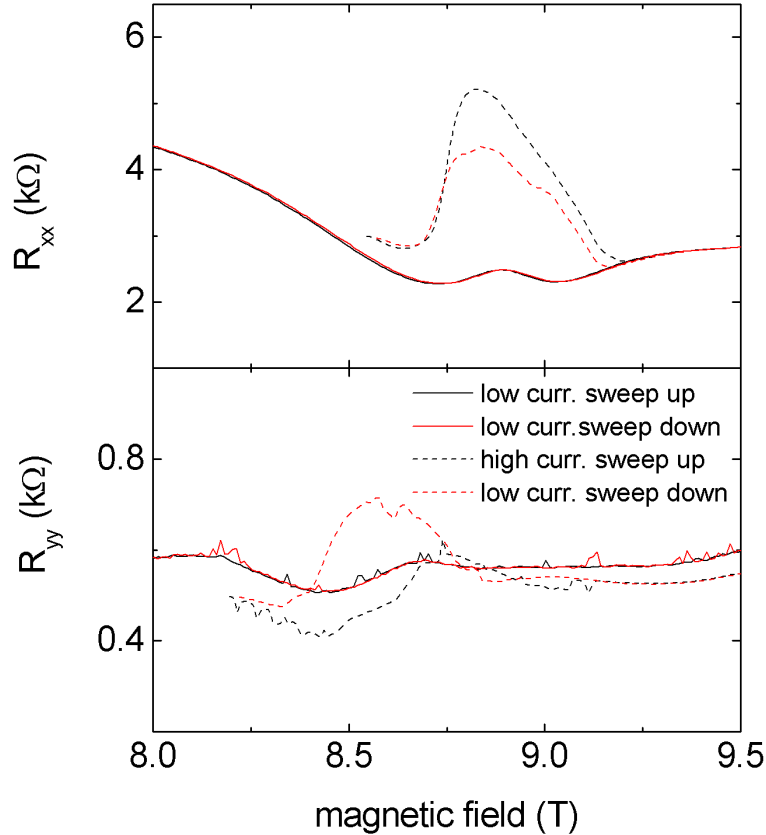


FIGURE 5.20: Quasi-DC resistance measured parallel to the direction of the applied current. Upper panel: resistance measured with the B-field swept upwards (black curve) and downwards (red curve) for sample B in the low and high current regime respectively, with the current applied parallel to the long side of the Hall bar. Lower panel: the same but measured with the current applied parallel to the short side of the Hall bar

of the current was changed. During the measurements that we showed so far the current for the quasi-DC measurement, whose effects especially in the high current regime are not negligible, has been applied along the long side of the Hall bar (see Fig. 4.5). It is also possible to apply the current along the short side of the Hall bar⁵. Fig. 5.20 plots the quasi-DC measurements for the two experimental configurations, i.e. when the current is applied along the long side of the Hall bar (upper panel) and the short side (lower panel) in the low and high current regime, respectively. We see in both configurations some features close to the phase transition suggesting that the current has some effect on the domain morphology. However, the high current regime

⁵Note that in this case the potential probes are far from the current path.

is quite different for the two configurations. Moreover, without changing the voltage applied to the back-gate, the magnetic field value of the minimum (most likely) associated with $\nu = \frac{2}{3}$ depends on the direction of the applied current (about 8.8 T for the upper panel and about 8.4 T for the lower panel). This effect is not clear yet. Fig. 5.21 shows the SAW conductivity in the HLR regime when the current is applied along the long (lower right panel) and the short (lower left panel) side of the Hall bar. The black curves represent the longitudinal conductivity when the B-field is swept upwards, the red curves the downward sweeps. We also show in the upper panel the quasi-DC conductivity measured when the current is applied along the long side of the Hall bar. No clear difference can be detected between the two experimental configurations. A complete study of the domain orientation with respect to the

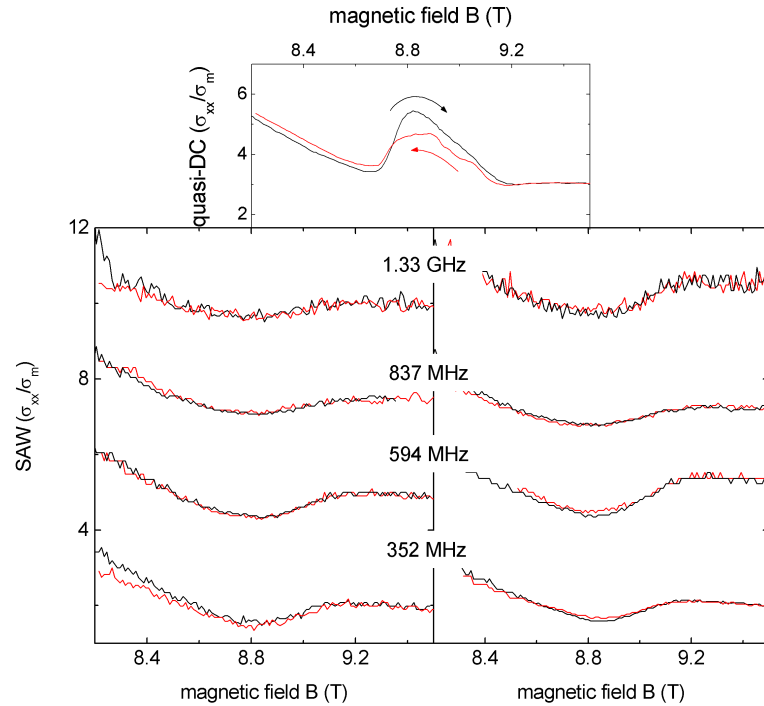


FIGURE 5.21: Upper panel: longitudinal conductivity measured with quasi-DC techniques for B-field swept upwards (black curve) and downwards (red curve) for sample B in the high current regime, close to filling factor $\frac{2}{3}$, with the quasi-DC current applied parallel to the long side of the Hall bar. Lower right panel: the same but determined from the velocity shift of a SAW at a frequency of 352 MHz, 594 MHz, 836 MHz and 1.33 GHz (from top to bottom). Lower left panel: the same as the right panel but measured when the quasi-DC current is applied parallel to the short side of the Hall bar. The curves are shifted vertically by 2.5 for clarity.

in-plane magnetic field, current direction, crystallographic direction and so on is an interesting topic that requires additional experiments to be performed.

5.9 Discussion

We studied the spin phase transition at $\nu = \frac{2}{3}$ monitoring the effect of the 2DES on the propagation of a SAW. We used SAWs with frequencies ranging from 100 MHz to more than 1 GHz, corresponding to wavelength from 25 μm to 2 μm . The conclusion is the same for all the cases: no sign of QHF is detected with SAWs.

In our experiment we send with the input IDT an ensemble of SAWs, each one of a different frequency, centered at the resonance one. With the output transducer we determine the effect of the 2DES on each component of the input ensemble; from that we deduce the shift of the group velocity. What we really measure is the change of the phase of each component of the SAW ensemble due to the interaction with the system under study. The phase shift ϕ due to the propagation through a homogeneous system of length L and SAW velocity v , for a SAW of frequency f , is $\phi = L \frac{2\pi f}{v}$.

Now we focus on the system of our experimental investigation and perform some quantitative analysis.

We divide our system (2DES plus GaAs crystal) into two different regions. One region (region 1) indicates the domains and is characterized by a conductivity σ_1 and a SAW velocity v_1 ⁶. The second region (region 2) indicates the domain walls; it has a conductivity σ_2 and a SAW velocity v_2 . Since the wavefront of the SAW are (almost) plane wave in the direction perpendicular to the SAW propagation, we consider the system invariant along the direction parallel to the wavefront. We indicate the length of the region 1 with D and the length of region 2 with d (see Fig. 5.22).

We consider first the situation in which domain walls do not exist and we have a single homogeneous region of type 1. The phase shift of a SAW of frequency f due to the 2DES only is

$$\phi' = (D + d) \frac{2\pi f}{v_1} - (D + d) \frac{2\pi f}{v_0} = (D + d) 2\pi f \left(\frac{1}{v_1} - \frac{1}{v_0} \right) \quad (5.3)$$

⁶This type includes domains of both polarization, one and zero. In our system we do not expect a conductivity that depends on the electron polarization.

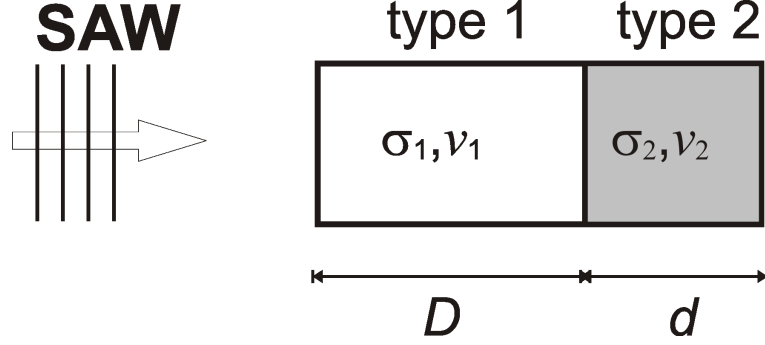


FIGURE 5.22: Sketch of the model used to calculate the effect of an inhomogeneous system on the propagation of a SAW. The sample (2DES + GaAs crystal) is divided into two regions, each one characterized by a velocity v , a conductivity σ and a length D or d .

where v_0 is the SAW velocity on GaAs.

If we include domain walls the phase shift is

$$\phi'' = D2\pi f \left(\frac{1}{v_1} - \frac{1}{v_0} \right) + d2\pi f \left(\frac{1}{v_2} - \frac{1}{v_0} \right). \quad (5.4)$$

In our experiment we do not detect any difference between the situation with domain walls and without. Our resolution allows us to state that if a difference exists, it has to be at least 100 times smaller than in the case of a homogeneous electron system. This can be written in mathematical terms as

$$|\phi'' - \phi'| < 0.01 |\phi'|. \quad (5.5)$$

The changes in the SAW velocity (i.e. in the phase shift) at the phase transition are very small (see Fig. 5.13). We can therefore use a Taylor expansion and write

$$\frac{1}{v} - \frac{1}{v_0} \approx -\frac{1}{v_0^2} (v - v_0). \quad (5.6)$$

Combining Eq. 5.6 with Eq. 5.3, Eq. 5.4 and Eq. 5.5 we arrive to the following condition

$$d \left| \frac{v_2 - v_0}{v_0} - \frac{v_1 - v_0}{v_0} \right| < 0.01(D + d) \left| \frac{v_1 - v_0}{v_0} \right|. \quad (5.7)$$

According to the theory presented in Sec. 4.2 the velocity shift is related to the conductivity. Using Eq. 4.5 we can rewrite Eq. 5.7 as

$$|\sigma_1^2 - \sigma_2^2| < 0.01 \frac{D + d}{d} (\sigma_m^2 - \sigma_2^2). \quad (5.8)$$

We can solve this formula numerically. We arrive to the conclusion that for $\sigma_2 > \sigma_1$ (as in our case) the inequality is satisfied only for $\frac{d}{D+d} < 0.01$. In other words, the region occupied by the domain walls is 100 times smaller than the region domain walls plus domains themselves.

The limit that we obtain can be used to obtain additional information on the domain extension. Before doing that, let us mention the prediction of the theory of QHF (Sec. 3.2).

According to Hartree-Fock calculation the extra (quasi-DC) dissipation at the crossing between LLs is due to the propagation across the 2DES of quasi-particles confined to the domain walls. According to the same theories the width of a single domain wall is about $2l_B$ [38, 45]. However, strictly speaking, the Hartree-Fock approximation is not valid in the fractional quantum Hall regime due to the high electron correlations. One can employ the composite fermion framework and substitute the highly correlated electron system with a weakly interacting CF system. In this picture the electron magnetic length l_B is substituted by the CF magnetic length l_B^{eff} . After this operation we obtain a value for the width of a single domain wall of roughly 34 nm.

Now we return to the possible interpretation of our experimental findings.

Surface wave technique has been proven advantageous for the study of spatial inhomogeneities in 2DESs [108, 138, 139]. In fact, since a SAW integrates over the whole sample area, it can directly yield information about the spatial uniformity of the electron system. This means that the upper limit that we obtain from our data (1%) refers to the amount of domain walls present in the whole sample. Since the Hall bar that we use is 1 mm long, the total domain wall width results smaller than $10 \mu\text{m}$. Recalling that according to theory each domain wall is about 34 nm wide, we end up with a maximum number of domain wall of about 300. This number (plus one to be precise) represents also the maximum number of domains in our 2DES. A straightforward calculation brings to the conclusion that the average extension of a single domain at $\nu = \frac{2}{3}$ has to be larger than $3.3 \mu\text{m}$.

We can check if this value is reasonable by comparing it with the results obtained from the quasi-DC measurements in small Hall bars presented in Sec. 5.4.

In the data of Fig. 5.9 and Fig. 5.12 the QHF seems not to change substantially by reducing the width of the Hall bar from $200 \mu\text{m}$ to 10, 5 and $2 \mu\text{m}$. This is in agreement with the picture of domain walls that at the transition run from one edge of the sample to the other. They produce backscattering between the edge

states and lead to dissipation regardless of how far apart the two edge are. This picture gives credit to our model in which the direction perpendicular to the SAW propagation is not playing an important role. The fact that the QHF is present also when the width of the Hall bar is smaller than our limit for the domain extension is not a contradiction in this picture. Now we focus on the measurement shown in Fig. 5.10 performed on the same device but using different voltage probes. We detect a resistivity peak at the spin phase transition when the center-to-center distance of the contact arms is $10 \mu\text{m}$, meaning that the source of backscattering responsible for the extra dissipation is present between the two contacts. Also this observation agrees with our lower limit: since the average domain size is smaller than $10 \mu\text{m}$, at least one domain wall is present between the two voltage probes.

In conclusion, based on a simple model of SAW propagation in an inhomogeneous 2DES, we can state that the region of the sample occupied by domain walls is less than 1% of the whole sample area. Using Hartree-Fock estimates for the domain wall width we conclude that the average domain size at the transition is larger than $3.3 \mu\text{m}$. A more accurate model should take into account other factors like the possible reflection and diffraction of a SAW at the domain walls. We do not think that these improvements would change our limit dramatically. Finally, we checked the validity of our model by comparison with quasi-DC measurements performed on Hall bar of small size.

Before concluding this section we want to remark one further aspect of our findings. We discussed our measurements comparing the conductivity detected with SAWs and with quasi-DC currents. One could argue that this is not valid since $\sigma_{xx} = \sigma_{xx}(\omega, k)$. With the two methods we probe different regions of the dispersion curve of the excitations at the domain wall. These two regions are not necessarily similar. This argument should apply also for the acoustoelectric measurements. However we detect a similar response when exciting the 2DES with SAWs and when calculating the drag signal from the quasi-DC measurements. We can therefore say that acoustic dispersion effects are negligible.

6 Conclusions

In this thesis we investigate the spin phase transition at filling factor $\frac{2}{3}$ with both quasi-DC and SAW techniques.

The first part of this work is the design and realization of a setup that allows low and high frequency measurements at temperatures as low as 0.4 K. This includes the choice of the low-loss coaxial cables for the HF signal and a proper thermal anchoring for efficient heat dissipation. In order to reduce the cross-talk signal between the transducers a special sample holder has been designed which includes SMP connectors and coplanar waveguides for the signal transmission. Great care has been taken also in the design of interdigital transducers for SAW generation and detection.

We use Hall bars with IDTs at the opposite sides of the 2DES. The quasi-DC σ_{xx} is calculated from the resistivities measured with excitation currents of a few Hz. The SAW σ_{xx} is simultaneously determined from the SAW absorption and dispersion.

A conductivity maximum signals the transition between differently polarized ground states in the quasi-DC measurements. All standard magneto-transport oscillations seen with quasi-DC are reproduced with SAWs. However the conductivity peak at the spin transition is not. This absence is reproduced for acoustic frequencies ranging from 100 MHz to more than 1 GHz (wavelengths from 25 μm to 2 μm). We exclude the possibility of stripe domains induced by the quasi-DC current by checking that the results remain the same changing the direction of the applied current. The conductivity peak is absent in the SAW σ_{xx} also when the quasi-DC current is increased and the quasi-DC conductivity presents the dramatic enhancement known as huge longitudinal resistance (HLR) regime. This effect is caused by the hyperfine interaction between the electronic and nuclear spins, the latter becoming polarized by the huge current (dynamical nuclear polarization).

One could argue that the SAWs do not couple to the excitations at the domain walls. We check that this is not the case by performing acousto-electric measurements: a SAW interacts with a 2DES by exchanging momentum with the mobile carriers. This momentum transfer leads to the generation of drag voltages in the 2DES. Measuring the longitudinal drag voltage we detect a peak in the signal at the

spin transition. The presence and the position of this peak agree with theoretical predictions and yield evidence of a coupling between SAWs and the quasi-particle responsible for the quantum Hall ferromagnetism.

In the SAW measurements we monitor the phase shift of the acoustic wave after that it interact with the whole sample. Our results are therefore integrated over the whole area of an inhomogeneous 2DES. In order to obtain a quantitative estimate of the domain width we model the sample as divided into two regions, each of them characterized by a conductivity, a SAW velocity and a spatial extension. One region indicates the area occupied by the domain walls, while the other indicates the area occupied by the domains themselves. We then assume that the total phase shift is the sum of the phase shift acquired in each single region. Following this simple model the resolution of our experiment allow us to state that the region occupied by the domain walls is about 1% of the whole sample area. Using Hartree-Fock estimates for the width of a single domain wall we arrive to the conclusion that at $\nu = \frac{2}{3}$ the domains are larger than $3.3 \mu\text{m}$.

We checked the validity of this value by comparing with quasi-DC measurements performed on Hall bar of small size.

In future experiments the precision of the SAW measurements must be enhanced and/or smaller Hall bars for the quasi-DC test must be used¹. This would allow to either determine the domain size more accurately or to exclude their existence altogether.

Other kinds of interaction can occur between a domain wall and a surface acoustic wave. Several studies [140, 141, 142, 143, 144, 145, 146] show that it is possible to trap electrons in the potential minima of a SAW and drag them over macroscopic distances. In our experiment we can exclude this phenomenon since the acoustic power that we drive into our devices is much smaller (at least 20 times) than the one needed to confine the carriers. Using hybrid structures or different IDT geometries could allow some electrons to be dragged across the domain wall. This process would require the flip of the electron spin adding an additional energy cost. In the high current regime this cost is considered to be the cause of the HLR while in this case it would come from the energy of the SAW. In other words, the HLR could be made disappear by simply adding a SAW. In preliminary experiments the heating

¹This last hypothesis can be technologically not easy to improve since the resistance minima at $\nu = \frac{2}{3}$ become weaker in such small Hall bars.

due to the high acoustic power smears out all the features present in the transport curves and technological improvements has to be considered.

One could also think to drag not only electrons but also the skyrmion-like excitations at the domain boundaries. This would imply to move the domain walls themselves. In ferromagnetic materials and magnetic semiconductors the domain walls are normally moved by using pulsed DC current [147, 148]. Recently Saitoh *et al.* [149] reported the motion of a domain wall after applying an AC current. It is however not clear if by using an AC current (or a SAW) it is really possible to move the domain wall over macroscopic distances or if the only result is an induced oscillating motion around the equilibrium position. Performing these high power studies for a quantum Hall ferromagnet requires however special attention in order to avoid excessive heating of the 2DES.

To conclude, this work opens a new door to study the topology of a quantum Hall ferromagnet. The technique used in this thesis can be applied also to different types of QHF. There the different kinds of ferromagnetic order can lead to domain morphology and low-energy excitations that can give different responses to SAW excitations. Two-dimensional bilayer systems seem to be very attractive. In these systems it is actually possible to induce a transition between an easy-axis to an easy-plane ferromagnetic ordering. SAW detection is a powerful technique to study the phenomenology of this process.

A Sample structure

The measurements shown in this thesis are obtained from two different wafers: 81644 and 8813. They have been both grown by molecular beam epitaxy at the Max-Planck-Institut in Stuttgart by Maik Hauser.

A.1 Wafer 81644

The sample has been grown the 29th July 2005. The detailed structure, from top to bottom, is the following:

GaAs	20 nm
AlGaAs	20 nm
AlGaAs Si-doped	40 nm
AlGaAs	140 nm
GaAs	15 nm
AlGaAs	160 nm
AlGaAs Si-doped	30 nm
AlGaAs	100 nm
GaAs	2 nm
AlAs	2 nm
GaAs	300 nm
100 × GaAs/AlAs	2nm/2nm
GaAs	Substrate.

A.2 Wafer 8813

The sample has been grown the 12th June 1997. The detailed structure, from top to bottom, is the following:

A Sample structure

GaAs	10 nm
AlGaAs	10 nm
AlGaAs Si-doped	60 nm
GaAs	20 nm
AlGaAs	20 nm
GaAs	1000 nm
50 × GaAs/AlAs	5nm/5nm
GaAs	250 nm
GaAs	Substrate.

Bibliography

- [1] For a review see T. Chakraborty and P. Pietiläinen, *The Quantum Hall Effects: Integral and Fractional* 2nd ed. (Springer-Verlag, Berlin, 1995). 18, 19, 20, 21
- [2] K. von Klitzing, G. Dorda, and M. Pepper, “New Method for High-Accuracy Determination of the Fine-Structure Constant Based on Quantized Hall Resistance”, *Phys. Rev. Lett.* **45**, 494 (1980). 20
- [3] K. von Klitzing, “The quantized Hall effect”, *Rev. Mod. Phys.* **58**, 519 (1986). 20
- [4] B. N. Taylor, “Basic standards and fundamental constants”, *IEEE Trans. Instrum. Meas.* **38**, 164 (1989). 20
- [5] H. Bachmair, E. O. Göbel, G. Hein, J. Melcher, B. Schumacher, *et al.*, “The von Klitzing resistance standard”, *Physica E* **20**, 14 (2003). 20
- [6] For a review see T. Ando and A. Fowler and F. Stern, *Rev. Mod. Phys.* 54, 437 (1982). 20
- [7] M. Janßen, O. Viehweger, U. Fastenrath, and J. Hajdu, *Introduction to the Theory of the Integer Quantum Hall Effect* (VCH Weinheim Heidelberg, Heidelberg, 1994). 20
- [8] Edited by S. Das Sarma and A. Pinczuk, *Perspectives on Quantum Hall Effects*, (Wiley, New York, 1996). 20, 25
- [9] S. M. Girvin, *1998 Les Houches Summer School Lecture* (Springer-Verlag and Editions de Physique, New York and Les Ulis, 2000). 22, 30
- [10] Edited by O. Heinonen, *Composite Fermions: A Unified View of the Quantum Hall Regime*, (World Scientific, Singapore, 1998). 25, 27
- [11] R. Tao and D. Thouless, “Fractional quantization of Hall conductance”, *Phys. Rev. B* **28**, 1142 (1983). 25
- [12] D. H. Lee, G. Baskaran, and S. Kivelson, “Generalized Cooperative-Ring-Exchange Theory of the Fractional Quantum Hall Effect”, *Phys. Rev. Lett.* **59**, 2467 (1987). 25

- [13] G. Murthy and R. Shankar, “Hamiltonian theories of the fractional quantum Hall effect”, *Rev. Mod. Phys.* **75**, 1101 (2003). 25
- [14] R. B. Laughlin, “Anomalous Quantum Hall Effect: An Incompressible Quantum Fluid with Fractionally Charged Excitations”, *Phys. Rev. Lett.* **50**, 1395 (1983). 25, 26
- [15] R. B. Laughlin, “Nobel lecture: fractional quantization”, *Rev. Mod. Phys.* **71**, 863 (1999). 25, 26
- [16] R. de Picciotto, M. Reznikov, M. Heiblum, V. Umansky, G. Bunin, and D. Mahalu, “Direct observation of a fractional charge”, *Nature* **389**, 162 (1997). 26
- [17] V. J. Goldman and B. Su, “Resonant Tunneling in the Quantum Hall Regime: Measurement of Fractional Charge”, *Science* **267**, 1010 (1995). 26
- [18] F. E. Camino, W. Zhou, and V. J. Goldman, “Realization of a Laughlin quasiparticle interferometer: Observation of fractional statistic”, *Phys. Rev. B* **72**, 075342 (2005). 26
- [19] F. E. Camino, W. Zhou, and V. J. Goldman, “Aharonov-Bohm superperiod in a Laughlin quasiparticle interferometer”, *Phys. Rev. Lett.* **95**, 246802 (2005). 26
- [20] B. I. Halperin, “Statistic of Quasiparticles and the Hierarchy of Fractional Quantized Hall States”, *Phys. Rev. Lett.* **52**, 1583 (1984). 26
- [21] F. D. M. Haldane, “Fractional Quantization of the Hall Effect: A Hierarchy of Incompressible Quantum Fluid States”, *Phys. Rev. Lett.* **51**, 605 (1983). 26
- [22] R. B. Laughlin, “Fractional Quantization of the Hall Effect: A Hierarchy of Incompressible Quantum Fluid States”, *Surf. Sci.* **141**, 11 (1984). 26
- [23] J. K. Jain, “Composite-Fermion Approach for the Fractional Quantum Hall Effect”, *Phys. Rev. Lett.* **63**, 199 (1989). 27
- [24] J. K. Jain, “Composite Fermions in the Quantum Hall Regime”, *Science* **266**, 1199 (1990). 27
- [25] W. Pan, H. L. Störmer, D. C. Tsui, L. N. Pfeiffer, K. W. Baldwin, and K. W. West, “Fractional Quantum Hall Effect of Composite Fermions”, *Phys. Rev. Lett.* **90**, 016801 (2003). 27
- [26] J. H. Smet, “Wheels within wheels”, *Nature* **422**, 391 (2003). 27

-
- [27] S. L. Sondhi, A. Karlhede, S. Kivelson, and E. H. Rezayi, “Skyrmions and the crossover from the integer to fractional quantum Hall effect at small zeeman energies”, *Phys. Rev. B* **47**, 16 419 (1993). 30
- [28] T. H. R. Skyrme, *Proc. Royal. Soc. (London)* **A262**, 233 (1961). 30
- [29] S. M. Girvin, “Spin and Isospin: Exotic Order in Quantum Hall Ferromagnets”, *Physics Today* **June 2000**, 39 (2000). 31
- [30] S. E. Barrett, G. Dabbagh, L. N. Pfeiffer, K. W. West, and R. Tycko, “Optically Pumped NMR Evidence for Finite-Size Skyrmions in GaAs Quantum Wells near Landau Level Filling $\nu = 1$ ”, *Phys. Rev. Lett.* **74**, 5112 (1995). 31
- [31] V. Bayot, E. Grivei, S. Melinte, M. B. Santos, and M. Shayegan, “Giant Low Temperature Heat Capacity of GaAs Quantum Wells near Landau Level Filling $\nu = 1$ ”, *Phys. Rev. Lett.* **76**, 4584 (1996). 31
- [32] V. Bayot, E. Grivei, J. M. Beuken, S. Melinte, and M. Shayegan, “Critical Behavior of Nuclear-Spin Diffusion in GaAs/AlGaAs Heterostructures near Landau Level Filling $\nu = 1$ ”, *Phys. Rev. Lett.* **79**, 1718 (1997). 31
- [33] T. Jungwirth and A. H. MacDonald, “Pseudospin anisotropy classification of quantum Hall ferromagnets”, *Phys. Rev. B* **63**, 035 305 (2000). 32, 34
- [34] G. F. Giuliani and J. J. Quinn, “Spin-Polarization instability in a tilted magnetic field of a two-dimensional electron gas with filled Landau levels”, *Phys. Rev. B* **31**, 6228 (1985). 33
- [35] V. I. Fal’ko and S. V. Iordanskii, “Topological Defects and Goldstone Excitations in Domain Walls between Ferromagnetic Quantum Hall Liquids”, *Phys. Rev. Lett.* **82**, 402 (1999). 33
- [36] V. I. Fal’ko and S. V. Iordanskii, “Spin-Orbit Coupling Effect on Quantum Hall Ferromagnets with Vanishing Zeeman Energy”, *Phys. Rev. Lett.* **84**, 127 (2000). 33
- [37] M. Uchida, Y. Onose, Y. Matsui, and Y. Tokura, “Real-Space Observation of Helical Spin Order”, *Science* **311**, 359 (2006). 34
- [38] T. Jungwirth and A. H. MacDonald, “Resistance Spikes and Domain Wall Loops in Ising Quantum Hall Ferromagnets”, *Phys. Rev. Lett.* **87**, 216 801 (2001). 34, 99
- [39] T. Jungwirth, S. P. Shulka, L. Smrcka, M. Shayegan, and A. H. MacDonald, “Magnetic Anisotropy in Quantum Hall Ferromagnets”, *Phys. Rev. Lett.* **81**, 2328 (1998). 34

- [40] T. Jungwirth, A. H. MacDonald, L. Smrcka, and S. M. Girvin, “Field-tilt anisotropy energy in quantum Hall stripes states”, *Phys. Rev. B* **60**, 15 574 (1999). 34
- [41] E. P. D. Poortere, E. Tutuc, S. J. Papadakis, and M. Shayegan, “Resistance Spikes at Transitions Between Quantum Hall Ferromagnets”, *Science* **290**, 1546 (2000). 34, 36
- [42] J. T. Chalker, D. G. Polyakov, F. Evers, A. D. Mirlin, and P. Wölfle, “Quantum Hall ferromagnets, cooperative transport anisotropy, and the random field Ising model”, *Phys. Rev. B* **66**, 161 317 (2002). 34
- [43] U. Zeitler, H. W. Schumaker, A. G. M. Jansen, and R. J. Haug, “Magnetoresistance Anisotropy in Si/SiGe in Tilted Magnetic Fields: Experimental Evidence for a Stripe-Phase Formation”, *Phys. Rev. Lett.* **86**, 866 (2001). 34, 36
- [44] W. Pan, H. L. Stormer, D. C. Tsui, L. N. Pfeiffer, K. W. Baldwin, and K. W. West, “Highly anisotropic transport in the integer quantum Hall effect”, *Phys. Rev. B* **64**, 121 305(R) (2001). 34, 36
- [45] L. Brey and C. Tejedor, “Spins, charges, and currents at domain walls in a quantum Hall Ising ferromagnet”, *Phys. Rev. B* **66**, 041 308(R) (2002). 34, 99
- [46] H. J. P. Freire and J. C. Egues, “Hysteretic resistance spikes in quantum Hall ferromagnets without domains”, *cond-mat/0412491*. 35
- [47] J. Jaroszyński, T. Andrearczyk, G. Karczewski, J. Wróbel, T. Wojtowicz, *et al.*, “Ising Quantum Hall Ferromagnet in Magnetically Doped Quantum Wells”, *Phys. Rev. Lett.* **89**, 266 802 (2002). 35, 36
- [48] S. Koch, R. J. Haug, K. von Klitzing, and M. Razeghi, “Observation of a spin-polarization instability in tilted magnetic fields”, *Physica B* **184**, 76 (1993). 36
- [49] J. C. Chokomakoua, N. Goel, S. J. Chung, M. B. Santos, J. L. Hicks, M. B. Johnson, and S. Q. Murphy, “Ising quantum Hall ferromagnetism in InSb-based two-dimensional electronic systems”, *Phys. Rev. B* **69**, 235 315 (2004). 36
- [50] G. M. Gusev, A. A. Quivy, T. E. Lamas, J. R. Leite, O. Estibals, and J. C. Portal, “Quantum Hall ferromagnet in a parabolic well”, *Phys. Rev. B* **67**, 155 313 (2003). 36

-
- [51] J. G. S. Lok, M. Lynass, W. Dietsche, K. von Klitzing, and M. Hauser, “Quantum Hall ferromagnetism of AlAs 2D electrons”, *Physica E* **22**, 94 (2004). 36
- [52] E. P. D. Poortere, E. Tutuc, and M. Shayegan, “Critical Resistance in the AlAs Quantum Hall Ferromagnet”, *Phys. Rev. Lett.* **91**, 216 802 (2003). 36
- [53] K. Vakili, Y. P. Shkolnikov, E. Tutuc, N. C. Bishop, E. P. D. Poortere, and M. Shayegan, “Spin-Dependent Resistivity at Transitions between Integer Quantum Hall state”, *Phys. Rev. Lett.* **94**, 176 402 (2005). 36
- [54] V. Piazza, V. Pellegrini, F. Beltram, W. Wegscheider, T. Jungwirth, and A. H. M. Donald, “First-order phase transitions in a quantum Hall ferromagnet”, *Nature* **402**, 638 (1999). 36, 75, 78
- [55] V. Piazza, V. Pellegrini, F. Beltram, and W. Wegscheider, “Metastable phase in the quantum Hall ferromagnet”, *Sol. State Comm.* **127**, 163 (2003). 36
- [56] K. Muraki, T. Saku, and Y. Hirayama, “Charge excitations in Easy-Axis and Easy-Plane Quantum Hall Ferromagnets”, *Phys. Rev. Lett.* **87**, 196 801 (2001). 36
- [57] T. Chakraborty and F. C. Zhang, “Role of reversed spins in the correlated ground state for the fractional quantum Hall effect”, *Phys. Rev. B* **29**, 7032 (1984). 36, 41
- [58] F. C. Zhang and T. Chakraborty, “Ground state of two-dimensional electrons and the reversed spins in the fractional quantum Hall effect”, *Phys. Rev. B* **30**, 7320 (1984). 36, 41
- [59] I. V. Kukushkin, K. von Klitzing, and K. Eberl, “Spin Polarization of Composite Fermions: Measurements of the Fermi Energy”, *Phys. Rev. Lett.* **82**, 3665 (1999). 36, 45, 46
- [60] T. Chakraborty, “Electron spin transitions in quantum Hall systems”, *Adv. Phys.* **49**, 959 (2000). 36
- [61] J. P. Eisenstein, R. Willett, H. L. Stormer, D. C. Tsui, A. C. Gossard, and J. H. English, “Collapse of the Even-Denominator Fractional Quantum Hall Effect in Tilted Fields”, *Phys. Rev. Lett.* **61**, 997 (1988). 37
- [62] R. G. Clark, S. R. Haynes, A. M. Suckling, J. R. Mallett, P. A. Wright, J. J. Harris, and C. T. Foxon, “Spin Configurations and Quasiparticle Fractional Charge of Fractional-Quantum-Hall-Effect Ground States in the N=0 Landau Level”, *Phys. Rev. Lett.* **62**, 1536 (1989). 37

- [63] J. P. Eisenstein, H. L. Stormer, L. Pfeiffer, and K. W. West, “Evidence for a Phase Transition in the Fractional Quantum Hall Effect”, *Phys. Rev. Lett.* **62**, 1540 (1989). 37
- [64] W. Kang, J. B. Young, S. T. Hannahs, E. Palm, K. Campman, and A. C. Gossard, “Evidence for a spin transition in the $\nu = \frac{2}{5}$ fractional quantum Hall effect”, *Phys. Rev. B* **56**, 12776(R) (1997). 37, 38
- [65] N. G. Morawicz, K. W. J. Barnham, C. Zammit, J. J. Harris, C. T. Foxon, and P. Kujawinski, “Observation of the fractional quantum Hall effect under hydrostatic pressure”, *Phys. Rev. B* **41**, 12687 (1990). 38
- [66] D. R. Leadley, R. J. Nicholas, D. K. Maude, A. N. Utjuzh, J. C. Portal, J. J. Harris, and C. T. Foxon, “Fractional Quantum Hall Effect Measurements at Zero g factor”, *Phys. Rev. Lett.* **79**, 4246 (1997). 38
- [67] H. Cho, J. B. Young, W. Wang, K. L. Campman, A. C. Gossard, M. Bichler, and W. Wegscheider, “Hysteresis and Spin Transitions in the Fractional Quantum Hall Effect”, *Phys. Rev. Lett.* **81**, 2522 (1998). 38, 39, 41
- [68] J. Eom, H. Cho, W. Kang, K. L. Campman, A. C. Gossard, M. Bichler, and W. Wegscheider, “Quantum Hall Ferromagnetism in a Two-Dimensional Electron System”, *Science* **289**, 2320 (2000). 38, 39, 81
- [69] D. C. Tsui and A. C. Gossard, “Resistance standard using quantization of the Hall resistance of GaAs-Al_xGa_{1-x}As heterostructures”, *Appl. Phys. Lett.* **38**, 550 (1981). 38
- [70] K. Park and J. Jain, “Phase Diagram of the Spin Polarization of Composite Fermions and a new Effective Mass”, *Phys. Rev. Lett.* **80**, 4237 (1998). 40
- [71] I. V. Kukushkin, J. H. Smet, K. von Klitzing, and W. Wegscheider, “Cyclotron resonance of composite fermions”, *Nature* **415**, 409 (2002). 40
- [72] R. Du, A. Yeh, H. Störmer, D. Tsui, L. N. Pfeiffer, and K. W. West, “Fractional Quantum Hall Effect around $\nu = \frac{3}{2}$: Composite Fermions with a Spin”, *Phys. Rev. Lett.* **75**, 3926 (1995). 40
- [73] S. Kraus, *Ph.D. thesis* (Max-Planck-Institut für Festkörperforschung, Stuttgart, Germany, 2003). 40, 78, 79
- [74] J. Lok, S. Kraus, O. Stern, W. Dietsche, K. von Klitzing, *et al.*, “Time and current dependencies of transport at the $\nu = \frac{2}{3}$ phase transition in narrow quantum wells”, *Physica E* **22**, 138 (2004). 40

-
- [75] K. Hashimoto, T. Saku, and Y. Hirayama, “Nuclear-spin-related resistance enhancements observed over a wide range of magnetic fields”, *Phys. Rev. B* **69**, 153 306 (2004). 40
- [76] R. G. Clark and P. Maksym, *Physics World* **2**, 39 (1989). 41
- [77] R. G. Clark, S. R. Haynes, J. V. Branch, A. M. Suckling, P. A. Wright, J. J. Harris, and C. T. Foxon, “Spin configurations and quasiparticle fractional charge of fractional QHE ground states in the $n=0$ Landau level”, *Surf. Sci.* **229**, 25 (1990). 41
- [78] J. P. Eisenstein, H. L. Stormer, L. N. Pfeiffer, and K. W. West, “Evidence for a spin transition in the $\nu = \frac{2}{3}$ fractional quantum Hall effect”, *Phys. Rev. Lett.* **41**, 7910 (1990). 41, 42
- [79] L. W. Engel, S. W. Hwang, T. Sajoto, D. C. Tsui, and M. Shayegan, “Fractional quantum Hall effect at $\nu = \frac{2}{3}$ and $\frac{3}{5}$ in tilted magnetic fields”, *Phys. Rev. B* **45**, 3418 (1992). 41, 42
- [80] S. Kronmüller, W. Dietsche, J. Weis, K. von Klitzing, W. Wegscheider, and M. Bichler, “New Resistance Maxima in the Fractional Quantum Hall Effect Regime”, *Phys. Rev. Lett.* **81**, 2526 (1998). 41, 43, 78, 79, 81
- [81] S. Kronmüller, W. Dietsche, K. von Klitzing, W. Wgscheider, and M. Bichler, “New resistance maxima of the 2DEG at fractional filling factors”, *Physica B* **256-258**, 82 (1998). 41
- [82] W. Dietsche and S. Kronmüller, “Anomalous interaction between electrons and nuclear spins at $\nu = \frac{2}{3}$ filling of the fractional quantum Hall effect”, *Physica E* **10**, 71 (2001). 42
- [83] S. Kronmüller, W. Dietsche, K. von Klitzing, G. Denniger, W. Wegscheider, and M. Bichler, “New Type of Nuclear-Spin Interaction from Resistively Detected NMR in the Fractional Quantum Hall Effect Regime”, *Phys. Rev. Lett.* **82**, 4070 (1999). 42, 43
- [84] O. I. Stern, *Ph.D. thesis* (Max-Planck-Institut für Festkörperforschung, Stuttgart, Germany, 2005). 43, 78, 79, 80
- [85] J. H. Smet, R. A. Deutschmann, W. Wegscheider, G. Abstreiter, and K. von Klitzing, “Ising Ferromagnetism and Domain Morphology in the Fractional Quantum Hall Regime”, *Phys. Rev. Lett.* **86**, 2412 (2001). 43
- [86] G. Bertotti, *Hysteresis in Magnetism* (Academic Press, San Diego, 1998). 43

- [87] S. Kraus, O. Stern, J. G. S. Lok, W. Dietsche, K. von Klitzing, *et al.*, “From Quantum Hall Ferromagnetism to Huge Longitudinal Resistance at the $2/3$ Fractional Quantum Hall State”, *Phys. Rev. Lett.* **89**, 266 801 (2002). 43, 44, 78
- [88] J. H. Smet, R. A. Deutschmann, F. Ertl, W. Wegscheider, G. Abstreiter, and K. von Klitzing, “Gate-voltage control of spin interactions between electrons and nuclei in a semiconductor”, *Nature* **415**, 281 (2002). 44, 80
- [89] K. Hashimoto, K. Muraki, T. Saku, and Y. Hirayama, “Electrically Controlled Nuclear Spin Polarization and Relaxation by Quantum-Hall States”, *Phys. Rev. Lett.* **88**, 176 601 (2002). 44, 80
- [90] G. Yusa, K. Hashimoto, K. Muraki, T. Saku, and Y. Hirayama, “Self-sustaining resistance oscillations: Electron-nuclear spin coupling in mesoscopic quantum Hall devices”, *Phys. Rev. B* **69**, 161 302 (2004). 44
- [91] G. Yusa, K. Muraki, K. Takashina, K. Hashimoto, and Y. Hirayama, “Controlled multiple quantum coherences of nuclear spins in a nanometre-scale device”, *Nature* **434**, 1001 (2005). 44
- [92] G. Yusa and N. Kumada and K. Muraki and Y. Hirayama, ”Individual Mechanism of Nuclear Spin Decoherence in a Nanoscale GaAs NMR Device”, *cond-mat/0510310*. 44
- [93] K. Hashimoto, K. Muraki, N. Kumanda, T. Saku, and Y. Hirayama, “Effects of Inversion Asymmetry on Electron-Nuclear Spin Coupling in Semiconductor Heterostructure: Possible Role of Spin-Orbit Interactions”, *Phys. Rev. Lett.* **94**, 146 601 (2005). 44
- [94] N. Freytag, Y. Tokunaga, M. Horvatič, C. Berthier, M. Shayegan, and L. P. Lévy, “New Phase Transition between Partially and Fully Polarized Quantum Hall States with Charge and Spin Gaps at $\nu = \frac{2}{3}$ ”, *Phys. Rev. Lett.* **87**, 136 801 (2001). 45, 46
- [95] O. Stern, N. Freytag, A. Fay, W. Dietsche, J. H. Smet, *et al.*, “NMR study of the electron spin polarization in the fractional Hall effect of a single quantum well: Spectroscopic evidence for domain formation”, *Phys. Rev. B* **70**, 075 318 (2004). 45, 47
- [96] S. Datta, *Surface Acoustic Wave Device* (Prentice-Hall, New Jersey, 1986). 49, 58
- [97] B. A. Auld, *Acoustic fields and waves in solid, Vol. I* (Wiley-Interscience, New York, 1973). 51

-
- [98] C. K. Campbell, *Surface Acoustic Wave Devices and Their Signal Processing Applications* (Academic Press, Boston, 1989). 51, 57, 60
- [99] A. R. Hutson and D. L. White, “Elastic Wave Propagation in Piezoelectric Semiconductors”, *J. Appl. Phys.* **33**, 40 (1969). 51
- [100] K. A. Ingebrigsten, “Linear and Nonlinear Attenuation of Acoustic Surface Waves in a Piezoelectric Coated with a Semiconducting Film”, *J. Appl. Phys.* **41**, 454 (1972). 51
- [101] B. K. Adler, *IEEE Trans. Sonics Ultrason* **SU-18**, 115 (1971). 52
- [102] A. Knäbchen, Y. B. Levinson, and O. Entin-Wohlmann, “Surface acoustic-wave attenuation by a two-dimensional electron gas in a strong magnetic field”, *Phys. Rev. B* **54**, 10 696 (1996). 53
- [103] S. H. Simon, “Coupling of surface acoustic waves to a two-dimensional electron gas”, *Phys. Rev. B* **54**, 13 878 (1996). 53
- [104] J. P. Robinson, M. P. Kennett, N. R. Cooper, and V. I. Fal’ko, “Surface Acoustic-Wave-Induced Magnetoresistance Oscillations in a Two-Dimensional Electron Gas”, *Phys. Rev. Lett.* **93**, 036 804 (2004). 53
- [105] M. P. Kennett, J. P. Robinson, N. R. Cooper, and V. I. Fal’ko, “Quantum and classical surface-acoustic-wave-induced magnetoresistance oscillations in a two-dimensional electron gas”, *Phys. Rev. B* **71**, 195 420 (2005). 53
- [106] A. Wixforth, J. P. Kotthaus, and G. Weinmann, “Quantum Oscillations in the Surface-Acoustic-Wave Attenuation Caused by a Two-Dimensional Electron System”, *Phys. Rev. Lett.* **56**, 2104 (1986). 53, 54
- [107] A. Schenstrom, Y. J. Qian, M.-F. Xu, H.-P. Baum, M. Levy, and B. K. Sarma, “Frequency dependent breakdown of the dissipationless state in the quantum Hall effect”, *Sol. State Comm.* **68**, 357 (1988). 53
- [108] A. Wixforth, J. Scriba, M. Wassermeier, J. P. Kotthaus, G. Weimann, and W. Schlapp, “Surface acoustic waves on GaAs/Al_xGa_{1-x}As heterostructures”, *Phys. Rev. B* **40**, 7874 (1989). 53, 67, 99
- [109] I. L. Drichko, A. M. Diakonov, I. Y. Smirnov, Y. M. Galperin, and A. I. Toropov, “High-frequency hopping conductivity in the quantum Hall regime: Acoustical studies”, *Phys. Rev. B* **62**, 7470 (2000). 53
- [110] Y. Takagaki, E. Wienicke, K.-J. Friedland, and K. H. Ploog, “Giant Surface Acoustic Wave Attenuation in the Quantum Hall Regime Induced by a DC Current”, *Jpn. J. Appl. Phys.* **41**, 2583 (2002). 53

- [111] R. B. Dunford, M. R. Gates, C. J. Mellor, V. W. Rampton, J. S. Chauhan, J. R. Middleton, and M. Henini, “Surface acoustic wave comparison of single and double layer AlGaAs/GaAs 2D hole systems”, *Physica B* **316-317**, 219 (2002). 53
- [112] I. L. Drichko, A. M. Diakonov, I. Y. Smirnov, G. O. Andrianov, O. A. Mironov, *et al.*, “High-frequency transport in *p*-type Si/Si_{0.87}Ge_{0.13} heterostructures studied with surface acoustic wave in the quantum Hall regime”, *Phys. Rev. B* **71**, 045 333 (2005). 53
- [113] R. L. Willett, M. A. Paalanen, R. R. Ruel, K. W. West, L. N. Pfeiffer, and D. J. Bishop, “Anomalous Sound Propagation at $\nu = \frac{1}{2}$ in a 2D Electron Gas: Observation of a Spontaneously Broken Translational Symmetry?”, *Phys. Rev. Lett.* **65**, 112 (1990). 53, 55
- [114] M. A. Paalanen, R. L. Willett, P. B. Littlewood, R. R. Ruel, K. W. West, L. N. Pfeiffer, and D. J. Bishop, “rf conductivity of a two-dimensional electron system at small Landau-level filling factors”, *Phys. Rev. B* **45**, 11 342 (1992). 53
- [115] R. L. Willett, “Surface acoustic wave studies of electron correlations in the 2DES”, *Surface Science* **305**, 76 (1994). 53
- [116] R. L. Willett, K. W. West, and L. N. Pfeiffer, “Transition in the Correlated 2D Electron System Induced by a Periodic Density Modulation”, *Phys. Rev. Lett.* **78**, 4478 (1997). 53
- [117] R. L. Willett, K. W. West, and L. N. Pfeiffer, “Experimental Demonstration of Fermi Surface Effects at Filling Factor 5/2”, *Phys. Rev. Lett.* **88**, 066 801 (2002). 53
- [118] R. H. Parmenter, “The acoustoelectric effect”, *Phys. Rev.* **89**, 990 (1953). 55
- [119] V. I. Fal’ko and S. V. Iordanskii, “Electron-phonon drag effect at 2D Landau levels”, *J. Phys: Condensed Matter* **4**, 9201 (1992). 55
- [120] J. P. Wolfe, *Imaging Phonons: Acoustic Wave Propagation in Solids* (Cambridge University Press, Cambridge, 1998). 58
- [121] C. K. Campbell, *Surface Acoustic Wave Devices for Mobile and Wireless Communications* (Academic Press, San Diego, 1998). 58, 59
- [122] J. M. Deacon and Highway, “Acoustic surface propagation on gaas”, *Electronics Letters* **8**, 6 (1972). 59

-
- [123] T. W. Grudkowski and M. Gilden, “Realization of temperature-compensated GaAs surface acoustic wave delay lines”, *Appl. Phys. Lett.* **38**, 412 (1980). 59
- [124] J. G. S. Lok, S. Kraus, M. Pohlt, W. Dietsche, K. von Klitzing, W. Wegscheider, and M. Bichler, “Spin effects in the magnetodrag between double quantum wells”, *Phys. Rev. B* **63**, 041 305 (2001). 61
- [125] K. Muraki, J. G. S. Lok, S. Kraus, W. Dietsche, K. von Klitzing, *et al.*, “Coulomb Drag as a Probe of the Nature of Compressible States in a Magnetic Field”, *Phys. Rev. Lett* **92**, 246 801 (2004). 61
- [126] R. D. Wiersma, J. G. S. Lok, S. Kraus, W. Dietsche, K. von Klitzing, *et al.*, “Activated Transport in the Separate Layers that Form the $\nu_t = 1$ Exciton Condensate”, *Phys. Rev. Lett* **93**, 266 805 (2004). 61
- [127] R. M. Arzt, E. Salzmann, and K. Dransfeld, “Elastic Surface Waves in Quartz at 360 MHz”, *Appl. Phys. Lett.* **10**, 165 (1967). 64
- [128] A. Esslinger, A. Wixforth, R. W. Winkler, J. P. Kotthaus, H. Nickel, W. Schlapp, and R. Lösch, “Acoustoelectric study of localized states in the quantized Hall effect”, *Sol. State Comm.* **84**, 939 (1992). 68
- [129] U. R. G. Lommer and F. Malcher, “Reduced g factor of subband Landau levels in AlGaAs/GaAs heterostructures”, *Phys. Rev. B* **32**, 6965 (1985). 78
- [130] E. L. Ivchenko and A. A. Kiselev, “Electron g factor of quantum wells and superlattices”, *Sov. Phys. Semicond.* **26**, 827 (1992). 78
- [131] F. Zhang and S. dar Sarma, “Excitation gap in the fractional quantum Hall effect: Finite layer thickness corrections”, *Phys. Rev. B* **33**, 2903 (1986). 79
- [132] L. Höppel, *Ph.D. thesis* (Max-Planck-Institut für Festkörperforschung, Stuttgart, Germany, 2004). 79, 80
- [133] A. W. Overhauser, “Polarization of Nuclei in Metals”, *Phys. Rev.* **92**, 411 (1953). 79
- [134] G. Tatara and H. Kohno, “Theory of Current-Driven Domain Wall Motion: Spin Transfer versus Momentum Transfer”, *Phys. Rev. Lett.* **92**, 086 601 (2004). 79
- [135] J. Shibata, G. Tatara, and H. Kohno, “Effect of Spin Current on Uniform Ferromagnetism: Domain Nucleation”, *Phys. Rev. Lett.* **94**, 076 601 (2005). 79
- [136] O. Stern, private communication. 81, 83

- [137] F. Alberici-Kious, J. P. Bouchaud, L. F. Cugliandolo, and P. Doussineau, “Aging in $K_{1-x}Li_xTaO_3$: A Domain Growth Interpretation”, *Phys. Rev. Lett.* **81**, 4987 (1998). 82
- [138] I. L. Drichko, A. M. Diakonov, A. M. Kreshchuk, T. A. Polyanskaya, I. G. Savel’ev, I. Y. Smirnov, and A. V. Suslov, “Electron localization in sound absorption oscillations in the quantum Hall effect regime”, *Semiconductors* **31**, 384 (1997). 99
- [139] L. A. Tracy, J. P. Eisenstein, M. P. Lilly, L. N. Pfeiffer, and K. W. West, “Surface acoustic wave propagation and inhomogeneities in low-density two-dimensional electron systems near the metal-insulator transition”, *Solid State Communications* **137**, 150 (2006). 99
- [140] J. M. Shilton, V. I. Talyanskii, M. Pepper, D. A. Ritchie, J. E. F. Frost, *et al.*, “High-frequency single-electron transport in a quasi-one-dimensional gaas channel induced by surface acoustic waves”, *J. Phys.: Condens. Matter* **8**, L531 (1996). 102
- [141] C. Rocke, S. Zimmermann, A. Wixforth, J. P. Kotthaus, G. Böhm, and G. Weimann, “Acoustically Driven Storage of Light in a Quantum Well”, *Phys. Rev. Lett.* **78**, 4099 (1997). 102
- [142] M. Rotter, A. V. Kalameitsev, A. O. Govorov, W. Ruile, and A. Wixforth, “Charge Conveyance and Nonlinear Acoustoelectric Phenomena for Intense Surface Acoustic Waves on a Semiconductor Quantum Well”, *Phys. Rev. Lett.* **82**, 2171 (1999). 102
- [143] F. Alsina, J. A. H. Stotz, R. Hey, and P. V. Santos, “Acoustically induced potential dots in gaas quantum wells”, *Sol. State Comm.* **129**, 453 (2003). 102
- [144] M. M. de Lima, J. R. Hey, J. A. H. Stotz, and P. V. Santos, “Acoustic manipulation of electron-hole pairs in gaas at room temperature”, *App. Phys. Lett.* **84**, 2569 (2004). 102
- [145] J. A. H. Stotz, F. Alsina, R. Hey, and P. V. Santos, “Acoustically induced dynamic potential dots”, *Physica E* **26**, 67 (2005). 102
- [146] V. I. Talyanskii, M. R. Graham, and H. E. Beere, “Acoustoelectric Y-branch switch”, *App. Phys. Lett.* **88**, 083501 (2006). 102
- [147] M. Yamanouchi, D. Chiba, F. Matsukura, and H. Ohno, “Current-induced domain-wall switching in a ferromagnetic semiconductor structure”, *Nature* **428**, 539 (2004). 103

- [148] M. Yamanouchi, D. Chiba, F. Matsukura, T. Dietl, and H. Ohno, “Velocity of Domain-Wall Motion Induced by Electrical Current in the Ferromagnetic Semiconductor (Ga,Mn)As”, *Phys. Rev. Lett.* **98**, 096 601 (2006). 103
- [149] E. Saitoh, H. Miyajima, T. Yamaoka, and G. Tatara, “Current-induced resonance and mass determination of a single magnetic domain wall”, *Nature* **432**, 203 (2004). 103

Deutsche Zusammenfassung

Ziel dieser Arbeit ist die Untersuchung eines speziellen Spin-Phänomens in zweidimensionalen Elektronensystemen (2DES) bei hohen Magnetfeldern und tiefen Temperaturen.

Beim ganzzahligen Quanten-Hall-Effekt besetzen die Elektronen eine ganzzahlige Anzahl von Energie-Niveaus, welche als Landau-Niveaus bezeichnet werden (Kapitel 2.3.1). Der energetische Abstand dieser Landau-Niveaus entspricht der Zyklotronenergie der Elektronen. Infolge des Elektronenspins kommt bei höheren Magnetfeldern eine Zeeman-Aufspaltung der Landau-Niveaus hinzu. Ist die Zahl der Elektronen nicht ausreichend, um ein Landau-Niveau vollständig zu füllen, so können Grundzustände mit verschiedenen Elektron-Polarisationen koexistieren. Solche Systeme sind charakterisiert durch eine ferromagnetische Ordnung und werden daher als Quanten-Hall-Ferromagnete (QHF) bezeichnet. Quanten-Hall-Ferromagnetismus kann durch eine Zunahme der Austauschenergie im ferromagnetischen Zustand erklärt werden. Annahmen des Hartree-Fock-Modells sind in der Lage, die physikalischen Vorgänge zu beschreiben. Die Untersuchung des quasi-2DES, welches sich am Übergang der Halbleiter-Heterostruktur ausbildet, führt zu Effekten, die nicht in das oben beschriebene Bild des Freien-Partikel-Modells passen. Berücksichtigt man zusätzlich die Wechselwirkung der Elektronen untereinander, dann kommt es zur Bildung von neuen Grundzuständen, wobei die Elektronen von den vorhandenen freien Zuständen nur ganz bestimmte besetzen. Dieses Phänomen ist unter den Namen gebrochenzahliger Quanten-Hall-Effekt bekannt (Kapitel 2.4). Gegen Ende des letzten Jahrhunderts lieferten Experimente Hinweise auf ferromagnetische Zustände auch im Bereich des gebrochenzahligen Quanten-Hall Effekts bei den Füllfaktoren $\nu = \frac{2}{3}$ und $\nu = \frac{2}{5}$. Bei diesen Füllfaktoren sind die Spin-Zustände hochgradig korreliert, und Übergänge zwischen Grundzuständen mit unterschiedlichen Spin-Polarisationen werden möglich. In dieser Situation ist die Hartree-Fock Näherung allerdings nicht mehr gültig. Experimente lieferten Hinweise darauf, dass diese Phänomene in direkter Verbindung zum Ising-Ferromagnetismus stehen. Obwohl es auch einige Beobachtungen gibt, die keine Analogie zu gewöhnlichen Ising-Systemen herstellen, könnte die Möglichkeit von Domänenbildung bestehen, wobei die Grundzustände durch unterschiedliche Spin-Polarisationen gegeben sind. Das Modell wird komplizierter, wenn man den Einfluss der Atomkerne berücksichtigt. Verschiedene Experimente konnten tatsächlich zeigen, dass bei Füllfaktor $\nu = \frac{2}{3}$ die Elektronendynamik stark an den Kern gekoppelt ist.

In dieser Arbeit sollen nun der Grundzustand und die untersten angeregten Zustände bei Füllfaktor $\nu = \frac{2}{3}$ untersucht werden. Dazu werden die Transporteigenschaften

eines 2-dimensionalen Elektronengases mittels akustischer Oberflächenwellen (Surface Acoustic Waves, SAW) gemessen und mit Daten verglichen, die mit Lock-In Technik ermittelt wurden.

Akustische Oberflächenwellen sind elastische Moden, die sich entlang der Oberfläche eines Kristalls ausbreiten können. In GaAs verursachen diese Wellen eine Deformation des Kristallgitters und ein oszillierendes elektrisches Feld. Letzteres kann mit den freien Ladungsträgern eines 2DES wechselwirken und zu einer Dämpfung und einer modifizierten Ausbreitungsgeschwindigkeit der akustischen Oberflächenwelle führen. Die Messung dieser Effekte liefert eine elektrische Leitfähigkeit bei der speziellen Frequenz bzw. Wellenlänge einer akustischen Mode. Dieser Parameter kann bis in den GHz Bereich ausgeweitet werden und wird beim Design der Probe festgelegt.

Der erste Teil meiner Arbeit befasst sich daher mit dem Design und dem Aufbau eines Messsystems, mit der die Messung von tiefen und hohen Frequenzen bei Temperaturen von unter 400 mK möglich ist. Dieses Messsystem beinhaltet u.a. die Wahl eines verlustarmen Koaxialkabels für das HF-Signal, sowie eine gute thermische Ankopplung für eine effiziente Wärmeabfuhr. Um ein Übersprechen zwischen den Überträgern zu minimieren, wurden ein spezieller Probenhalter mit SMP-Anschlussstechnik und ein planparalleler Wellenleiter konzipiert. Große Sorgfalt wurde beim Design der Überträger zur Erzeugung und zur Detektion der akustischen Oberflächenwellen walten gelassen. Für die eigentliche Messung verwendeten wir Hall-Proben mit Überträgern an den entgegengesetzten Enden der Probe. Eine quasi-DC Leitfähigkeit σ_{xx} konnte dann aus den spezifischen Widerständen bei Anregungsströmen von einigen Hz errechnet werden. Gleichzeitig konnte ein wellenspezifisches σ_{xx} bestimmt werden, indem die Absorption und Dispersion der akustischen Oberflächenwelle gemessen wurde.

In der quasi-DC Messung fand sich ein Maximum in der Leitfähigkeit, welches auf einen Phasenübergang zwischen unterschiedlich polarisierten Grundzuständen hindeutet. Alle normalen Magnetotransport-Oszillationen konnten in der quasi-DC Messmethode mit der akustischen Oberflächenwellenmessung reproduziert werden. Sogar die kleinen SdH-Oszillationen konnten in den transmittierten SAWs aufgelöst werden, was die hohe Auflösung unserer Anordnung bestätigt. Allerdings konnte das Maximum in der quasi-DC Leitfähigkeit beim Spin-Phasen-Übergang nicht beobachtet werden. Dieses unerwartete Ergebnis wurde mit Hilfe der SAWs mit Frequenzen zwischen 100 MHz und mehr als 1 GHz, was Wellenlängen zwischen 25 μm und 2 μm entspricht, bestätigt.

Wir überprüften mit Hilfe von Akusto-Drift-Messungen, dass die SAWs effektiv mit den Anregungen interagieren, die verantwortlich für die QHF sind.

Ein Maximum in der Leitfähigkeit der akustischen Oberflächenwelle war ebenfalls nicht zu beobachten, wenn der quasi-DC Strom erhöht wurde, was zu einer dramatischen Zunahme der quasi-DC Leitfähigkeit führte (huge longitudinal resistance effect, HLR). Dieser Effekt basiert auf dem Einfluss der Kernspins, welche infolge der

Hyperfein-Wechselwirkung mit den Elektronenspins polarisiert werden (Dynamische Kernpolarisierung).

Wir haben ein Model entwickelt um die Fortpflanzung von SAW in einem inhomogenen 2DES zu simulieren. Im Rahmen unserer Messgenauigkeit können wir sagen, dass die, von den Domänengrenzen eingenommen Fläche, weniger als 1% des Probenkörpes einnimmt. Unter Verwendung einer Hartree-Fock Abschätzung für die Dicke einer einzelnen Domänengrenze kommt man durch eine einfache Rechnung zu dem Ergebnis, dass die Domänengröße $3.3 \mu\text{m}$ nicht unterschreiten sollte.

Im Bereich des Quanten-Hall-Ferromagnetismus werden viele experimentelle Untersuchungen vorgenommen, die sich jedoch hauptsächlich auf die quasi-DC Transporteigenschaften der Elektronensysteme beschränken. In dieser Doktorarbeit haben wir diese Untersuchungen des Phasenüberganges bei Füllfaktor $\nu = \frac{2}{3}$ auf den Hochfrequenzbereich ausgeweitet. Der nächste Schritt wäre die Ausweitung unserer HF-Technik auf verschiedene Arten der ferromagnetischen Ordnung, wie z.B. Quanten-Hall-Ferromagnetismus, der in elektronischen Doppellagensystemen auftritt. In diesen Doppellagensystemen ist es möglich, die ferromagnetische Ordnung sowohl entlang der Anisotropieachse als auch in der Anisotropieebene zu erzeugen.

Der Aufbau diese Doktorarbeit ist wie folgt:

- Kapitel 2 liefert eine Beschreibung der fundamentalen Eigenschaften von 2DES unter dem Einfluss von senkrechten Magnetfeldern. Das Konzept der Landau-Niveaus wird erläutert, ebenso wie die Modelle zur Beschreibung des ganzzahligen und gebrochenzahligen Quanten-Hall Effekts.
- In Kapitel 3 folgt eine Einführung in die Prinzipien des QHF. Dabei wird sowohl auf das theoretische Bild als auch auf experimentelle Beweise des Spin-Phasenüberganges bei gebrochenzahligen Füllfaktoren eingegangen. Im letzten Teil dieses Kapitels werden wir uns auf den Spin-Phasenübergang bei Füllfaktor $\frac{2}{3}$ konzentrieren.
- Kapitel 4 beschreibt die verwendeten Messtechniken und die Wechselwirkungsmechanismen zwischen akustischen Oberflächenwellen und einem 2DES. Da ein Grossteil meines Projektes aus dem Design und Aufbau der benötigten Messvorrichtung bestand, werden ebenfalls die Probleme, die während meiner Arbeit aufgetaucht sind, und deren Lösung behandelt.
- Kapitel 5 umfasst alle gesammelten Ergebnisse meiner Messungen zum Spin-Phasenübergang bei Füllfaktor $\frac{2}{3}$. Dabei werden die Daten der quasi-DC Messungen (3.4 Hz), sowie der HF-Messungen (MHz bis GHz Bereich) präsentiert. Die experimentelle Befunde werden kommentiert, und es werden Modelle zur Erklärung vorgeschlagen.
- Abschließend werden alle Ergebnisse in der Zusammenfassung kurz umrissen.

Acknowledgments

First of all I'd want to thank all the people that helped me during my staying in Stuttgart. They are too many to be mentioned.

I'd like to thank in particular some of them:

- Prof. Klaus von Klitzing for allowing me to do my PhD in his department.
- Prof. Werner Dietsche for the support during my PhD, the relaxed atmosphere in his group and the Brezeln on Fridays. A special thank for reading the manuscript during the early stage of preparation.
- Prof. Gert Denninger for accepting to be my Mitberichter.
- Dr. Sjoerd Lok, my officemate for almost three years, for the discussions about physics and life.
- Alexander Hubel, Mark Lynass and Frank Ospald for reading the manuscript.
- All the members of the Dietsche's group that I met during these years (Stefan Kraus, Omar Stern, Mark Lynass, Rodney Wiersma, Lars Tiemann) for the nice atmosphere inside and outside the institute and for the many discussions about physics.
- Maik Hauser for the realization of good wafers.
- Monika Riek for help in the process of the transducers. All the people of the clean room: Ulrike Waizmann, Thomas Reindl and Achim Guth.
- Werner Rauscher, Manfred Schmid and all the technicians of the Werkstatt for technical support.
- All the members of the department vK for the friendly atmosphere with a special thank to Eleonora Storace.

Curriculum Vitae

Name	Dimitri Dini
Nationality	Italian
Date of birth	8 September 1978
Place of birth	Pescia, Italy
Marital status	Single

Studies

02/2003–Present	PhD student Max-Planck-Institut für Festkörperforschung (Stuttgart) in the group of Prof. Dr. Klaus von Klitzing
09/2002	Laurea Università degli Studi di Pisa, Pisa (Italy) <i>Intersubband electrodynamics in microcavity</i> , with Prof. Fabio Beltram
10/1996 – 10/2001	Studies of physics, Università degli Studi di Pisa, Pisa (Italy)
06/1996	High School leaving exam, Liceo Scientifico Statale, Montecatini Terme (Italy)

...though this knave came something saucily into the world...
...there was good sport at his making.

William Shakespeare

from *King Lear, Act I, scene I*